MASTER THESIS

Modeling the Response to Terrestrial Gamma-Ray Flashes at the Zugspitze Research Station

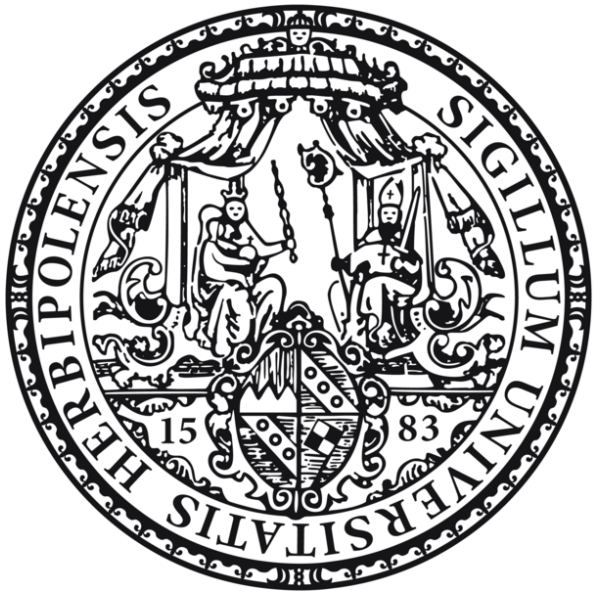

JULIUS-MAXIMILIANS-UNIVERSITY WÜRZBURG

Institute for Theoretical Physics and Astrophysics

Chair for Astronomy

submitted by

Patrik Ehrmann

from Ingelfingen

February 2026

Die vorliegende Arbeit wurde im Zeitraum vom 1/9/2025 bis zum 2/3/2026 am Lehrstuhl für Astronomie der Julius-Maximilians-Universität Würzburg unter der Betreuung von Dr. Thomas Siegert angefertigt. Die Zweitbetreuung erfolgte durch Prof. Dr. Raimund Ströhmer.

Abstract

This thesis investigates the potential detection and physical characteristics of Terrestrial Gamma-ray Flashes (TGFs) from a ground-based perspective, especially focusing on the Umweltforschungsstation Schneefernerhaus (UFS) in the German alps at 2650 m altitude above sea level. While TGFs are primarily observed by satellites, this work analyses how high-altitude stations can mitigate atmospheric attenuation to study these millisecond high-energy bursts. Utilizing the MEGAlib framework and GEANT4, a comprehensive simulation environment was developed that incorporates the complex topography of the Zugspitze and its Schneeferner glacier as well as the strcutural environment of the detector housing at the UFS, called Kugelalm. The theoretical framework for γ-rays from lightning discharges is grounded in the Relativistic Runaway Electron Avalanche (RREA) model and the Relativistic Feedback Mechanism (RFM). Using satellite data from the Gamma-ray Burst Monitor (GBM) onboard the Fermi satellite, typical spectral and temporal parameters of TGFs have been extracted to estimate the integrated flux of the TGFs and the hardness ratio. The hardness ratio describes the hardness of a spectrum, it compares the amount of photons in a hard energy band with the amount a defined soft energy band where both bands are defined. The result reveals a strong energy-dependency regarding TGF detectability. For lower input energies of E_{in} $\leq$1 MeV, detection is statistically improbable due to a photon survival probability of 10^{-12} form a 10 km altitude while the detector is located at an altitude of 2657 m. At E_{in}=10 MeV, the survival probability increases to 10^{-4} indicating the trend towards detectability of high-energy photons. The input energy also limits the maximum distance from which a TGF can be observed. The maximum distance for a luminosity of 10^{19} ph s^{-1} was determined to 5,34 km. Given this maximum distance, resulting observation window amounts to 63 monthly thunderstorm hours, totaling in 756 thunderstorm hours per year. With a TGF-to-flash of $10^{-3} - 10^{-2}$ this would result in up to 7 observable TGFs per year at the UFS. For a distance of 500 m between detector and TGF source the number of detectable photons including atmospheric attenuation is in the order of magnitude 10^{7} while for a distance of 5 km it decreases to

174. It was also shown that for higher energies it is more favorable placing the detector in the Kugelalm with the ratio of counts with house vs counts without house being approximately 1.5 for E_{in}=10 MeV. For high-energy photons the house acts as a scatterer which creates a lot of secondary particles. These secondary particles are then detected more frequently and increase the number of detected events. These findings establish a quantitative baseline for the energy response of scintillators in high-mountain environments and confirm that the UFS is a suitable location for monitoring high-energy atmospheric phenomena, particularly in the range around and above 10 MeV.

Abstract - German

Diese Arbeit untersucht die mögliche Detektierbarkeit und die physikalischen Eigenschaften von Terrestrial Gamma-ray Flashes (TGFs) von einer bodengestützten Perspektive aus gesehen. Dabei wird besonderer Fokus auf die Umweltforschungsstation Schneefernerhaus (UFS) gelegt, welche sich in den deutschen Alpen auf 2650 m Höhe über dem Meeresspiegel befindet. Während TGFs primär mit Satelliten beobachtet werden, soll diese Arbeit analysiere wie hochgelegene Messstationen atmosphärische Dämpfung minimieren können, um diese im Millisekundenbereich auftretenden hochenergetischen Strahlungsausbrüche zu erforschen. Indem das MEGAlib framework und GEANT4 genutzt werden, wurde eine umfassende Simulationsumgebung erstellt, welche die komplexe Topographie der Zugspitze mit deren Schneefernergletscher sowie die strukturelle Umgebung der UFS, die Kugelalm, miteinbezogen. Das theoretische Framework für γ-Strahlung von Blitzentladungen ist auf dem Relativistic Runaway Electron Avalanche (RREA) Modell und dem Relativistic Feedback Mechanism (RFM) begründet. Mithilfe von Satellitendaten des Gamma-ray Burst Monitor (GBM), welcher auf dem Fermi-Satelliten monitiert ist, werden typische spektrale und zeitliche Parameter von TGFs extrahiert, um den aufintergrierten Flux von TGFs, sowie den hardness ratio abschätzen zu können. Der hardness ratio beschreibt die Härte eines Spektrum, die Anzahl an Photonen in einem 'harten' Energiebereich wird mit der Anzahl an Photonen in einem 'weichen' Energiebereich verglichen wobei beide Energiebereich definiert sind. Dieses Ergebnis offenbart eine starke Energieabhängigkeit bezüglich der TGF-Detektierbarkeit. Für kleinere Einfallsenergien von $E_{\text{in}} \leq 1\,\text{MeV}$ ist die Detektion statistische gesehen unwahrscheinlich, da die Photonen mit einer Wahrscheinlichkeit von 10^{-12} den Detektor erreichen wenn dieser auf einer Höhe von 2657 m platziert ist und die Photonenquelle sich auf 10 km höhe befindet. Für höhere Energien von E_{in}=10 MeV hingegen erhöht sich die Wahrscheinlichkeit der Detektierbarkeit auf 10^{-4}. Die Einfallsenergie limitiert auch die maximale Distanz, in der ein TGF gemessen werden kann. Ausgehend von einer Luminosität von $10^{19}\,\text{ph}\,\text{s}^{-1}$ beträgt die maximal messabre Distanz 5.34 km. Mit dieser Distanz ergibt sich ein effektives Beobachtungsfenster von 63 monatlichen Blitzstunden,

das sich auf 756 jähliche Blitzstunden aufsummiert. Mit einem TG-to-flash Verhältnis von $10^{-3} - 10^{-2}$ ergeben sich damit jährlich 7 beobachtbare TGFs an der UFS. Für eine Distanz von 500 m zwischen Detektor und TGF Quelle bewegt sich die Anzahl der dtektierbaren Photonen unter Beeinflussung atmosphärischer Dämpfung in der Größenordnung 10^7, während für eine Distanz von 5 km 174 Photonen detektierbar sind. Es wurde ebenfalls gezeigt, dass es für höhere Energien vorteilhafter ist, den Detektor innerhalb der Kugelalm zu platzieren, da das Verhältnis von Detektorevents mit Haus vs Detektorevents ohne Haus für E_{in}=10 MeV im Bereich von 1.5 liegt. Für hochenergetische Photonen fungiert das Haus als Streukörper, wodurch viele Sekundärteilchen erzeugt werden. Diese Sekundärteilchen können dementsprechend öfter detektiert werden und erhöhen damit die Anzahl an detektierten Events. Diese Ergebnisse bilden eine quantitative Grundlage für die spektrale Antwort von Szintillatoren in hochgelegenen Umgebungen und bestätigen, dass die UFS ein passender Standort für die Beobachtung von hochenergetischen atmosphärischen Phänomenen ist, vor allem für Energien im Bereich und oberhalb von 10 MeV.

Contents

1 List of Abbreviations

TGF	Terrestrial Gamma-ray Flash
UFS	Umweltforschungsstation Schneefernerhaus
STP	Standard Temperature and Pressure
CG	Cloud-to-Ground
TLE	Transient Luminous Events
GEANT	Geometry And Tracking
BATSE	Burst And Transient Source Experiment
CGRO	Compton Gamma Ray Observatory
RHESSI	Reuven Ramaty High Energy Solar Spectroscopic Imager
GBM	Gamma-ray Burst Monitor
AGILE	Astro-rivelatore Gamma a Immagini Leggero
ASIM	Atmosphere-Space Interactions Monitor
RREA	Relativistic Runaway Electron Avalanche
GRB	Gamma Ray Burst

EIP Electric In-cloud Pulse

VLF Very Low Frequency

SPE Solar Particle Event

RFM Relativistic Feedback Mechanism

WWLLN World-Wide Lightning Location Network

IC Intracloud

NORM Naturally Occuring Radioactive Material

GCR Galactic Cosmic Rays

SCR Solar Cosmic Rays

CME Coronal Mass Ejection

DLR Deutsches Zentrum für Luft- und Raumfahrt

TUM Technische Universität München

JMU Julius-Maximilians-Universität Würzburg

PMT Photo-Multiplier Tube

FWHM Full Width at Half Maximum

MEGAlib Medium-Energy Gamma-ray Astronomy library

Geomega Geometry for MEGAlib

Cosima Cosmic Simulation for MEGAlib

HEP High-Energy Physics

MCS Monte Carlo Simulation

PDF Probability Density Function

NASA National Aeronautics and Space Administration

MPE Max-Planck Institute for Extraterrestrial Phyiscs

TTE Time-Tagged Event

DRM Detector Response Matrix

MCMC Markov Chain Monte Carlo

List of Figures

List of Tables

2 Introduction

Thunderstorms are some of the most impressive but least understood meteorological phenomena seen on Earth. The mechanical and thermodynamical processes of building a thundercloud structure and lightning processes in general have been intensively studied over three decades [Mazur, 2016] in which it has been shown that thunderclouds also work as natural particle accelerators [Paras and Pooja, 2021]. The discovery of highly energtic radiation bursts originating from Earths atmosphere was the start of a new research chapter regarding atmospheric physics. These so-called Terrestrial Gamma-ray Flashes (TGFs) have been a topic of interest for researchers since then [Dwyer and Uman, 2014]. They consist of pulses of ultrashort gamma rays with energies of up to tens of mega eletron volt – an energy range which is ususally expected for astronomical objects.

The research on TGFs ranges over multiple scientific areas. There are open fundamental electrodynamical questions on how the particles can be accelerated to sufficient velocities before being slowed down by scattering at air molecules [Dwyer and Uman, 2014, Köhn et al., 2020]. Researching TGFs is not just about scientific understanding, it is also of practical importance since air radiation has effects on radiation exposure for high-altitude flights [Dwyer et al., 2012]. Even though there are satellite-based measurements, the microphysics and the connection between lightning dynamics and TGF creation and acceleration is still not fully understood [Marisaldi et al., 2013, Wada et al., 2025].

A big challenge for TGF research is the atmosphere and its associated absorption of high-energy photons when the goal is to perform ground-based measurements. Since satellite detectors measure at high altitudes of around 560 km, this absorption effect appears predominantely for ground-based stations [Hongbo et al., 2019a]. The research station Umweltforschungsstation Schneefernerhaus (UFS) which is located at the Zugspitze mountain, the highest mountain in the German alps, takes a key role. Since it is located at an altitude of 2650 m it is closer to possible TGF source regions originating from thunderclouds. The high altitude makes absorption less relevant and

therefore the detectability is increased. For measuring and interpreting TGF data at the UFS, a lot of different factors come into play which are evaluated in the following thesis. The detection of photons is not just dependent on the source strength but also on atmsopheric scattering, the local topography and shielding by different structures. Therefore, detailed modeling is necessary. The goal of this study is to evaluate the origin and propagation of TGFs and the associated measurement of these through three-dimensional Monte Carlo simulations. By systematically varying parameters it is shown how different effects and material structures contribute to the resulting spectrum. The final goal of this thesis is to estimate the detection frequency of TGFs with a dedicated gamma-ray detector inside the Kugelalm. This thesis is structured as follows: Section 3.1 is introducing the theoretical knowledge about thunderstorms in general. Thunderstorms build the basis of the phenomena which we simulate in this thesis and are an essential part of the physics we are interested in. Section 3.2 then describes particle interactions between photon and matter. These interaction not just appear in the thundercloud, they also describe the interaction mechanisms happening in the detector. It is necessary to know about the possible interaction to be able to analyse the resulting spectra of the simulations. Section 3.3 describes the main phenomenon which should be simulated and researched: TGFs. Main properties like energy range or duration of TGFs are mentioned as well as the most common models which describe TGFs are explained. This section closes with previously performed TGF measurements to which the simulation results can be compared with. Section 3.4 shows the basics of natural radioactivity and other underlying background radiation like Solar particle Events (SPEs). Since this background radiation is constantly there it is of importance to evaluate the measured background to see if the TGF signals are influenced by this. Section 4.1 starts with introducing the measurement site with its surrounding environment, the UFS and the Kugelalm where the detector is located. The detector and the detection principle is explained in Section 4.2 in detail. Section 5.4 outlines the main goals of the thesis and what the simualtion results should be evaluated after. Simulations are an essential part of this work so the simulation environment is introduced. The most important tools and properties are introduced and explained. Also, the simulation principle behind this machinery is explained more detailed in Section 5.3. Section 5.4 describes the application of MEGAlib: the used model is shown as well as the mountain range surrounding the UFS. The inclusion of the surrounding structures is from utmost importance since this is affecting the resulting spectra and data which should be analysed.

The last chapter describes the simulation results which are analyzed. Section 6.1 first describes the probability of a thunderstorm occurring in a specific radius around the

UFS. Due to the fact that TGFs are connected to lightnings the occurrence of a thunderstorm is a necessary condition for measuring a TGF. The next section Section 6.2 evaluates the probability of a TGF to be measured by calculating the atmospheric transmittance. This is done for monochromatic energies and input angles. Section 6.3 compares different detector materials. Also, the difference between placing the detector in the Kugelalm or leaving the Kugelalm out is shown. By doing this it can be seen how strong the shielding effect of the Kugelalm affects the measurement. Section 6.4 analyses the resulting γ-ray spectrum for several input energies and input angle combinations. Also, the total amount of detected counts is evaluated both with and without the Kugelalm. By doing so, the spectral effect of the Kugelalm is visualized. Since this spectrum is the detector response it is important to see the expected signals for different energies and input directions. This leads to conclusions of TGF properties like favorable input energy and direction. Chapter 7 performs a time-resolved analysis of TGFs measured by Fermi-GBM. To gain insights about the TGF source a Bayesian analysis by utilizing the 3ML framework is performed with a fixed dataset. As a result, the parameter distribution of the TGF parameters are analyzed. Also, a powerlaw simulation with the determined parameters and the given Geomega setup is carried out. This spectrum is analyzed for the cases of implying atmospheric atetnuation or leaving it out. Finally, Chapter 8 shows the expected spectra of radioactive decays measured by the detector placed inside the Kugelalm. These spectra are compared to the powerlaw spectrum which describes the real signal to make conclusion if the natural radioactivity background needs to be taken into account.

3 Theoretical Background

The following chapter gives an overview about the theoretical background of the physics of thunderstorms, particle interactions, TGFs, natural radioactivity and the measurement site. This is necessary to understand the physical processes which are simulated in this thesis and to be able to interpret the results.

3.1 Physics of Thunderstorms and Electrical Processes

TGFs are deeply connected to thunderstorms and lightnings. In order to understand TGFs, we first need to lay down the theoretical groundwork regarding thunderstorms. The following chapter explains the physics behind the creation and the properties of thunderclouds as well as the formation of lightnings.

3.1.1 Structure and Development of Thunderclouds

A thunderstorm is a complex meteorological phenomenon, fundamentally consists of several distinct regions, and characterized by convective activity which are called *thunderstorm cells* [Britannica]. For these cells to be created they need to pass through three specific phases: The initial phase is called the *building phase* and starts with the formation of an ordinary cumulus cloud. At this point it is important to note that a necessary condition for thunderstorms to develop is the existence of an updraft of warm air which permeates the entirety of the cell but is counterbalanced by a gentle downdraft occurring in the surrounding environment. This creates a temperature

difference where the temperature is much higher inside the internal cloud than in the external atmosphere. Possible mechanisms for the rise of warm air can be topographic uplift due to the terrain or heating of a layer of air that's closer to the Earth's surface [Skybrary]. If this warm air ascends, a point of saturation is reached, leading to the formation of clouds, whereas the latent heat released during the condensation of atmospheric moisture further warms up the air. As the cells develop and continue to grow in size, an increasing volume of water condenses out of the updraft due to the temperature drop which accompanies the elevation to higher altitudes. As the temperature of these droplets drop below the freezing point with higher altitudes, they become supercooled and join togeter to form ice particles. If this accumulation of water becomes excessive in volume or in drop size, the resulting particles begin to precipitate and the next stage is initiated. The subsequent stage of a thunderstorm cell is initiated, which is called the *mature stage*. It starts with precipitation when the top of the cloud reaches great heights so that a downdraft starts to develop where previously the updraft existed. The falling rain thereby drags air down where it becomes more dense [Byers and Braham, 1948]. To properly understand the downdraft formation it is important to understand the mixing of a vertical air column with the ambient atmosphere. This mixing continues until the warmer updraft air inside the cloud has the same temperature lapse rate than the environment. The lapse rate describes the rate at which an atmsopheric parameter falls with increasing altitude. In this case this means that the mixing continous until the temperature drop rate inside and outside the cloud are equal. With the falling rain and the downdraft, additional air is added to the downstream, mostly from outside of the cloud, as long as sufficient rain remains [Byers and Braham, 1948]. To sum it up, the entire thunderstorm cell has convergent flow with divergent outflow at the base of the cloud and the very high altitudes between 10 km – 14 km. When the rain falls down the air is cooled down and friction between the ice particles carried by the updraft and the ice particles descending through the cloud appears. This friction creates a static field where the positive charge moves to the top of the cloud, whereby the negative charge is at the bottom of the cloud. Afterwards, the top of the cloud flattens out to a Cirrus like cloud, giving it an anvil shape [Skybrary].

The final phase of the thunderstorm cell is referred to as the *dissipation* or *anvil phase*. It is characterized by the widespread distribution of the downdraft across the lower levels of the cell, leading to a lower importance of the updraft activity. At this point, there is negligible vertical motion in higher levels since the entire lower levels at altitudes between 1 km and 3 km of the cell have a slight downdraft. This slight downdraft will persist and remain for as long as precipitation continues to fall from the cloud. Once the rainfall stops, the previously dominating large-scale vertical movements dissipate,

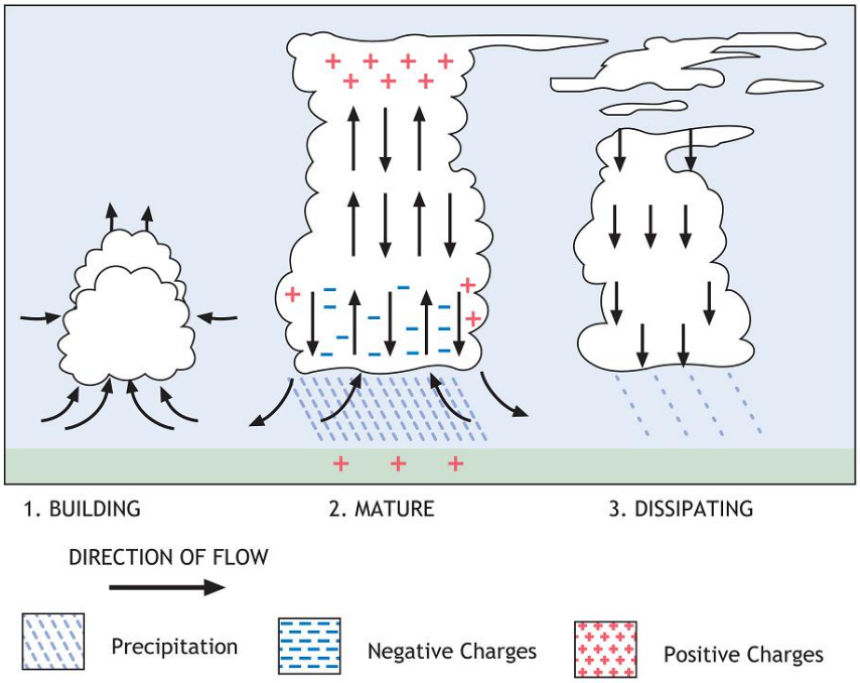

Fig. 3.1: The life cycle of a thundercloud. Phase one (left) is the building phase where by updrafts of warm air and condensation of water the thundercloud is created. Phase two (middle) is called the mature stage where the cloud starts to cause precipitation. Here, the upper part of the thundercloud is developed and with a downdraft, the charge is separated in a way that a potential difference appears. The last phase (right) is called dissipating phase. There is no more motion in the upper part of the cloud so that the borders dissolve. Also, the downdraft is getting slower, keeping on as long as the rain is falling [from Skybrary].

resulting in the boundaries of the cell becoming indistinct and difficult to differentiate [Byers and Braham, 1948]. The entirety of this process is summarized in Fig. 3.1 while the basic structure of a thundercloud is shown in Fig. 3.2.

3.1.2 Charge Distribution in Thunderclouds

One of the simplest but also most spread pictures of the charge distribution in thunderclouds is the *tripole model* [Dwyer and Uman, 2014]. This model contains a main negative charge in the center of the thundercloud, a main positive charge center on the top of the cloud and a small positive charge distribution on the bottom, below the negative charge. This main structure is visualized in Fig. 3.3. The separation of charged particles is thought to originate from slow hydrodynamic processes inside the thundercloud like updraft currents or advection. While the updraft drags small and

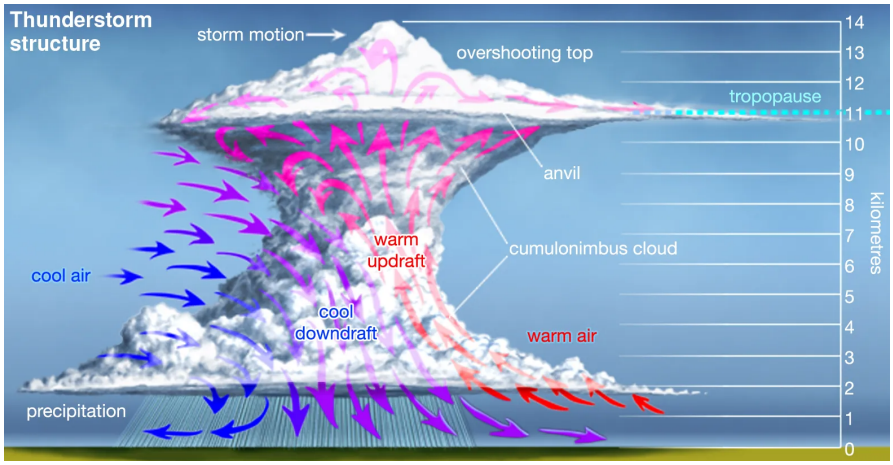

Fig. 3.2: A towering thundercloud is created when the atmosphere is forming strong updrafts and downdrafts, as indicated by the arrows. It can happen that the updrafts are strong enough to extend the top of the thundercloud so that the cloud is extended into the tropopause, which is the upper limit of the troposphere. A typical scale with altitudes at which the clouds stay is given [from Britannica].

light positively charged ice fragments, heavy negatively charged hailstones preferably fall downward due to gravity [Surkov and Hayakawa, 2012a]. A central part of this mechanism is the generation of free electrons by either collisions between ice particles and atmospheric molecules or through external sources like cosmic rays. Since the current inside the cloud goes upward but is approximately zero outside, a charge separation occurs. The current inside of the cloud works as a battery for the generation of upward- or downward-directed lightning discharges. Due to this current, the lightning can be operative as long as the current inside can separate the charges and provide the top of the thundercloud with enough positive charges. The so called fair weather current outside is a weak current flowing to the ground [Surkov and Hayakawa, 2012a]. Apart from these three main charges the surrounding air can be seen as an additional fourth negative screening charge layer because the air outside the cloud has a higher conductivity compared to the air inside of the cloud. The reason for this is the quick attachement of the free electrons to ice particles or atomic molecules inside of the cloud [Dwyer and Uman, 2014].

As a consequence of this 'stacked' model there is a temperature difference across the single layers. Depending on the height of the thunderstorm itself, the size of the charge layers can vary. The thickness of the positive upper layer can range between about 8–15 km in summer storms and about a few km in winter storms [Dwyer and Uman, 2014].

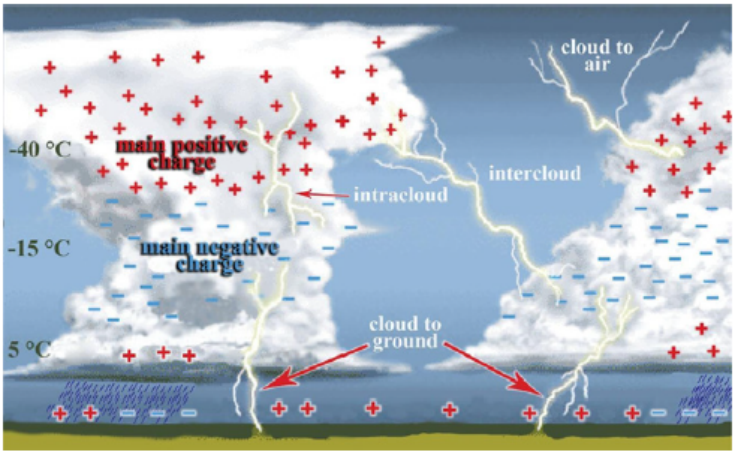

Fig. 3.3: Different lightning types. The picture shows: cloud-to-air, intracloud, intercloud and cloud-to-ground lightning [Dwyer and Uman, 2014].

3.1.3 Streamer and Leader Formation

As described in the section above there is charge separation in a thundercloud, which leads to free electrons. These free electrons quickly attach to oxygen molecules, forming negative ions. Before undergoing 2-body or 3-body attachment processes, the electrons experience multiple scatterings with the surrounding air molecules. These attachment processes describe the capture of free electrons by neutral molecules to create negative ions. Since this capture does not happen immediately, the electrons travel with a constant average velocity as they experience scattering. By increasing the electric field due to the charge separation inside the cloud, the velocity of the electrons also increases, so at large enough fields, a fraction of electrons will have enough energy to ionize the air. This ionization is mostly due to the impact of the electrons with the air molecules which then creates additional electrons [Dwyer and Uman, 2014]. For small electric fields the number of free electrons rapidly subsides, since the growth in the number of electrons competes with its decrease because to attachment processes. For higher electric fields the ionization rate surpasses the attachment rate. This happens at around $E_k = 3 \times 10^6\,\mathrm{V\,m^{-1}} \times n_{\mathrm{air}}$ which is called the conventional breakdown field where $n_{\mathrm{air}} = N_{\mathrm{air}}/N_{\mathrm{STP}}$. N_{air} is the number density of air and N_{STP} is the number density of air at standard temperature and pressure (STP). For electric fields $E > E_{\mathrm{k}}$ the number of electrons grows exponentially with time and distance along the direction of the electric field. As a starting condition for this effect, there needs to be a high energy seed electron which has the function of starting the electron avalanche. This seed electron could have different origins, such as cosmic rays, natural radioactivity, or

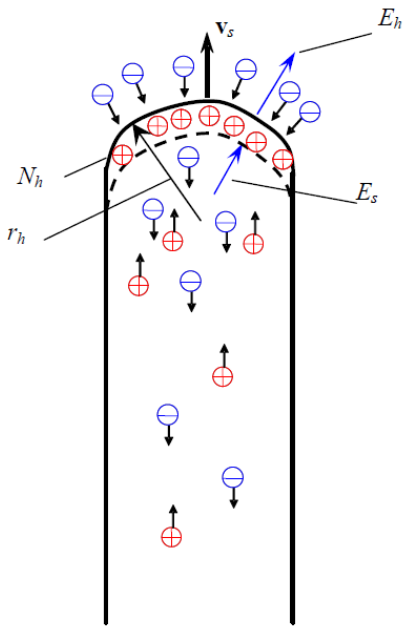

Fig. 3.4: The model of a positive streamer where ν_S is the streamer velocity, r_h is the streamers heads curvature radius, N_h is the number density of uncompensated positive charges, E_h is the electric field in front of the streamer head and E_S is the electric field inside of the streamer. Taken from [Surkov and Hayakawa, 2012a].

solar particle events [Dwyer and Uman, 2014, Dwyer et al., 2012].

The increasing number of electrons polarizes the medium, and this polarization enhances the electric field at the avalanche front, accelerating its growth. Because the avalanche carries the high field required for avalanche multiplication it is able to self-propagate into lower ambient fields. This self-propagating structure is then called a *streamer* [Dwyer and Uman, 2014, Surkov and Hayakawa, 2012a]. Streamers can have lengths of about several meters with a propagation velocity of about $10^5\,\mathrm{m\,s^{-1}}$ and consist of a propagating compact volume of positive space charges, called the 'tip'. The tip is followed by a tail of negligibly conducting plasma with low conductivity, which prevents it from a complete breakdown [Petersen et al., 2008]. Even though the streamers appear because of high electric fields, their current is mostly weak and in the range of microamperes [Dwyer and Uman, 2014, Mazur, 2016]. The typically high currents occuring in lightnings are not measured in the streamer which describes the tip of the lightning channel but in the plasma channel behind the streamer. The currents in these plasma channels reach up to 15 A – 2.1 kA [Mazur, 2016]. As seen in Fig. 3.4, which shows a positive streamer, the charge density is larger at the streamer tip. This density can be so large that the electric field in the vicinity of the head can reach values of up to 4 – 7 times the value of E_k. Since the streamer carries a charge there are two

types of streamers depending on the charge they carry: positive and negative streamers. While negative streamers propagate due to ejection of electrons from its head, positive streamers propagate due to injections of seed electron avalanches from surroundings. The seed electrons therefore can be created just by the high rate of impact and photoionization caused by the strong electrical field of the tip which is due to the spatial charge of the head [Surkov and Hayakawa, 2012b]. Also, the electric field for initiating positive or negative streamers are different. Positive streamers need a minimum critical field of $E_{\mathrm{cr}} = 440\,\mathrm{kV/m}$ at ground pressure and $E_{\mathrm{cr}} = 150\,\mathrm{kV/m}$ at an altitude of 6.5 km. In contrast, the critical field for negative streamers is more than twice as high with $E_{\mathrm{cr}} = 1250\,\mathrm{kV/m}$ at ground pressure and $E_{\mathrm{cr}} = 300\,\mathrm{kV/m}$ at 6.5 km altitude. This larger electric field for sustaining the negative streamer is due to the self-diffusing nature of the discharge [Petersen et al., 2008]. Because of this, the probability for positive streamers in low ambient fields, which are in the order of magnitude of E_{cr}, is way higher compared to negative streamers.

A necessary criterion for the transition of an electron avalanche to become a streamer is the radius of the avalanche region to enhance the electric field with a localized space charge and the critical number of avalanching electrons. When these streamers then propagate through high electric fields, the charge accumulates at the tip of the streamer and may become sufficiently large enough that the streamer splits up into two or more streamers. This may repeat so that at the end a network of positive and/or negative streamers is created. The number of corresponding electrons is then at the order of $10^8 - 10^9$ for a single leader or in the range of $10^{16} - 10^{19}$ for a streamer system [Montijn and Ebert, 2006, Wada et al., 2025].

If the currents produced by the streamers are large, another effect occurs: the streamer heats the air, which increases the conductivity, allowing more current to flow, which again causes more heating, and the whole process repeats itself. This instability leads to a concentration of the current along a small hot channel in the air since the resistance is the smallest in the center of the path. For temperatures $T > 1500\,\mathrm{K}$ the conductivity of the air quickly rises due to the rapid detachment of electrons from negative ions. For high electron densities and temperatures we can then see thermalization, as well as impact ionization between ions and neutral particles, that becomes important. These narrow hot channels with temperatures of 5000 K or higher are often called *leaders* which are a prerequisite for lightnings [Dwyer and Uman, 2014]. The final stage of the leader process occurs when the downwards facing leader connects with an upward directed dischrage. This contact results in a short circuit occuring between the Earth and cloud discharge. Even though the electrons move downward, the current and the luminosity have an upward direction of propagation due to the already ionized path

of the preceding leader [Dwyer and Uman, 2014]. When a return stroke occurs, the air in the lightning channel gets suddenly heated to 30 000 °C which expands the air and creates a shock wave. This shockwave is audible as thunder. The peak current for the first return stroke is at the order of 30 kA with possibly reaching up to 300 kA in positive lightning discharges. There is also the possibility of multiple return strokes, seperated by time intervals of 40 – 50 ms [Dwyer and Uman, 2014, Mazur, 2016]. There are different types of leaders being generated in lightnings: stepped leader, dart leader, and bidirectional leader, as explained in the following and visualized in Fig. 3.5.
A stepped leader is a type of electrical discharge in a gas, characterized by an expanding filament of hot, highly electrically conductive gas preceded at its tip. This type of leader is the initial discharge for Cloud-to-Ground (CG) discharges [Dwyer and Uman, 2014, Petersen et al., 2008]. The movement of the stepped leader is not continuous but rather in discrete luminous segments of tens of meters of length for a duration of a microsecond. After a short pause the next step joins and so. This short pause between two steps is in the range of 10 – 100μs [Dwyer and Uman, 2014]. The movement of the steps works as follows: negative leaders produce steps by creating a plasma channel in the volume front of an old leader channel which is then called a space stem. This space stem thermalizes and becomes a space leader which evolves bidirectionally with the positive end, moving backward to the main leader and the negative end propagating forward, extending the leader tip. Afterwards the positive space leader merges with the tip of the negative leader. When the space leader connects with the primary leader, its current will traverse upwards regarding the leader channel direction, completing the step process [Dwyer and Uman, 2014].
A dart leader is a leader which propagates continuously along the defunct return stroke channel. Due to the fact that they move along the main channel of the ionized preceding leader channel they are responsible for the subsequent return strokes in lightning bolts and therefore they are the reason for multi-stroke lightnings. They move with a velocity of around $10^7\,\mathrm{m\,s^{-1}}$ and deposit not as much charge as the stepped leader [Dwyer and Uman, 2014].

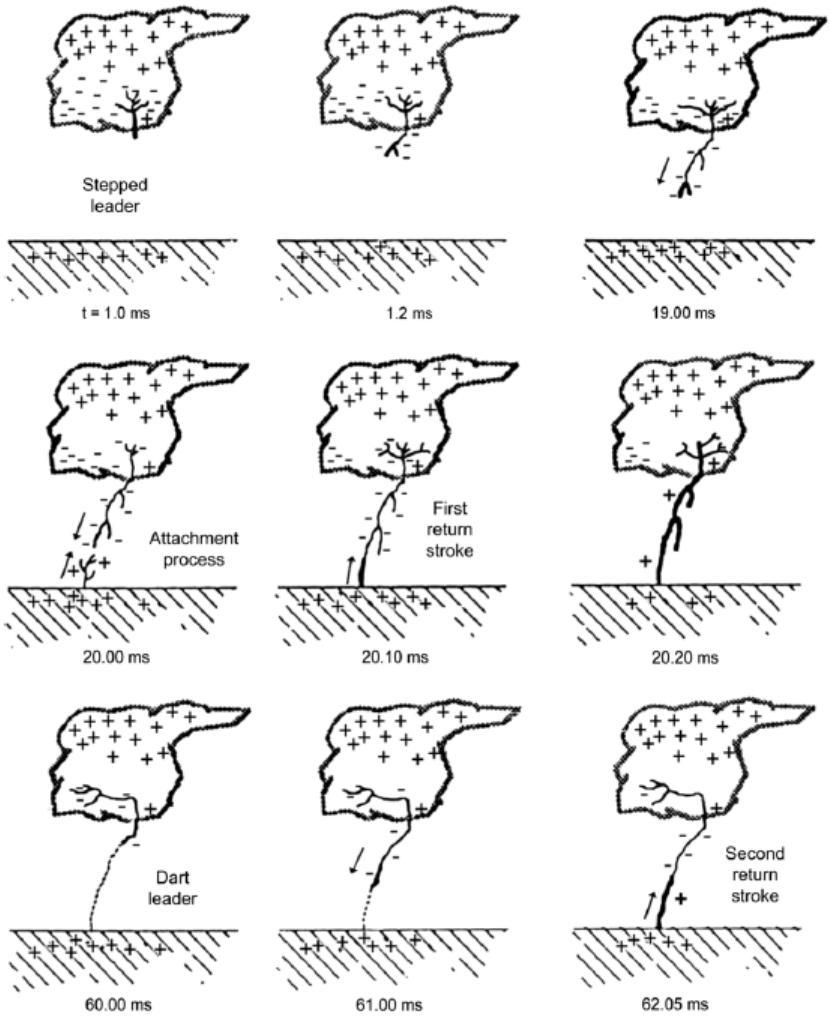

Fig. 3.5: A negative leader propagates from a charged cloud to the ground (CG lightning). The principle of a stepped leader is shown since the lightning stroke moves in different distinct steps. After the return stroke propagated back to the cloud and leaves behind an ionized channel the dart leader travels through this channel back to the ground. This results in a second return stroke, showing how multiple stroke lightnings are created. Taken from [Dwyer and Uman, 2014].

3.1.4 Lightning Phenomenology

To characterize lightnings, we need to differ between two cases: lightnings that bridge the gab between cloud and Earth which are called *CG lightning* and those that do not. Those who will not cross the gap are called *cloud discharges*. We can specify these further: if the lightnings happen to appear inside one cloud they are called *intracloud lightning*, if they occur between two clouds they are called *intercloud lightning*, and if they start in a cloud but end in the air they are called *cloud-to-air lightnings*. These four types of lightnings are illustrated in Fig. 3.3.
There are four different types of lightning flashes occurring between thunderclouds and Earth, shown in Fig. 3.6.

There is a difference in the lightning charge and leader propagation direction. In about 90% of the cases the lightning has negative charge and a downward-propagating leader while the other 10% have a positive charge and a downward-propagating leader. The cases for upward-propagating leaders are rather uncommon – they are mostly initiated

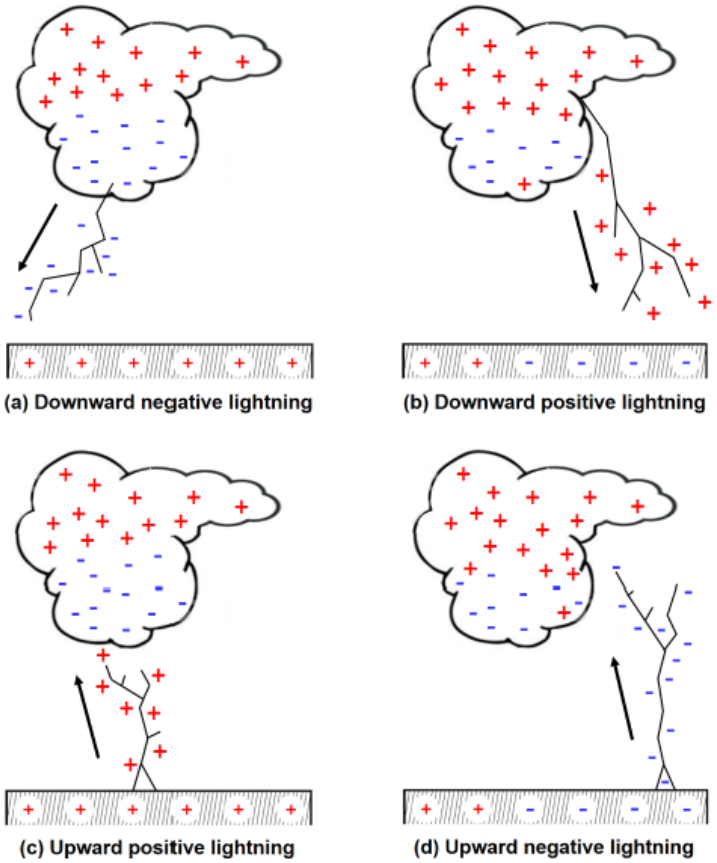

Fig. 3.6: Different types of cloud-to-ground lightnings. Taken from [Bedoui, 2019].

at manmade objects like tall towers or similar, towards the charged clouds [Dwyer and Uman, 2014]-

It was discovered that these positive CG lightning discharges lower positive charges from clouds to ground and then can trigger further processes, so-called transient luminous events (TLEs) [Surkov and Hayakawa, 2012a]. TLEs are large-scaled optical events which occur at altitudes between 40 km and 90 km and are directly related to the thunderstorm below. Depending on their properties, they can be separated in different types such as Sprites, Blue jets, Elves and recently discovered Blue starters and Gigantic jets. The different types of TLEs are shown in Fig. 3.7 and their properties are summarized in Tab. 3.1 [Kim et al., 2018].

Type	**Duration (ms)**	**Size (km)**	**Velocity (km/s)**	**Altitude (km)**
Blue jets	up to 250	3 – 20	12	20 – 40
Gigantic jets	less than 1	20 – 30	70 – 90	70 – 90
Sprite	1 – 10	25 – 50	10^4	40 – 90
Elves	less than 1	over 300	10^5	84 – 87

Table 3.1: Properties of different types of TLEs.

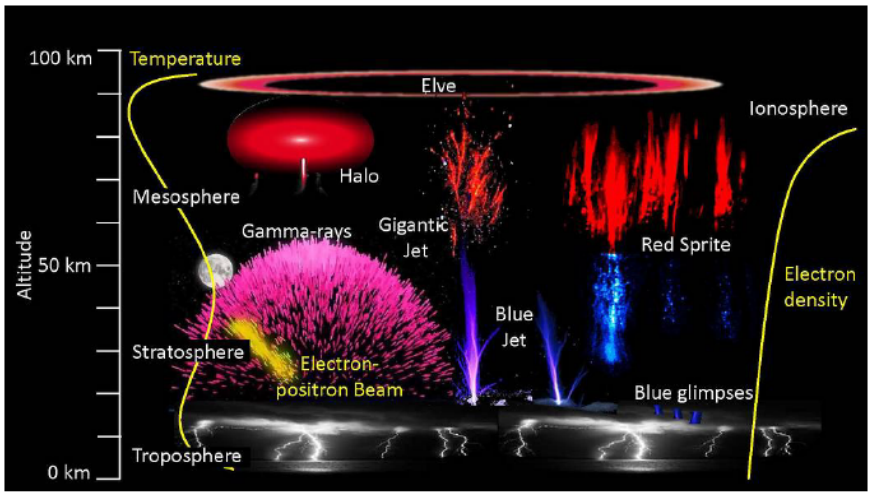

Fig. 3.7: Different types of TLEs. Taken from [Kim et al., 2018].

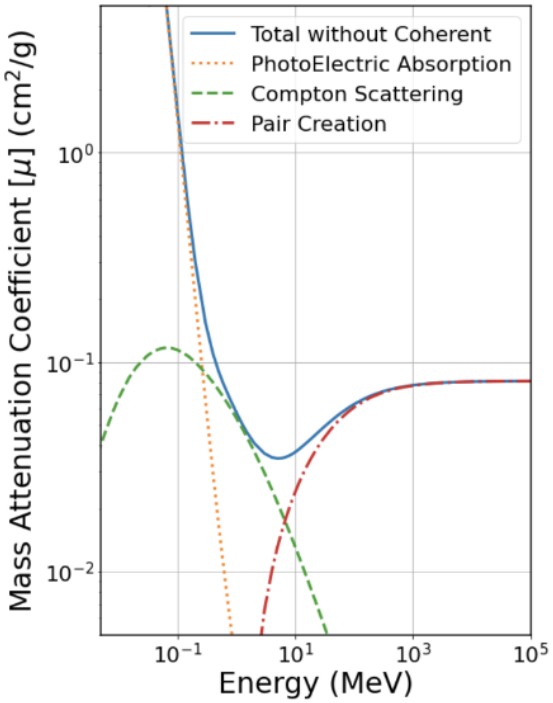

Fig. 3.8: The mass attenuation coefficient shown for sodium iodide (Tellur doped). The resulting summed up graph consists of the three processes: photoelectric absorption, Compton scattering and pair production. Taken from [Kierans et al., 2022].

3.2 Photon - Matter Interactions

When we want to detect photons they need to interact with matter - either with the surrounding matter or with the detector material itself. These interactions happen in different ways, which is shown in Fig. 3.8. In this section these interactions between photons and matter and the relating processes are shown and described in detail.

3.2.1 Photoelectric Absorption

Fig. 3.8 shows that for low-energy photons $E \ll m_e c^2$ where $m_e c^2$ is the rest energy of an electron, the dominant interaction process in NaI is photoelectric absorption. In this process a gamma ray is interacting with a bound atomic electron in a way that it transfers all of its energy to the electron. Some of the energy is used to overcome the electron binding energy and most of the remainder is transferred to the electorn

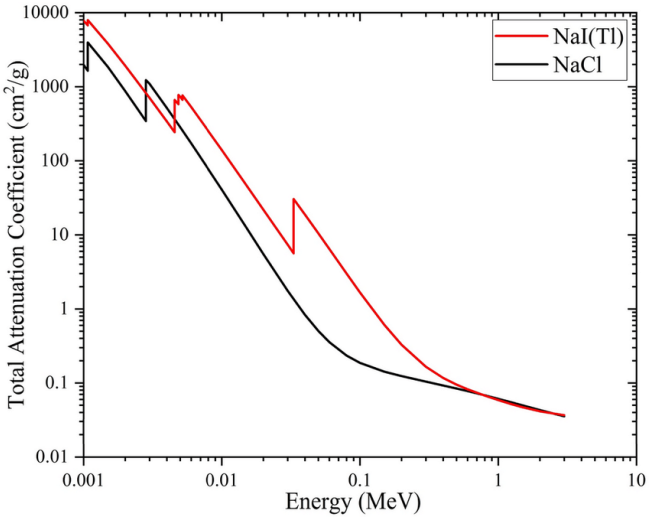

Fig. 3.9: Photoelectric mass coefficient of NaI. It is seen that the lowest shell (K shell) appears at the highest input energy and the outermost shell has the lowest input energy. This is due to the fact that the binding energy is lower for outer shells so the electrons can be released more easily. Since there are more electrons in outer shells the mass attenuation coefficient is higher for lower energies. After a shell is emptied, μ decreases until the input energy is high enough to overcome the binding energy from the electrons in the next shell. Taken from [Farzanehpoor Alwars and Rahmani, 2021]

as kinetic energy while a very small amount of the incident photon energy is used to conserve momentum and therefore remains as recoil energy with the atom. This so called *photoelectron* is then ejected with an energy of

$$E_{e^-} = \hbar\omega - E_b \tag{3.1}$$

where E_b is the binding energy of the electron [Karpius and Reilly, 2024]. The probability of this process happening strongly depends on the input energy of the photon and the atomic number of the material. The more tightly an electron is bound, the higher the probability is that a photon is interacting with this electron. Knowing this, the K-shell electrons are the most likely to participate in this process. So, if the photon energy is slightly above the binding energy for K-shell electrons but below the electron rest energy, the cross-section is given by

$$\sigma_{\text{Photoabsorption}} = \frac{32\pi\sqrt{2}\alpha^4 r_e^2 Z^5}{3}\left(\frac{m_e c^2}{\hbar\omega}\right)^{\frac{7}{2}} \tag{3.2}$$

where $\alpha = 137^{-1}$ is the fine structure constant, $r_e = 2.818 \times 10^{15}\,\text{m}$ is the electron radius, Z is the atomic number, $m_e =$ is the electron mass and $\hbar\omega$ is the photon energy

[Leo, 1994, Dwyer and Uman, 2014].
At lower energies, electrons from multiple atomic shells also contribute to the interaction. Generally, the attenuation coefficient μ increases as the incident photon energy decreases. This trend is characterized by absorption edges: as soon as the energy exceeds the binding energy of a more deeply bound inner shell, μ increases abruptly. Between these edges, μ decreases with increasing photon energy until the threshold of the next inner shell is reached. The linear attenuation coefficient μ is directly proportional to the cross-section through $\mu = n\,\sigma$ where n is the number density. This procedure is shown in Fig. 3.9 [Longair, 2014].
The complete absorption of the photon energy is the physical basis for the photopeak which can be observed in γ-ray spectroscopy. Since during photoelectric absorption the entire energy is deposited into the detector material, the resulting signal corresponds to the total energy of the incident gamma ray.

3.2.2 Compton Scattering

Compton scattering describes the interaction of a photon with a free or weakly bound electron, so $E_\gamma \gg E_b$. The photon transfers part of its energy to the electron so that the outcome of this interaction is a scattered photon and a free electron (Fig. 3.10). When the electron is not bound tightly, photoelectric absorption is forbidden, and only Compton scattering is allowed since the atom cannot absorb the recoil energy. Because of energy and momentum conservation just a partial energy transfer is possible and allowed [Karpius and Reilly, 2024].

Knowing that weakly bound electrons are needed for Compton scattering we know that this process preferably happens at the outer shell electrons and after the interaction the electron becomes a free electron with energy

$$E_{e^-} = E_\gamma - E_{\gamma'} \tag{3.3}$$

where E_γ is the energy of the input photon and E'_γ the energy of the scattered photon. The energy of the scattered photon can be calculated with

$$E_{\gamma'} = \frac{m_e}{1 - \cos\theta + \frac{m_e}{E_\gamma}} = \frac{E_\gamma}{1 + \frac{E_\gamma}{m_e}(1 - \cos\theta)} \tag{3.4}$$

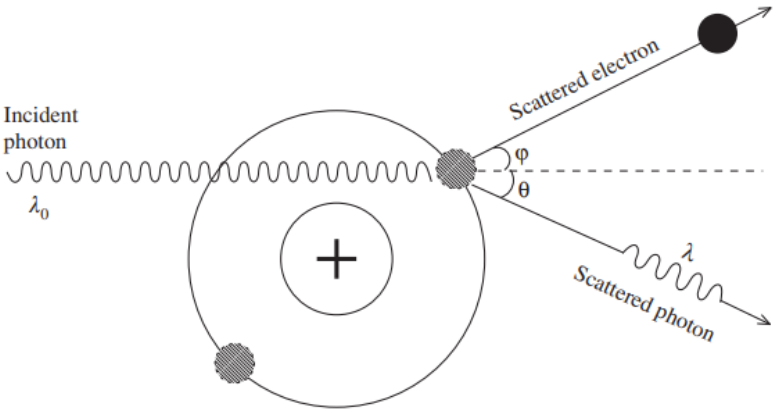

Fig. 3.10: Compton scattering of a photon with incident energy $E_0 = \frac{hc}{\lambda_0}$ at a bound electron. The result is a scattered electron and a scattered photon of energy $E_0 = \frac{hc}{\lambda}$ [Ahmed, 2015].

where θ is the angle between the incoming and the scattered photon. Depending on how much energy is transferred during the interaction the direction of the electron and the scattered photon do change [Nelson and Reilly, 1991].
According to Equation (3.4), the minimum energy occurs during a collision where the scattering angle becomes $\theta = 180°$ and the electron moves in the same direction as the incident photon. The other extreme of scattering occurs at a very small angle ($\theta \approx 0°$). In this case, the energy of the scattered photon is very close to the incident energy so the scattered electron barely absorbs energy from this interaction [Karpius and Reilly, 2024]. For $E_\gamma \gg \frac{m_e}{2}$ the resulting minimum and maximum energies of the scattered photon are

$$E_{\gamma'}^{\min} = \frac{m_0 c^2}{2} \quad \text{and} \tag{3.5}$$

$$E_{e^-}^{\max} = E_\gamma - \frac{m_0 c^2}{2} \tag{3.6}$$

The cross section for this process can then be calculated with the *Klein-Nishina* formula:

$$\frac{d\sigma}{d\Omega} = \frac{r_e^2}{2} \frac{1}{(1+\gamma(1-\cos\theta))^2} \left(1 + \cos^2\theta + \frac{\gamma^2(1-\cos\theta)^2}{1+\gamma(1-\cos\theta)}\right) \tag{3.7}$$

where $\gamma = E_\gamma / m_e c^2$ and r_e is the classical electron radius. The cross section for Compton scattering can be achieved by integrating over the solid angle $\mathrm{d}\Omega$ and gives [Leo, 1994]

$$\sigma_c = 2\pi r_e^2 \left(\frac{1+\gamma}{\gamma^2}\left(\frac{2(1+\gamma)}{1+2\gamma} - \frac{1}{\gamma}\ln(1+2\gamma)\right) + \frac{1}{2\gamma}\ln(1+2\gamma) - \frac{1+3\gamma}{(1+2\gamma)^2}\right). \tag{3.8}$$

Closely related to Compton scattering are *Thomson scattering* and *Rayleigh scattering* - the difference is that in these processes there is no energy transfer but a directional change of the incoming photon. Thomson scattering describes the scattering of photons off of free electrons and the cross section can be calculated from the Klein-Nishina formula for small energies:

$$\sigma_T = \frac{8\pi}{3} r_e^2 \tag{3.9}$$

On the other hand, Rayleigh scattering is the scattering of photons at atoms and its cross sections is

$$\sigma_R = \frac{24\pi^3 k^4}{N^2} \left(\frac{n_k^2 - 1}{n_k^2 + 2} \right)^2 F_g(k) \tag{3.10}$$

where k is the wavenumber of light, N is the number density of gas, n_k is the wavenumber dependent real refractive index and $F_g(k)$ is a factor which accounts for depolarization [Thalman et al., 2014].

3.2.3 Pair Production

The process known as pair production can be described as a high-energy photon undergoing the creation of a electron - positron pair. In order for this event to occur, it is necessary that the photon possesses an energy threshold of 1.022 MeV since $E_\gamma > 2\, m_e\, c^2 = 1.022\,\text{MeV}$. This process is only possible in the presence of an electric field, which is typically provided by the nucleus of an atom. Now we can differ between two distinct scenarios: the case to which we refer to as *intermediate photon energies* and the one where the photon energies are in the *ultra-relativistic limit*. For the intermediate energy range, the pair production process occurs at distances from the nucleus where the electrostatic screening through atomic electrons can be neglected. This absence of screening is valid when the photon energy satisfies the condition $1 \ll \hbar\omega/m_e c^2 \ll \alpha^{-1} Z^{\frac{1}{3}}$. In this regime, the photon energy is sufficient to probe the nuclear field directly, yet remains low enough that the electron cloud does not significantly shield the nuclear charge [Longair, 2014]. The cross section for this interaction is given by:

$$\sigma_{\text{Pair}} = \alpha r_e^2 Z^2 \left(\frac{28}{9} \ln\left(\frac{2\hbar\omega}{m_e c^2} \right) - \frac{218}{27} \right) \tag{3.11}$$

Full photon screening is present at $\hbar\omega/m_e c^2 >> \alpha^{-1} Z^{\frac{1}{3}}$ and describes the scenario where the nuclear charge is completely shielded by the atomic electron charge, which results in the reduction of the effective interaction strength and cross-section. The cross

section then becomes

$$\sigma_{\text{Pair}} = \alpha r_e^2 Z^2 \left(\frac{28}{9} \ln \left(\frac{183}{Z^{\frac{1}{3}}} \right) - \frac{2}{27} \right) \tag{3.12}$$

3.2.4 Atmospheric Absorption Effects

If a TGF created in a thundercloud is to be measured on Earth there is a probability for these γ-rays to be attenuated or absorbed while traveling through the atmsophere. The transmissivity for γ-rays to traverse the atmosphere and reach the detector can be described by

$$T_{\text{atm}}(\theta, \mathrm{E_{in}}) = \exp\left(-\frac{1}{\cos\theta} \mathrm{H} \rho_0 \mu(\mathrm{E_{in}}) \mathrm{e}^{-\frac{\mathrm{h_D}}{\mathrm{H}}} \cdot \left(1 - \mathrm{e}^{\frac{-\mathrm{d}\cos\theta}{\mathrm{H}}} \right) \right) \tag{3.13}$$

where θ describes the zenith angle which is the angle between zenith direction and upwards oriented z-axis. E_{in} is the initial energy of the incoming photon, d represents the spatial separation between the TGF source and the detector, H = 8500 m is the constant scale height of the atmosphere, ρ_0 is the air density at sea level, μ(E) describes the energy dependent mass attenuation coefficient and h_{D} is the altitude at which the detector is placed. μ(E) was determined through [Mass attenuation coefficient] where the input atmospheric components were set to N (78.084%), O_2 (20.946%), Ar (0.934%) and CO_2 (0.036%). Fig. 3.11 shows the transmissivity for different input angles θ. This equation includes the exponential decay of the air density which occurs with increasing altitude. In addition to this transmission probability there are atmospheric absorption effects which highly influence the measurement of TGFs on Earth-based stations, especially regarding the attenuation of the flux, the change of the energy spectrum or the creation of secondary effects like photoneutrons. This attenuation is strongly dependent on the column density $I(z) = \int_z^\infty \rho \, dz$ where z is the altitude and ρ is the mass density of air.

Another effect is the modification of the γ-ray energy specturm after traveling through the atmosphere. For ground-based observations it is mostly the low-energy photons which are strongly attenuated before reaching the detector. As a consequence, the signal primarily consists of photons with energies above 1 MeV unless the event is very nearby which was found by GEANT4 simulations [Abbasi et al., 2019]. Also, the estimated time of arrival at the detector for the photons is broadened. Low-energy photons have a longer accumulated path length than high-energy photons due to multiple Compton

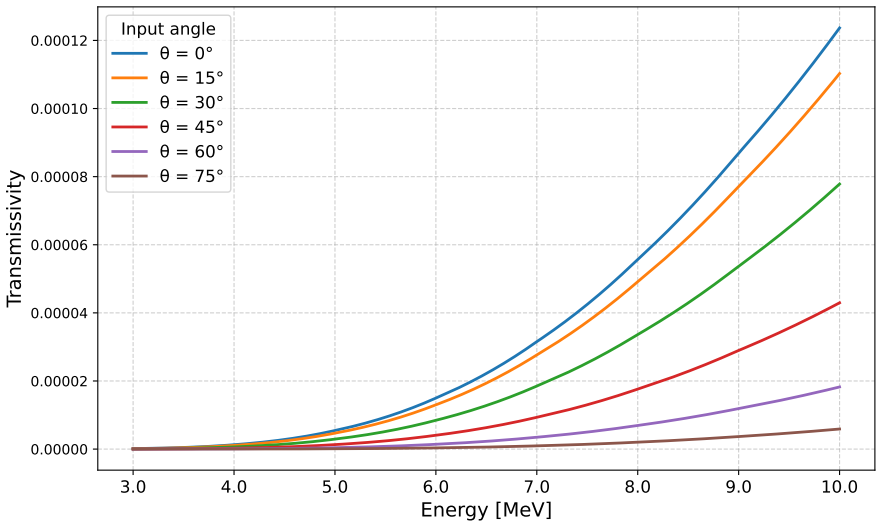

Fig. 3.11: Transmissivity calculated with Equation (3.13) for different input angles θ. The density of air is set to $\rho_0 = 1.225\,\mathrm{kg\,m^{-3}}$, the detector altitude is fixed to $h_{\mathrm{det}} = 2657\,\mathrm{m}$ and the vertical distance between detector and TGF source is set to $\mathrm{d} = 7434\,\mathrm{m}$, locating the source at an altitude of 10 km. The energy dependent mass attenuation coefficient $\mu(E)$ is taken from [Mass attenuation coefficient].

scatterings which results in dispersed arrival times. Time delays of up to 100 ms can be observed for TGFs created below 20 km which is quite important since TGFs exist on such short time scales. However, this time delay is way smaller for ground-based observations since the photons dont need to travel hundreds of kilometers to be detected. If the TGF contains enough high energy photons with energies $E > 10\,\mathrm{MeV}$ there is a chance for photonuclear reactions happening in the atmosphere such as $^{14}\mathrm{N} + \gamma \rightarrow {}^{13}\mathrm{N} + n$ and $^{16}\mathrm{O} + \gamma \rightarrow {}^{15}\mathrm{O} + n$. This reaction creates fast neutrons and after these are thermalized by mainly elastic scatterings with ^{14}N, neutron capture happens through the reaction $^{14}\mathrm{N} + n \rightarrow {}^{15}\mathrm{N}$. The isotope ^{15}N is an excited state so it immediately emits nuclear γ-rays and de-excites within picoseconds [Lieb, 1966]. A measurable burst of decaying γ-rays is called TGF afterglow which is dependent on the timescale of the thermalization but typically lasts for about 200 ms [Wada et al., 2019a, 2025]. These photonuclear reactions are illustrated in Fig. 3.12.

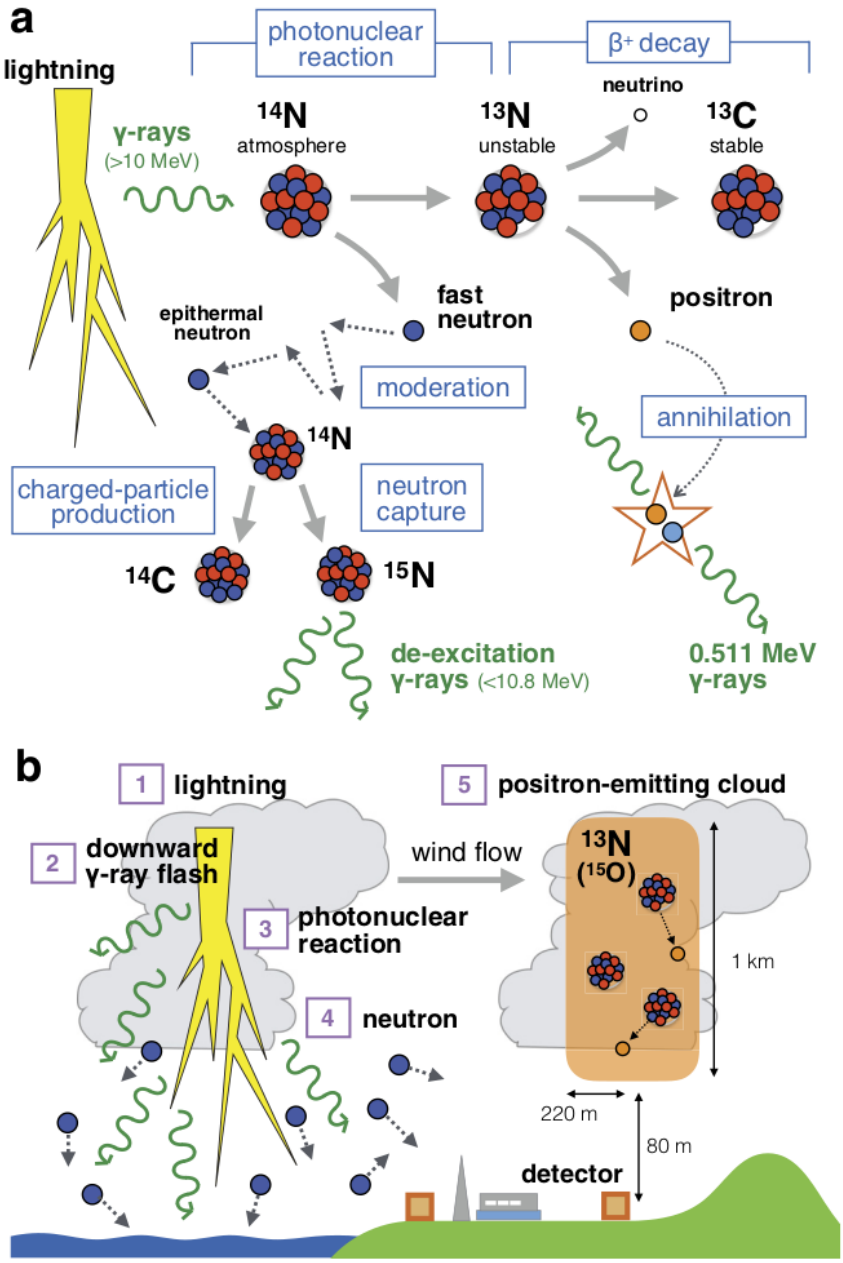

Fig. 3.12: (a) Possible photnuclear processes happening during a lightning discharge. (b) Drift of the positron-emitting cloud and diffusion of neutrons which are produced in photonuclear processes during lightning discharges. Taken from [Enoto et al., 2017].

3.3 Terrestrial Gamma-ray Flashes

In this chapter, an overview of TGFs is given and their physical properties and production mechanisms are described in detail. Previous measurements and works are explained, especially these with comparable setups and assumptions.

3.3.1 Overview and Physical Properties

TGFs are characterized as intense bursts of gamma rays on a sub-millisecond timescale, representing the most intense radiation generated naturally on Earth. These bursts are believed to originate from thunderclouds within the Earths atmosphere and are predominantly detected by satellites [Hongbo et al., 2019b, Wada et al., 2019b]. The initial measurement of TGFs was conducted by Fishman et al. [1994], utilizing the Burst And Transient Source Experiment (BATSE), which was mounted on the Compton Gamma Ray Observatory (CGRO) [Dwyer and Uman, 2014]. Initially, TGFs were mistakenly associated with Sprites occurring at altitudes exceeding 30 km. This association was later disproved by Dwyer et al. [2005] and it was shown that they originate from thunderclouds at comparatively lower altitudes of around 10 – 15 km. While TGFs are primarily observed by satellites like the Reuven Ramaty High Energy Solar Spectroscopic Imager (RHESSI), the Fermi Gamma-ray Burst Monitor (GBM), the Astro-rivelatore Gamma a Immagini Leggero (AGILE) or the Atmosphere-Space Interactions Monitor (ASIM), as used by Skeie et al. [2022] and Liu and Dwyer [2013], they are associated with the leaders of mostly intracloud lightning discharges occurring near the top of the thunderclouds. There have also been reports of their detection at ground level or at altitudes typical for aircrafts at around 10 km – 15 km [Wada et al., 2019b, Abbasi et al., 2019, Paras and Pooja, 2021, Dwyer and Uman, 2014].
TGFs are primarily generated within thunderclouds or just above at altitudes ranging from 9 km to 21 km which is part of the tropopause as seen in Fig. 3.2. One reason for this observation is the presence of spectral characteristics that are incompatible with sources originating from greater altitudes (> 21 km) [Skeie et al., 2022]. Interstingly, downward-directed TGF are more frequently located at considerably lower altitudes, such as those documented during winter storms in Japan which have altitudes of around 2.5 km [Wada et al., 2019b]. In the initial measurement conducted with BATSE, the duration of TGFs was approximated to be within the millisecond range. However, it

was subsequently discovered that these findings were adversely affected by the substantial dead-time and trigger bias of the measurement instruments. Further investigations revealed that the duration of TGFs varies from approximately 10 μs to several hundred μs with a median TGF pulse duration of 100 μs [Dwyer and Uman, 2014]. TGFs consist of either a single pulse or multiple pulses, as shown by later experimental results [Dwyer et al., 2017]. The fluency of those events is approximately 0.1 ph cm^{-2} at an altitude of 500 km. This suggests a number of runaway electrons originating from the thunderclouds source, estimated to be around 10^{17} [Dwyer et al., 2012, 2017].
An analysis of the cumulative spectrum of 100 recorded AGILE TGFs indicates the presence of a high-energy power-law component up to an energy of about 40 MeV. The spectrum for higher energies is not further consistent with that predicted by the Relativistic Runaway Electron Avalanche (RREA) process followed by bremsstrahlung emission [Dwyer et al., 2012, Marisaldi et al., 2013]. The RREA model predicts an average energy of the runaway electrons at around 7.3 MeV and with this a strong decline for energies surpassing 40 MeV [Liu and Dwyer, 2013]. In comparison to the spectra of Gamma Ray Bursts (GRBs), other cosmic sources and solar flares, the spectrum of TGFs has been acknowledged to exhibit significantly harder characteristics than those of other sources, i.e. a powerlaw spectral index of >1.0 [Marisaldi et al., 2013]. For the TGFs to be measured they need to traverse the atmosphere in which Compton scatterin is happening. Due to this scattering effect the spectrum is slightly soften and the arrival times are delayed [Dwyer et al., 2012].
It has been established that TGFs are deeply correlated with lightning phenomena, as they generally coincide with the observable electrical activities associated with thunderstorms. Lyu et al. [2015] showed the strong correlation between Electric In-cloud Pulses (EIPs) and TGFs. Usually, TGFs manifest during the initiation phase of the lightning discharge, concurrently with the presence of robust electric fields at the tip of the lightning leader that are necessary for the acceleration of electrons to higher energies. These flashes are created during the upward negative breakdown phase that marks the start of intracloud lightning discharges [Hongbo et al., 2019b]. Furthermore, it has been observed that TGFs predominantly occur after the initiation of lightnings, specifically during the initial phase of positive intracloud lightning when a negative leader traverses the space between the main negative and positive region in a thundercloud [Dwyer and Uman, 2014, Skeie et al., 2022]. Very Low Frequency (VLF) radio atmospherics, commonly referred to as sferics, generated by lightnings, occur concurrently with TGFs within a temporal window of several hundred microseconds. This temporal association has been justified by measurements from both RHESSI and AGILE [Dwyer and Uman, 2014, Dwyer et al., 2017]. Ostgaard et al. [2008] concluded that the TGF-

associated radio signals are produced either by the hot-leader lightning channel or the TGF or a combination of the two [Paras and Pooja, 2021]. In general, there are three different types of interaction between sferics and TGF: simultaneous occurrence, a few milliseconds of temporal difference or when the radio signal is hundreds of milliseconds subsequent to the TGF. The radio signals that have been measured may originate directly from the runaway electrons and the associated currents generated by low-energy electrons and ions [Lindanger et al., 2022].
In conclusion, it is relevant to highlight the significant distinction between TGFs and other atmospheric phenomena related to lightning. TGFs are fundamentally shorter in duration compared to gamma ray glows, which can persist for several minutes. Despite their common origin, TGFs are differentiated by their duration, luminosity and temporal alignment concerning lightning discharges. This similarly applies also to the relation with Blue Jets and Gigantic Jets, as these phenomena occur over a significantly longer period of time compared to TGFs. While TGFs duration is in the range of milliseconds the duration of Jets exceeds to up to a few tens of milliseconds [Dwyer and Uman, 2014, Surkov and Hayakawa, 2012a].

3.3.2 Relativistic Runaway Electron Avalanche

The leading central approach for describing and explaining high energy atmospheric phenomena, especially TGFs, is the so-called RREA model, schematically shown in Fig. 3.13. Even though this model is widely spread and accepted, there are still several aspects which cannot be explained. For instance the highest achievable energies of up to 100 MeV which translate into the maximum voltage drop that can be established in the thunderclouds [Marisaldi et al., 2013]. Also, the connection with lightnings and cloud microphysics or the overall occurrence of TGFs are a topic of current research [Dwyer and Uman, 2014, Marisaldi et al., 2013].
The main idea of runaway electrons was already introduced by Fishman et al. [1994]. Gurevich et al. [1992] expanded this concept by showing that after including Møller scattering, the runaway electrons undergo an avalanche multiplication. Møller scattering describes the scattering of high-energy electrons with atomic electrons which leads to the multiplication effect. So, RREA in general is described as an avalanche of electrons with relativistic runaway energies which increase exponentially with time and distance [Marisaldi et al., 2013, Dwyer and Uman, 2014].
In order to create RREAs some of the scattered atomic electrons need to have energies

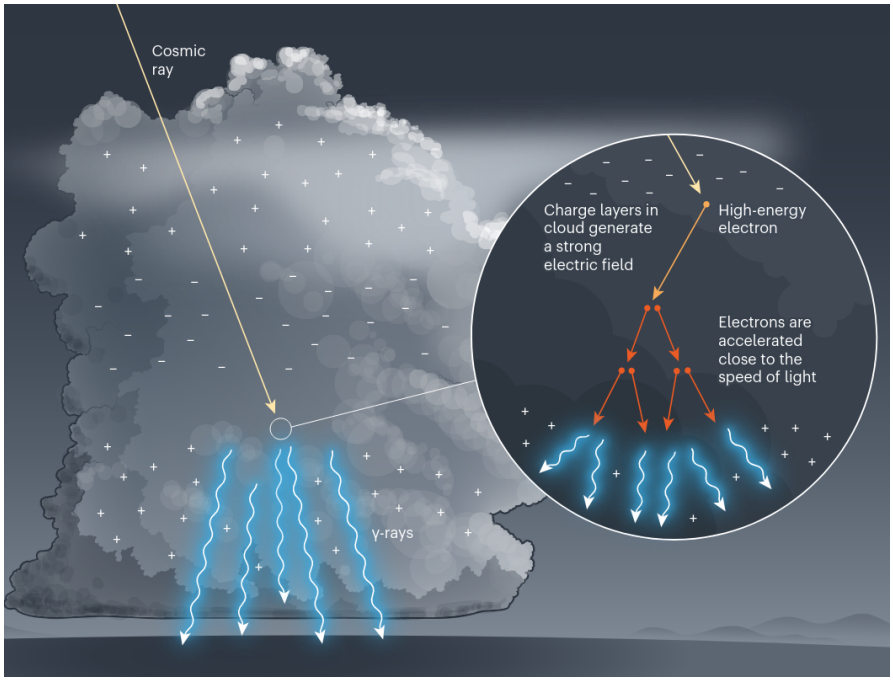

Fig. 3.13: Sketch of the RREA model. Taken from [Gibney, 2021]

E above a threshold energy so that they also become runaway electrons which run away with the initial electrons whereby the avalanche gets strengthened. The threshold field to create the necessary energies was found to be

$$E_{\mathrm{th}} = 2.84 \times 10^5 \, \frac{\mathrm{V}}{\mathrm{m}} \times \frac{\mathrm{n}}{\mathrm{n_0}} \tag{3.14}$$

where n is the density of air and n_0 is the density of air at STP [Dwyer, 2003, 2008]. While the previously introduced electric field E_{k} describes the field where a plasma channel is created, the field E_{th} relates to the acceleration of electrons. Electric fields of this magnitude were already measured and proven to exist inside of thunderclouds [Abbasi et al., 2019]. E_{th} is slightly larger than the break-even field, describing the minimum value of the ionization energy loss curve [Marisaldi et al., 2013]. Although the RREA mechanism is frequently referred to as *runaway breakdown*, it is not a true electrical discharge since it typically relies on an external source for it to happen. This could be high-energetic natural radioactivity, cosmic rays and/or solar particle events (SPEs) [Dwyer, 2008]. This mechanism can become self-contained in the extreme electric fields near lightning leader tips. In these regions, thermal runaway processes accelerate the high-energy tail of the electron population into the runaway regime. This internal injeciton allows the RREA to proceed independently of external radiation [Marisaldi et al., 2013]. Because the RREA mechanism relies on external seed electrons to initiate

runaway avalanches, the resulting runaway flux is dependent on the flux of inital seed electrons. Consequently, while RREAs increase the total number of runaway electrons, this output remains linked to the availability of seed electrons. This relationship, where the RREA serves as a multiplier of the initial population, can be described by:

$$F_{\mathrm{RREA}} = F_{\mathrm{seed}} \exp\left(\int_0^L \frac{dz}{\lambda}\right) = F_{\mathrm{seed}} \exp\left(\frac{L}{\lambda}\right), \tag{3.15}$$

with L being the vertical acceleration length in z-direction, λ being the avalanche length which is the characteristic length scale and F_{seed} is the flux of initial seed electrons in electrons $\mathrm{cm}^{-2}\,\mathrm{s}^{-1}$ [Marisaldi et al., 2013, Wada et al., 2019a]. One can compare RREAs to low-energy electron avalanches, except the length scale λ for avalanche multiplication is different. This so-called e-folding length describes the distance at which the number of runaway electrons increased exponentially by a factor of e and can be described with

$$\lambda = \frac{7.3 \times 10^6 \mathrm{V}}{E - 2.76 \times 10^5 \frac{\mathrm{V}}{\mathrm{m}} \times \frac{\mathrm{n}}{\mathrm{n_0}}} \tag{3.16}$$

where 7.3 MeV is the average energy of runaway electrons which was estimated from Monte Carlo Simulations and is the elctric field in $\mathrm{V\,m}^{-1}$ [Dwyer, 2008, Dwyer and Uman, 2014]. While for low-energy electron avalanches with energies of a few eV, λ is in the range of sub-millimeters, for RREAs it is in the range of tens to hundreds of meters [Dwyer and Uman, 2014, Marisaldi et al., 2013].

RREA models of TGFs are tied to the source of the energetic seed electrons and produce a unique energy spectrum which is nearly independent of the surrounding conditions like gas density, electric field strength or the details of the seed population [Dwyer, 2008]. After a few avalanches this spectrum approaches a steady state configuration, so the overall shape of the spectrum does not change, even though the number of electrons is increasing. The reason for this is that the individual electrons gain energy on the one hand but on the other hand create new low-energy electrons through Møller scattering. This steady state runaway electron energy distribution becomes

$$f_{\mathrm{re}} = \frac{F_{\mathrm{RREA}}}{7.3\,\mathrm{MeV}} \exp\left(\frac{-\varepsilon}{7.3\,\mathrm{MeV}}\right) \tag{3.17}$$

where F_{RREA} is the given flux and ε is the kinetic electron energy [Skeltved et al., 2014].

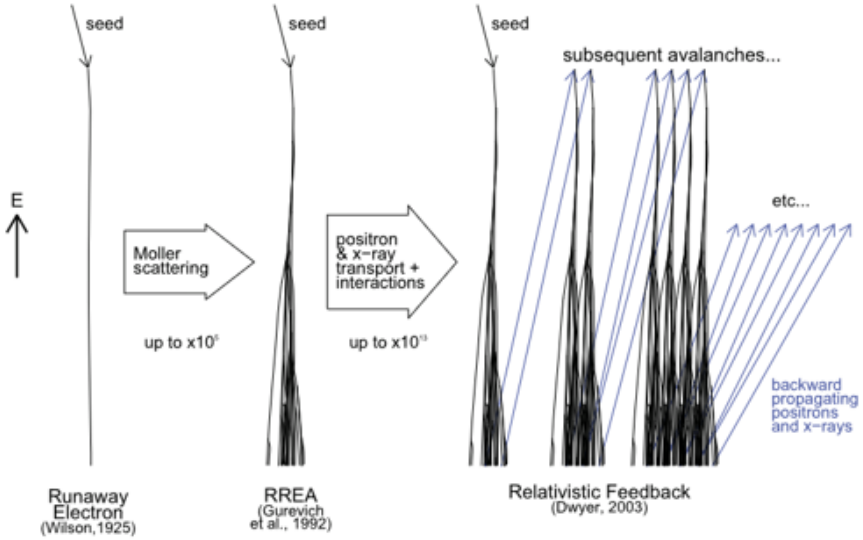

Fig. 3.14: Sketch of the RREA model with feedback mechanism. The origin is a high energy seed electron which travels down the thundercloud and creates more free electrons due to Møller scattering. This avalanche production is described by the RREA model. Reaching the end of the avalanche the electrons get scattered back to the beginning of the avalanche to create more subsequent avalanches there, increasing the flux and the number of free electrons over all. Taken from [Dwyer et al., 2012]

3.3.3 Feedback Mechanism

After describing the RREA model in Section 3.3.2 it is to mention that there are several challenges for explaining TGFs utilizing this model. Therefore, Dwyer [2003] proposed a new additional mechanism referred to as the relativistic feedback, aimed at addressing the limitations of the previous RREA model, which modifies the dynamic of runaway electron production [Dwyer and Uman, 2014]. This feedback mechanism, the so-called Relativistic Feedback Mechanism (RFM), builds upon the principles studied by Wilson [1925] who described the energy gain of electrons in an electric field. He proposes a positive feedback effect by incorporating the physics associated with backscattered γ-rays and positrons resulting from γ-ray pair production where both propagate to the initiation point of the avalanche region and generate new avalanches. Through this procedure an exponential growth in avalanches is created which is schematically shown in Fig. 3.14. The whole process is analogous to the Townsend discharge where positive ions and UV photons produced by the electrons in an avalanche may interact with atmospheric constituents, producing additional free electrons and consequently secondary avalanches [Kelley et al., 2015, Dwyer and Uman, 2014].

The RFM is predominantly comprised of two distinct processes. The first one is the positron feedback mechanism wherein runaway electrons emit bremsstrahlung X-rays that leads to pair production within the atmosphere. The resulting positrons are subsequently accelerated in the electric field, opposing the direction of the electrons. Upon reaching the start of the avalanche the positrons can generate additional runaway electrons through hard elastic scattering with atomic electrons present in the air (i.e. Bhabha scattering) whereby secondary avalanches are created as a result. This positron feedback is typically predominant for lower electric field strengths $E < 750\,\mathrm{kVm^{-1}}\times\mathrm{n}$ [Dwyer and Uman, 2014, Dwyer et al., 2012].
An alternative process is the γ-ray feedback wherein bremsstrahlung X-rays or γ-rays undergo Compton backscattering. When these backscattered photons reach the start of the avalanche and generate runaway electrons through Compton scattering or photoabsorbtion, a secondary avalanche is created. This feedback mechanism prevails for higher electric field strengths $E > 750\,\mathrm{kV}m^{-1} \times n_{\mathrm{air}}$ where n_{text} is the density of air relative to that at sea-level at standard conditions, as it requires shorter avalanche lengths in comparison to the the positron feedback. This is due to the fact that the photons created through Compton scattering have a shorter attenuation length relative to runaway positrons. While the positrons are able to travel in the range of a kilometer on sea-level, photons have a range of a few hundred meters [Dwyer and Uman, 2014].
A very important factor or property for describing the RFM is the so-called feedback factor γ which describes the relation between the amount of runaway electrons compared to the amount of runaway electrons in the previous cycle. If this feedback factor exceeds the value 1 the whole discharge process is called self-sustaining and independent of the amount of seed particles. Once the relativistic feedback becomes self-sustaining, this state is referred to as relativistic breakdown. Unlike the runaway breakdown from Section 3.3.2 the relativistic breakdown produced by the RFM is a true electrical breakdown since the discharge is self-sustaining and results in a collapse of the electric field. With this breakdown happening, the large-scale electric field will be discharged in less than a millisecond and moreover the resulting flux of runaway electrons is up to 10^{13} times larger than from the RREA mechanism alone [Dwyer and Uman, 2014, Dwyer, 2008]. So, including the relativistic feedback mechanism is one approach to explain the high fluxes and short durations of TGFs.
The relativistic feedback limits the RREA multiplication factor to below $\gamma < 10^5$ which is a reasonable factor for thundercloud fields [Dwyer et al., 2012]. TGFs can consist of either a single pulse or multiple pulses. These multiple pulse signals can also be generated by the relativistic feedback streamers. This pulsing behavior is due to the interplay of low-energy electron and ion currents which impact the electric field in the

avalanche area. Specifically, when the flux of runaway electrons becomes too large due to the feedback mechanism, the feedback factor γ is decreased because of the discharge at the end over the avalanche by low-energy electrons. This then terminates the runaway electrons and hence the gamma-ray pulse. After the pulse the current in the region behind the avalanche region is increased over a few milliseconds which then puts the feedback factor γ again > 1 [Dwyer and Uman, 2014].

3.3.4 Previous Measurements

This section summarizes key quantitative and observational results from both space-born instruments and ground-based experiments investigating TGFs. These measurements provide crucial constraints on theoretical production models, in particular the RREA mechanism and its extension through relativistic feedback, which together form the foundation of current TGF theory. TGFs have been extensively studied through observations from space-based instruments such as BATSE, RHESSI, AGILE, Fermi GBM, and ASIM and, more recently, from ground-based facilities [Marisaldi et al., 2013, Dwyer et al., 2017, Collier et al., 2011, Chaffin et al., 2024]. These measurements have provided critical constraints on the intrinsic physical properties of TGF sources, including their altitude, energy spectrum, duration, and fluence.

A central aspect of TGF research is the determination of the source altitude, as both the particle acceleration process and the resulting photon spectrum strongly depend on the atmospheric density at the emission site. Systematic analyses combining Monte Carlo simulations with spectral observations have since placed strong constraints on the source location. Comparisons between simulated bremsstrahlung spectra and RHESSI observations indicate that upward-directed TGFs originate predominantly in the troposphere and lower stratosphere, at altitudes between approximately 15 km and 21 km above sea level [Paras and Pooja, 2021, Collier et al., 2011, Dwyer and Smith, 2005]. Source altitudes exceeding 24 km are generally incompatible with the observed spectral hardness due to excessive atmospheric attenuation [Gjesteland et al., 2011, Carlson et al., 2012]. Measured RHESSI spectra are illustrated in Fig. 3.15.

In addition to space-based observations of upward-directed TGFs, ground-based experiments have provided important insights into downward-directed events, which imply significantly lower source altitudes. Measurements during winter thunderstorms by Wada et al. [2019b] revealed downward TGFs consistent with source altitudes of $2500 \pm 500\,\mathrm{m}$, as constrained by Monte Carlo simulations and ionization chamber data.

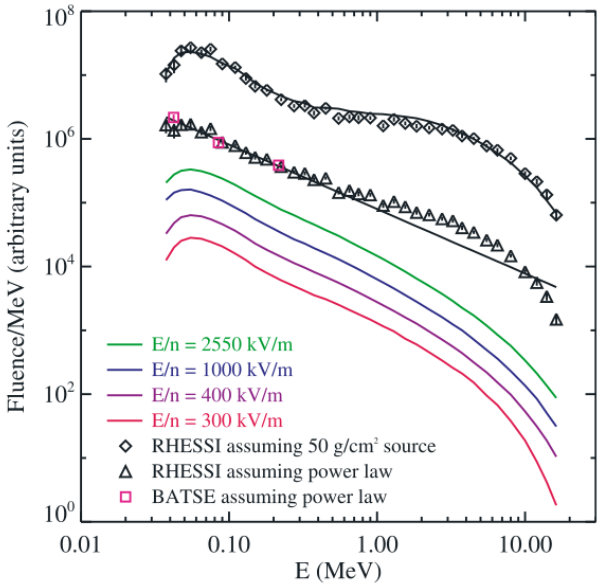

(a)

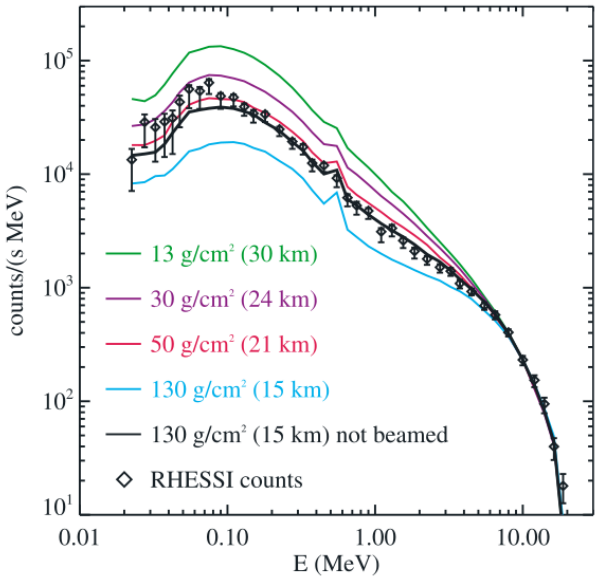

(b)

Fig. 3.15: (a) TGF photon spectra measured by RHESSI and BATSE, showing the characteristic hard spectrum extending up to tens of MeV. The lower four coloured curves show the X-ray emission spectra calculated by the Monte Carlo simulation for different values of the electric field in the avalanche region. The black solid curve was corrected for the instrumental response with the source asusmed to be located at an atmospheric depth of 50 gcm^{-2}. This corresponds to an altitude of 21 km. The bottom RHESSI data was corrected for the instrumental response assuming a E^{-1} powerlaw. (b) TGF count spectra measured by RHESSI as well as the X-ray emission spectra which are corected for the instrumental response. The spectra were simulated using Monte Carlo simulations with a runaway breakdown field of E = 400 kVm^{-1} and four atmospheric depths. The spectra are normalized to the 10 MeV RHESSI point. Taken from [Paras and Pooja, 2021].

Such low altitudes are characteristic of the charge structure of winter thunderclouds. While no direct TGF measurements have yet been reported from the Zugspitze research station, extensive modeling has been performed for comparable high-altitude experiments, such as the Gamma-Flash experiment at Mt. Cimone (2165 m a.s.l.) [Ursi, 2021]. These studies define a 'detectability region' within which TGFs can survive atmospheric attenuation and be detected at ground level. For a typical TGF emitting $\approx 10^{18}$ photons within a 40° half-angle, visualized in Fig. 3.16, this region extends up to approximately 4 km in horizontal distance and up to 10 km in altitude above sea level. The shape of this region is governed by the atmospheric mass content, which decreases exponentially with altitude. Ursi [2021] used GEANT4 simulations to model the propagaiton of the γ-rays through the atmosphere and employed a cutoff powerlaw at 6.6 MeV as the source energy spectrum. The researchers determined that the detectability region experiences significant lightning activity with an estimated 60 – 730 lightning flashes per year in their investigable area.

TGF energy spectra are notably hard, with a power-law index around -1, placing

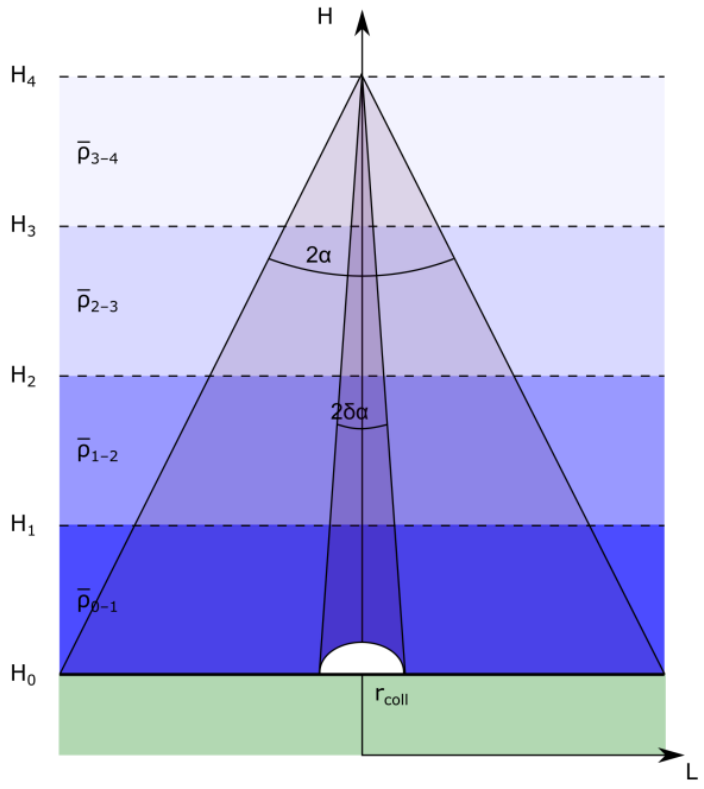

Fig. 3.16: Schematic (L,H) diagram of a TGF emission with half-angle α. Radiation emitted from a source at altitude z crosses different atmispheric layers at altitudes H with different average densities $\bar{\rho}$(H). r_{coll} describes the radius of the dome which is housing the γ-ray detector. Taken from [Ursi, 2021].

strong constraints on the underlying acceleration mechanisms, most probably being bremsstrahlung. Photon energies typically extend up to 20 MeV, with several measurements reporting energies reaching 40 MeV. Early AGILE observations even suggested spectral components approaching 100 MeV. However, subsequent studies demonstrated that these high-energy features can be reconciled with standard RREA-based spectra when instrumental effects such as dead time and pulse pileup under high-flux conditions are properly modeled [Marisaldi et al., 2019]. Overall, the intrinsic source spectrum is well described by bremsstrahlung emission from RREAs, typically modeled as a power law with an exponential cutoff, with a characteristic e-folding energy of approximately 7.3 MeV. This e-folding energy represents the energy interval over which the spectral flux decreases by a factor of e within the exponential tail. [Paras and Pooja, 2021].
The observed TGF photon spectrum can be described by a power law with an exponential cutoff, expressed as

$$\frac{dN}{dE} = K \left(\frac{E}{E_{\text{piv}}} \right)^{-1} \exp \left(-\frac{E}{E_{\text{cutoff}}} \right), \tag{3.18}$$

where K is the normlaization constant, E_{piv} is the pivot energy and E_{cutoff} describes the cutoff energy. The observed photon spectrum is strongly influenced by atmospheric propagation effects and the angular distribution of the emission. TGFs are inherently anisotropic, emitting radiation into a relatively narrow cone aligned with the local electric field while the width of this emission cone is related to the geometry and electric field of the source region. Spectral softening is observed at large viewing angles ($\geq 40°$) due to enhanced Compton scattering which provides an important constraint on the beam geometry. These measurements indicate typical emission half-angles in the range of $30° < \alpha < 40°$, consistent with production in a vertical or near-vertical electric field [Gjesteland et al., 2011].
Temporal measurements provide valuable insights into the involved discharge processes. Observed durations are mostly in the sub-millisecond range, with T_{50} values (containing the central 50% of counts) ranging from 20 μs to 1 ms[Dwyer et al., 2017]. Ground-based observations of downward TGFs reveal even finer temporal structure, consisting of multiple discrete pulses with individual durations of $\leq$ 10 μs spread over several hundred microseconds, originating at altitudes of a few kilometers above ground level [Abbasi et al., 2019]. It has been suggested that the smoother and longer-duration pulses observed from space result from atmospheric scattering processes, particularly Compton scattering, which temporally broaden and merge these short emission components. A measurement of multiple TGF pulses is shown in Fig. 3.17.

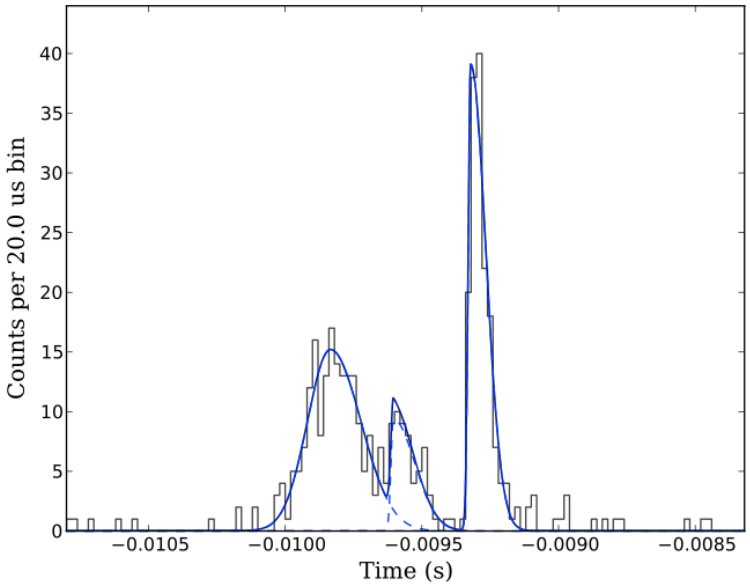

Fig. 3.17: Lightcurve measurement of GBM TGF110828435. The dotted lines show the fits of the single pulses. The overlapping of several pulses is visible. Taken from [Foley et al., 2014].

Beyond spectral and temporal properties, the observed intensity of TGFs provides one of the strongest constraints on their production mechanisms. To create these intensities, the production of 10^{16} to 10^{17} runaway electrons with energies exceeding 1 MeV is necessary, depending on the source altitude [Dwyer, 2008]. Ground-based measurements of downward TGFs for energies >1 MeV suggest even larger particle numbers, with estimated avalanche electron counts of $8^{+8}_{-4} \times 10^{18}$ for source altitudes near 2.5 km [Wada et al., 2019b]. These large particle numbers indicate that the basic RREA process must be significantly amplified, often requiring the inclusion of the relativistic feedback mechanism. Wada et al. [2019b] performed measurements using BGO crystal scintillators and ionization chambers to measure the TGF and the correlated total radiation dose. They also performed Monte Carlo simulations employing GEANT4 to translate the dose measurements into physical parameters. Key findings were a TGF duration of less than 1 ms with a separation time of about 0.7 – 1.5 ms. They confirmed that the TGFs were intense enough to trigger photonuclear reactions in the atmosphere, which was evidenced by a sub-second decay of γ-rays from neutron capture and a 10 s afterglow from positron annihilation.

TGFs exhibit a strong temporal and spatial correlation with lightning activity. Cross-correlation studies using RHESSI and the World Wide Lightning Location Network (WWLLN) show that TGFs typically precede the associated lightning discharge by approximately 0.77 ms, suggesting that γ-ray emission occurs during the initial stages of

lightning development rather than during the return stroke [Collier et al., 2011, Chaffin et al., 2024]. TGFs are usually associated with IC lightnings while a subset of TGFs is correlated with a distinct radio signature where the temporal shape of the signal matches the duration of the TGF. These include slow pulses, whose microsecond-scale durations closely match those of TGFs. They are commonly interpreted as the output of the RREA process itself, as well as EIPs, which are characterized by exceptionally high peak currents. EIPs associated with TGFs have been observed with peak currents exceeding 200 kA, particularly during the negative leader stage of positive intra-cloud lightning [Dwyer et al., 2017, Hongbo et al., 2019a].

3.4 Background Radiation And Disturbances

This section provides an overview of the various sources of background radiation and disturbances that can impact the detection and analysis of TGFs. Understanding these sources is crucial for accurately interpreting TGF measurements and distinguishing genuine TGF signals from background noise. The main sources of background radiation include natural radioactivity, cosmic rays, and SPEs. Each of these sources contributes to the overall radiation environment in which TGFs are observed and can influence the detectability of TGFs measured at high altitudes or in space.

3.4.1 Natural Radioactivity

Natural radioactivity is an omnipresent process on Earth and has to be taken into account when observing TGFs. There are two main sources of natural radioactivity, namely terrestrial radioactivity and cosmogenic radioactivity. The majority of the measurable radioactivity originates from the terrestrial radionuclides, which naturally occur in the ground and stones so they are abundant in Earth's crust and mantle. There are two possibilities for the origin of natural radionuclides: either they have a half-life time comparable to the Earth's age or they are continuously created. The members of the former case are called *primordial radionuclides* with typical representants being uranium (^{238}U, ^{235}U), thorium (^{232}Th), and potassium (^{40}K). The γ-ray spectra of these isotopes are shown in Fig. 3.18. The radioactive decay of these isotopes is the reason for approximately half of the Earth's internal heat balance. When working

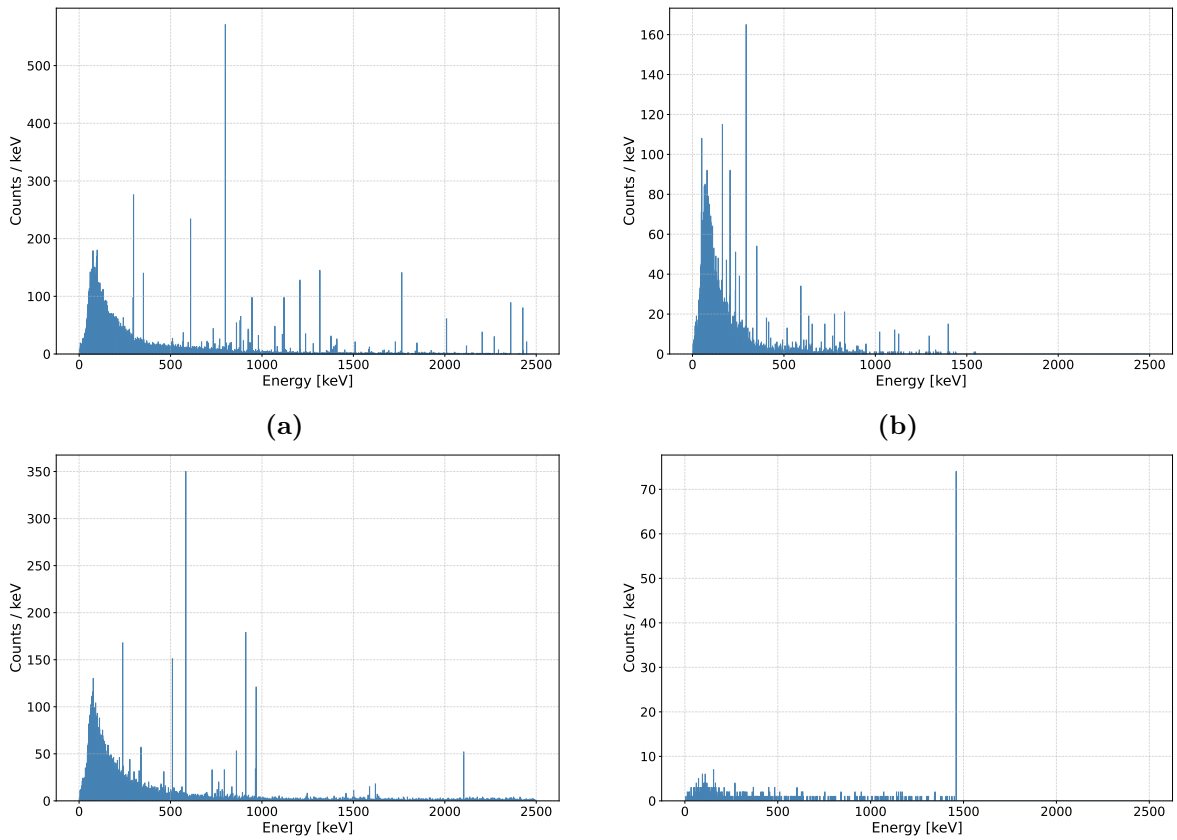

Fig. 3.18: γ-ray lines for the four isotopes: (a) ^{238}U, (b) ^{235}U, (c) ^{232}Th, and (d) ^{40}K. The spectra for the isotopes were obtained by performing simulations with the geometrical model used in this work. The shown γ-ray peak conicide with literaure values found at [Gamma-ray spectra].

with Naturally Occuring Radioactive Material (NORM) one is primarily interested in the primordial radionuclides as well as in the resulting decay products. These are of primary interest because their high geological half-lives ensure a universal presence in the Earth's crust, serving as the constant source for long decay chains that produce radiologically significant daughter isotopes. [Romano et al., 2021, Kovler et al., 2017]. When radionuclides decay there are three main modes as shown in Fig. 3.19: α-decay, β-decay and γ-deexcitation. α-radiation consists of a ^{4}He nucleus with 2 protons and 2 neutrons. This composition gives it a high mass compared to the products of other decay processes. Its ionizing effect is very high, so as a consequence the penetrating power is low, making it unable to penetrate a piece of paper. β-radiation on the other hand is composed of high energy electrons (β^-) or positrons (β^+). 'During a β^--decay the radionuclide transforms a neutron into a proton while emitting a high energy electron, while in a β^+-decay the radionuclide transforms a proton to a neutron while emitting

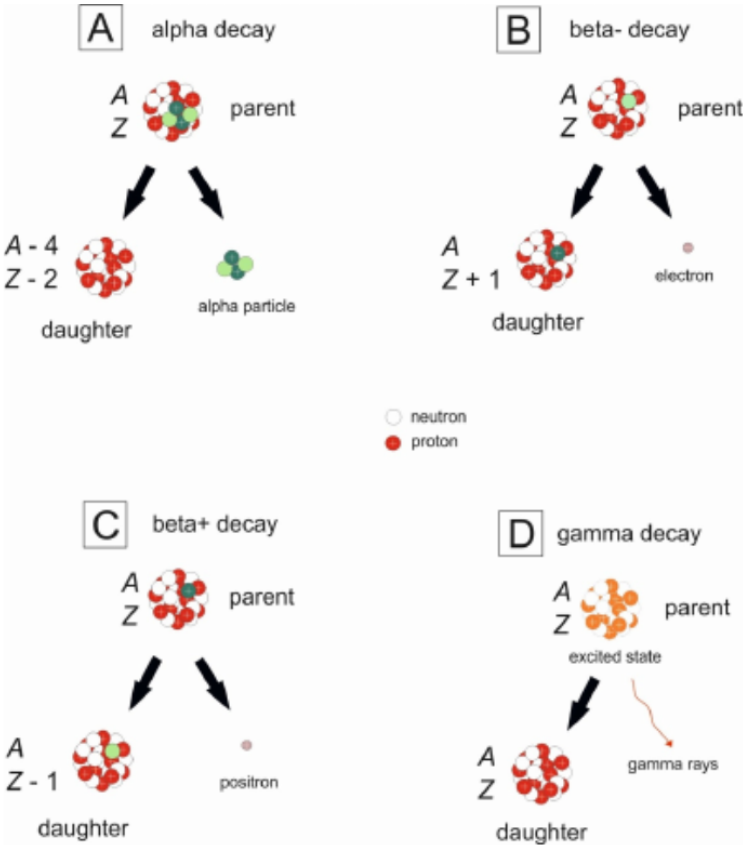

Fig. 3.19: A 'parent' nuclide decays into a 'daughter' nuclide by emitting particles and energy. The main types of decay are: (a) α-decay: a radionuclide emits an α-particle which is a He core composed of 2 neutrons and 2 protons while the resulting nuclide is reduced by these four nucleons; (b) β^--decay: a neutron is transformed into a proton while a high-energy electron is emitted; (c) β^+-decay: a proton is transformed into a a neutron while a positron is emitted; (d) γ-deccay: a radionuclide in an excited state reaches a lower energy state by emitting γ-rays. Taken from [Romano et al., 2021].

a high energy positron.' The ionizing effect is lower compared to α-radiation which results in a higher penetration power. γ-radiation consist of high-energy photons which is released when the radionuclid makes a transition from an excited state to a state of lower energy. Because photons have no mass and charge, they interact less frequently with matter compared to charged particles. This results in a lower ionization density of γ-radiation, making the penetration power high [Romano et al., 2021].

3.4.2 Cosmic Rays and Solar Particle Events

Cosmic rays are a second source of natural radioactivity and can function as the origin or seed of TGFs as mentioned in Section 3.3.2. They can be divided in two components: *galactic cosmic rays* (GCR) and *solar cosmic rays* (SCR) which are created during SPEs.
GCRs are produced and accelerated in general as a consequence of stellar flares, supernova explosions or as a side product of pulsar acceleration or outbursts of active galactic nuclei. They are composed mainly of protons ($\sim 95\%$) and α-particles ($\sim 3.5\%$) while the rest are heavy nuclei with atomic numbers $3 < Z < 90$ [Bell, 2013, O'Brien et al., 1996]. It is to mention that electrons and photons are emitted by GCRs but their contribution at the terrestrial radiation dose is negligible. The energy distribution of cosmic rays follows approximately $E^{-\gamma}$ with $\gamma =\sim 2.6$. Above energies of 1 PeV the spectrum steepens to $\gamma =\sim 3$ [Bell, 2013, O'Brien et al., 1996].
When the GCRs travel through the solar system *solar modulation* can happen because the solar system is filled with an expanding completely ionized plasma (the solar wind) which contains frozen-in irregular magnetic fields. By scattering at these irregularities the cosmic radiation loses energy. Since this is a result of the solar flares or Coronal Mass Ejections (CMEs) , the flux as well as the composition of the cosmic rays hitting the Earths atmosphere and in general the frequency of appearing SPEs varies with the 11-year solar cycle – with increasing solar activity the intensity of GRCs is decreasing [O'Brien et al., 1996].
As soon as the GRCs interact with the atmosphere, secondary particles are created so the cosmic radiation field near the ground consists almost exclusively of secondary particles, namely muons and neutrons. Also, the interaction of GCRs with the atmosphere creates cascades of secondary particles and cosmic radionuclides like Carbon (^{14}C), Tritium (^{3}H), Sodium (^{22}Na), and Beryllium (^{10}Be) [Masarik, 2009]. This interaction starts right at the top of the atmosphere, reaching a maximum at an atmospheric depth of $100 - 200\,\mathrm{g\,cm^{-2}}$ and the energy spectra of these interactions reach up to several hundreds of GeV [O'Brien et al., 1996]. Expressed as mass thickness, this unit represents the integrated columnar density along the particle's path, effectively normalizing the variable atmospheric density. This allows for a consistent description of the depth at which the primary flux has undergone sufficient collisions to maximize secondary particle production.
While cosmic rays have their origin outside of the solar system, SPEs are created inside of the Sun since they are high energy particles created through solar flares or CMEs.

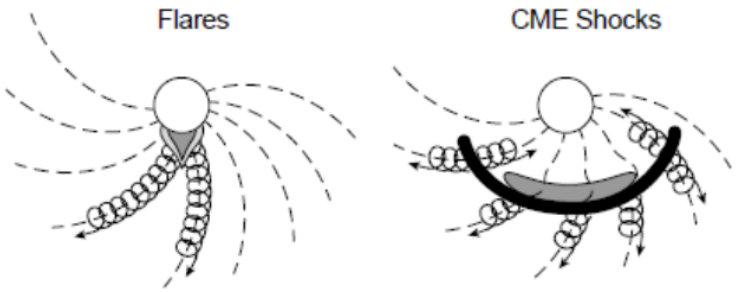

Fig. 3.20: Two types of SPEs: impulsive events (left) and gradual events (right). Impulsive events are produced by solar flares, populating the interplanetary magnetic field lines connected to the flare site. The gradual events are produced by large-scale CME driven shock waves which accelerate particles and populate interplanetary magnetic field lines over a large longitudinal area. Taken from [Hu, 2017].

There are mainly two types of SPEs: impulsive and gradual events, which is illustrated in Fig. 3.20. Impulsive events are directly connected to solar flares. These are energetic explosions at the surface of the Sun, occuring when built up magnetic energy in the solar atmosphere is suddenly released. The events produced here create a stream of high energy particles which are oriented along the magnetic field lines of the flare. CMEs are the drivers of gradual events. These involve large eruptions of the corona at a location up to several solar radii away from the Sun. The events produced there involve energetic particles which interact with collisionless shock waves so they are propagating in every direction, populating magnetic field lines over a broad range of longitudes [Hu, 2017].

3.4.3 Radiation Background in Alpine Environments

The detector setup takes place in the German-Austrian alps so it is quite important to take into account the radiation we measure there as a background. Therefore we need to keep in mind that as well as the cosmic radiation changes with altitude and latitude the NORM also changes with rock formation and soil composition. As mentioned in Section 3.4.1, the most common occuring natural radiation materials are Uranium, Thorium and Potassium. Since the dose of ^{235}U is 20 times less than the dose of ^{238}U the main focus is on the ^{238}U, ^{232}Th and ^{40}K series. The decay chains of ^{238}U, ^{235}U, ^{232}Th, and ^{40}K are visualized in Fig. 3.21 [Romano et al., 2021, Kovler et al., 2017].

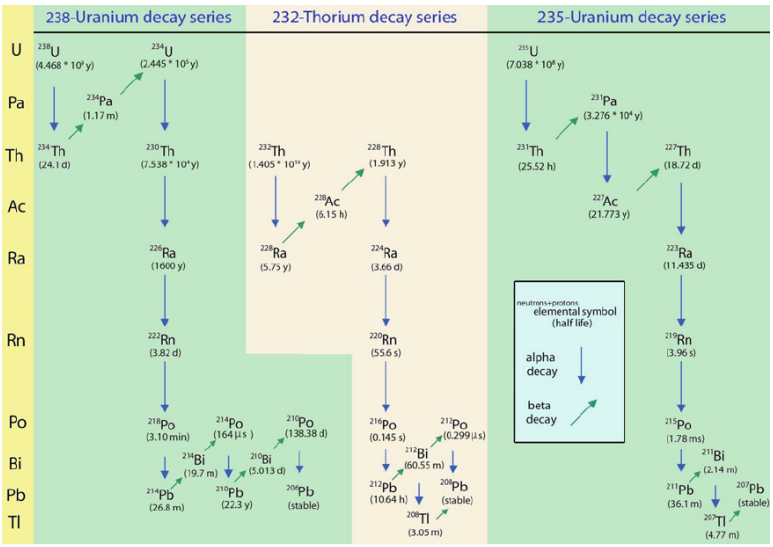

(a)

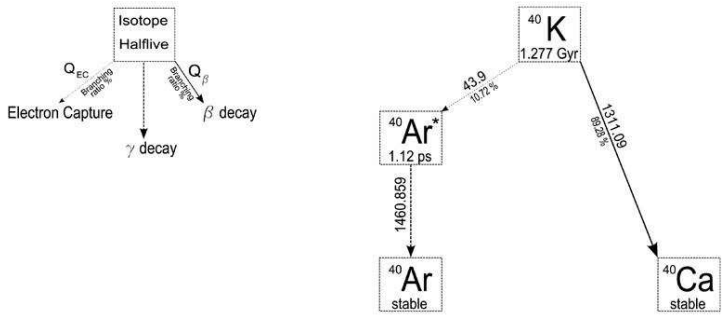

(b)

Fig. 3.21: (a) Decay chains of: ^{238}U, ^{235}U, and ^{232}Th. (b) Decay scheme of ^{40}K. Taken from [Porcelli and Baskaran, 2020, Fiorentini et al., 2007].

4 Measurement Site and Detector System

The experimental setup and its environment are decribed in this chapter. Since the measurement site can influence the detection of TGFs it is explained in detail here.

4.1 Zugspitze Research Station UFS

The UFS is located near the summit of the Zugspitze mountain, on the German-Austrian border, at 47° 24' 59.8" N longitude (lon) and 10° 58' 46.5" E latitude (lat). The station consists of three measurement platforms, all constructed from concrete. While some laboratories are located inside the building, most scientific instruments are installed outside to allow for the direct observation of atmospheric and environmental conditions at high altitude. The UFS and its location are shown in Fig. 4.1. The UFS is operated by a consortium of various partners, including research institutes such as the 'Deutsche Zentrum für Luft- und Raumfahrt' (DLR) as well as universities like the Technische Universität München (TUM) and the Julius-Maximilians-Universität Würzburg (JMU). As a result, a wide range of scientific experiments are conducted at the station. The main research areas include cloud dynamics and atmospheric processes, cosmic rays and radioactivity, hydrology, and satellite-based Earth observations [Schneefernerhaus, 2025].

There are several compelling reasons to conduct TGF measurements at the UFS. Firstly, its high-altitude location near the summit of the Zugspitze significantly reduces the atmospheric attenuation of γ-rays, increasing the likelihood of detecting TGFs from closeby thunderstorms. Additionally, the alpine region is regularly affected by thunderstorms, providing frequent opportunities for TGF-related observations. The UFS

Fig. 4.1: The UFS located at the mountainside of the German-Austrian alps. It consists of several measurement platforms concisting of concrete. Several institutes collaborate to this research station.

is also equipped with extensive scientific infrastructure, including power supply, data acquisition systems, and meteorological instrumentation. This existing setup greatly facilitates the implementation of a TGF experiment, reducing the effort and complexity compared to deploying a similar system at a remote or undeveloped location.
The *Kugelalm* shown in Fig. 4.2 is the hut where the scintillation detector for performing the measurements will be placed, located at 2657 m altitude on the lowest one of the concrete measurement platforms. It is of triangular shape and its roof consists of a wooden and an aluminum layer. This is to protect the inside from snow, wind and cold temperatures and moreover, it is heated to 15°C during winter. It houses several detectors and electric equipment to measure γ-rays and SPEs, among others.

Fig. 4.2: The Kugelalm houses several scientific instruments. The detector used in the simulations is located inside the Kugelalm, shielding it from the weather.

4.2 Detectors and Detection Principle

The detection principle for the type of detector used in this work is described in this chapter. It is further explained how imaging and spectral response of this detector type works.

4.2.1 Concept of Detector Response

To investigate incoming γ-rays, the application of scintillation detectors such as NaI(Tl) is extensively utilized. The concept of the γ-ray detection process is illustrated in Fig. 4.3. It starts with the penetration of particles or γ-rays into the scintillation crystal. It is important to mention that this process is stochastic, meaning that not every photon of the same energy creates the same pulse which leads to an energy resolution. The atoms and molecules interact with the incoming photons, resulting in the excitation and ionization of them. These excited atoms and molecules return to their ground state by emitting a photon characterized by a specific energy. This emitted photon then traverses to the photo cathode of the detector whereby photo electrons are emitted. By integrating a Photo-Multiplier Tube (PMT), the amount of photoelectrons can be multiplied to generate a voltage pulse at the anode. This pulse can then be be subjected to analysis and recording. By measuring the energy of the emitted photons and their corresponding secondary particles, one can infer properties related to the initial input.

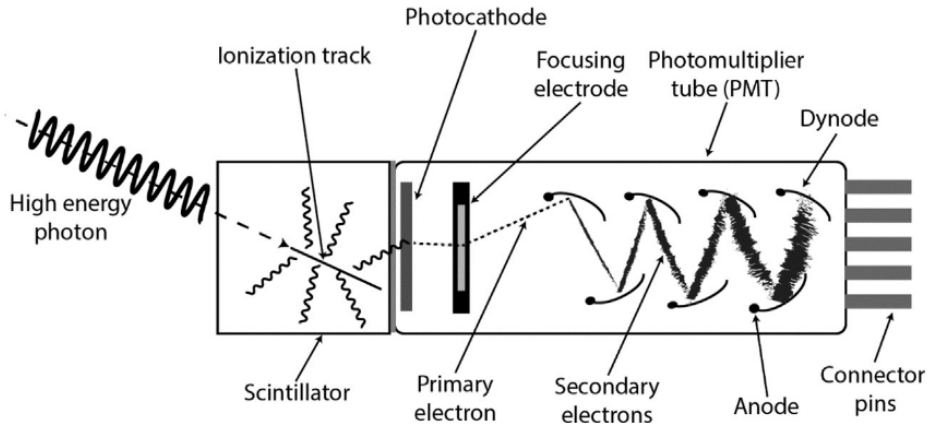

Fig. 4.3: Sketch of a scintillation detector

Imaging Response

An imaging response characterizes the systems ability to detect radiation as a function of its incoming direction. For the case used in this thesis this response is anisotropic due to the fact that the utilized detector is cylindrical and this detector is placed at the Kugelalm which is of triangular shape.
The primary metric for the imaging response is the effective area $A_{\text{eff}}(\theta, \varphi)$, representing the product of the geometric cross-section with the detector efficiency. Since the detector is located inside the UFS infrastructure the reponse needs to account for the shielding effects of the Kugelalm roof and the surrounding mountainside topography.
To quantify this, the imaging response is determined through Monte Carlo simulations. By simulating either a single far-field source with varying energy or multiple far-field sources distributed across the entire upper hemisphere, a response model is generated that accounts for both the intrinsic angular dependence of the scintillator and the extrinsic shielding caused by the local horizon and structural materials. These simualtions are carried out as described in Section 6.4, where the procedure is described in more detail.

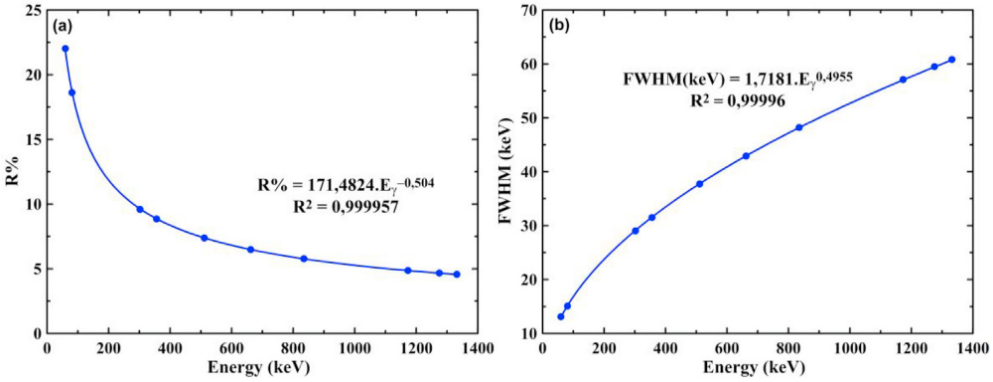

Fig. 4.4: Curve of the energy resolution (a) and the FWHM (b) as a function of the input energy of a NaI detector. Taken from [Demir and Kuluöztürk, 2021].

Spectral Response

The spectral response describes the transformation of the incident photon energy into a measured energy distribution. This process is characterized by the detector's energy resolution and its specific interaction probabilities. Due to the statistical fluctuation in the scintillation process and the subsequent electron multiplication within the PMT, monochromatic radiation results in a Gaussian-shaped distribution rather than a discrete line. The energy resolution is typically defined by the Full Width at Half Maximum (FWHM) of the photopeak. Since NaI is a widely used reference material in scintillation measurements, Fig. 4.4 illustrates the typical energy resolution and FWHM for a NaI detctor with cylindrical shape.
Furthermore, the spectral response accounts for partial energy depositions. While the photopeak represents the full absorption of a photon, the Compton continuum arises from photons that scatter within the crystal and subsequently escape. In the context of the UFS research station, the spectral response is also affected by spectral softening caused by the surrounding structure and the atmosphere. Photons may undergo Compton scattering in the roof of the detector housing before reaching the active volume of the NaI crystal, shifting the detected energies to lower values. This is detailed out further in Section 6.4.

5 Simulation and Modeling Framework

This chapter introduces the simulation framework used to model the detector response and the TGF detection probability at the UFS. It outlines the strategy and goals of the simulations, followed by an introduction to MEGAlib, the primary software utilized for conducting the simulations.

5.1 Strategy and Goals of the Simulation

The goal of the simulations and this thesis is to be able to achieve an estimate on the detection probability of TGFs with different detectors inside the Kugelalm at the UFS. To do so, idealized and literature based assumptions are used. This work wants to find out which detector performs best and how many TGFs can be detected with it.

5.2 Introduction to MEGAlib

All of the simulations are performed utilizing the same framewok, which is explained in detail in this chapter. The different components as well as the machine behind this framework are described.

5.2.1 Components and Tools

The main machinery at which the whole simulation procedure is based on is called MEGAlib (**M**edium-**E**nergy **G**amma-ray **A**stronomy **lib**rary), which is a C++ library and consists of a set of programs, used for gamma-ray instrumentation [Zoglauer, 2006a]. The main focus of MEGAlib is on making the whole path from simulations and measurements to high-level data analysis as easy as possible. MEGAlib is based on GEANT4 which is the general-purpose Monte Carlo simulator for everything. To effectively carry out simulations, MEGAlib is equipped with a variety of tools, each strictly designed to address a specific task within the broader simulation process [Zoglauer, 2006a].
The initial tool that must be employed is called *Geomega* (**Geo**metry for **MEGA**lib) which is the universal geometry and detector description library and has the purpose of building a mass model of the geometry to be simulated. To do so, Geomega uses different file types: for building the central input volume (.geo.setup), for defining subvolumes (.geo) and for describing detector characteristics (.det). Geomega is able to create, place and define specific volumes to build a whole setup as accurate as possible. Therefore, it is possible to choose between different shapes and materials and give certain properties to these volumes. A necessary step in Geomega is to define the detecting volume. By doing this, one is able to define distinct energy resolutions or trigger thresholds which might affect the resulting simulations. At the end Geomega works like the following: The basis of the geometry is a so called *WorldVolume* - all of the volumes a setup is built of are placed inside such an empty WorldVolume. This WorldVolume also contains a *Surrounding Sphere*, which is essential for the simulation part since it defines the starting point and direction of the simulated particles. As soon as this procedure is done, the simulated particles are started from a plane tangential to the surrounding sphere, as seen in Fig. 5.1. When the 3D geometry is set up, the next tool to use is *Cosima* (**Co**smic **Si**mulation of **M**eg**A**lib) [Zoglauer, 2006a].
Cosima is essentially simulating particles passing through the geometry defined in Geomega and generates Monte Carlo simulations. It is a framework built for carrying out the actual simulation. This is done through an ASCII input file - called 'source file' (.source) - which is then passed to Cosima. The source file contains all of the necessary simulation properties and has five main sections. First of all there is the geometry section where the previously built geometry is included. Internally, the geometry is loaded by Cosima and the for the simulation necessary parts are translated into GEANT4 materials, volumes, placements and sensitive detectors [Zoglauer et al., 2009]. The physics section describes the required physics list which should be chosen depending on the

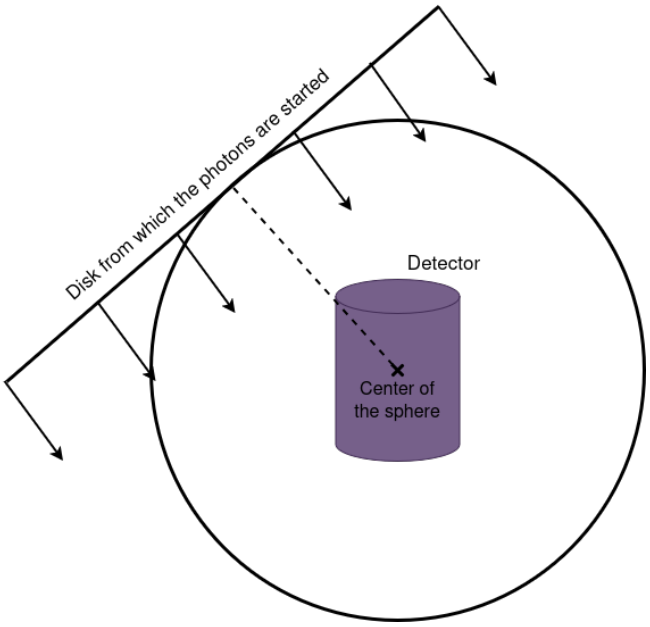

Fig. 5.1: Sketch of the surrounding sphere to visualize where the simulated photons are started. Inspired from Zoglauer [2006b]

given simulation situation since each option has different properties which are applied in each run. The following section is the output format. Here, information about the simulation output is adjusted i.e. if the simulation history is stored, if the entering and exiting particles are marked or how many significant digits are in the output file. After this the simulation run is specified with either one or multiple runs. A run is described by an output file name and a stop criterion like the running time or triggered events and one or more sources whereby the source itself has the physics of the simulated particles. Necessary attributes like the particle type, total flux, total energy or energy spectra like monoenergetic, linear, power law or more attributes are defined [Zoglauer et al., 2009]. The primary output of this process is the simulation file (.sim), a structured ASCII file that provides a multi-layered record of the detection process. Fig. 5.2 shows the structure of a .sim file. While the source file defines the 'intent' of the simulation, the .sim file documents the 'result' by categorizing data into three main sections: event metadata, physical interactions, and detector hits. The first layer contains global metadata for each simulated particle, such as the unique event ID, the absolute starting time, and the total energy deposited. Crucially for studies involving shielding or environmental structures, the header also tracks energy lost in non-sensitive volumes, labeled as passive material depositions. This allows for a quantitative assessment of how environmental components, such as a 'house' or detector housing, degrade the primary signal or attenuate the flux before it reaches the active detector volumes. The second layer consists of

```
# Simulation data file
# Created by Cosima and  Geant4 version Name: geant4-10-02-patch-03    (27-January-2017)

Type        SIM
Version     101
Geometry    /home/pehrmann/Pehrmann/RealisticModel/UFSMeasured.geo.setup

Date        2026-02-08 21:52:59
MEGAlib     4.00.00

Seed        6342542

SimulationStartAreaFarField 1.9635e+07
BeamType FarFieldPointSource 0 0
SpectralType PowerLaw 10 10000 1.0745

TB 0

SE
ID 1 20062
TI 0.000000010
ED 423.288
EC 0
NS 0
IA INIT  1; 0;0;0.000000000000e+00;1726.23916; 233.20144;2500.00000;0; 0.00000; 0.00000; 0.00000; 0.00000; 0.00000; 0.00000;     0.000;1;-0.00000;-0.00000;-1.00000; 0.00000; 0.00000; 0.00000;    423.288
IA ENTR  2; 1;4;7.571904960998e-08;1726.23916; 233.20144; 230.00000;1;-0.00000;-0.00000;-1.00000; 0.00000; 0.00000; 0.00000;   423.288;0; 0.00000; 0.00000; 0.00000; 0.00000; 0.00000; 0.00000;      0.000
IA COMP  3; 1;4;7.580249557218e-08;1726.23916; 233.20144; 227.49835;1; 0.79309;-0.39323;-0.46516; 0.00000; 0.00000; 0.00000;   314.551;3;-0.60506; 0.30000;-0.73750; 0.00000; 0.00000; 0.00000;    103.879
IA COMP  4; 1;4;7.580345319041e-08;1726.26193; 233.19015; 227.48500;1; 0.48360;-0.79425;-0.36783; 0.00000; 0.00000; 0.00000;   291.006;3; 0.68989; 0.67956;-0.24951; 0.00000; 0.00000; 0.00000;     23.508
IA COMP  5; 1;4;7.598899621221e-08;1728.95193; 228.77219; 225.43897;1; 0.52572;-0.39142;-0.75525; 0.00000; 0.00000; 0.00000;   272.683;3; 0.00190;-0.80070; 0.59906; 0.00000; 0.00000; 0.00000;     18.265
IA COMP  6; 1;4;7.606397280367e-08;1730.13362; 227.89239; 223.74135;1;-0.82905; 0.46003;-0.31789; 0.00000; 0.00000; 0.00000;   150.912;3; 0.76102;-0.49622;-0.41787; 0.00000; 0.00000; 0.00000;    116.914
IA RAYL  7; 1;4;7.607471762422e-08;1729.86657; 228.04057; 223.63895;1;-0.82436; 0.43864;-0.35780; 0.00000; 0.00000; 0.00000;   150.912;0; 0.00000; 0.00000; 0.00000; 0.00000; 0.00000; 0.00000;      0.000
IA COMP  8; 1;4;7.608321596557e-08;1729.65654; 228.15233; 223.54779;1; 0.84171; 0.53989;-0.00664; 0.00000; 0.00000; 0.00000;   110.584;3;-0.96972; 0.03868;-0.24115; 0.00000; 0.00000; 0.00000;     39.273
IA PHOT  9; 1;4;7.610050271129e-08;1730.09275; 228.43212; 223.54435;1; 0.00000; 0.00000; 0.00000; 0.00000; 0.00000; 0.00000;     0.000;3; 0.37878; 0.92445;-0.04384; 0.00000; 0.00000; 0.00000;     77.428
IA PHOT 10; 1;4;7.610050271129e-08;1730.09275; 228.43212; 223.54435;1; 0.00000; 0.00000; 0.00000; 0.00000; 0.00000; 0.00000;     0.000;1; 0.30543; 0.52611;-0.79367; 0.00000; 0.00000; 0.00000;     28.306
IA PHOT 11;10;4;7.610560699643e-08;1730.13949; 228.51263; 223.42298;1; 0.00000; 0.00000; 0.00000; 0.00000; 0.00000; 0.00000;     0.000;3;-0.25449; 0.92907;-0.26846; 0.00000; 0.00000; 0.00000;     23.752
HTsim 4;1720.00000; 230.00000; 190.00000; 423.28813;0.00000e+00;3;4;5;6;8;9;10;11
```

Fig. 5.2: Structure of a simulation file. The first part describes the simulation input parameters like geometry, physical input parameters or the date. Next comes the header section with main information about the simulated photon, followed by the interaction section which describes the interaction this photon has made. The interaction section contains information about the process itself, the energy deposited, the direction and the origin of the photons.

the interaction list, which represents the 'Monte Carlo Truth'. Every physical process is recorded with its precise spatial coordinates, timing, and energy transfer to secondary particles (e.g., recoil electrons). These entries are organized through a parent-daughter tracking system, enabling the reconstruction of the complete interaction tree for every incident particle. Finally, the hit section represents the digitized detector response. In this stage, all energy depositions occurring within the same sensitive detector volume like a specific pixel or crystal bar are spatially and temporally integrated. While the physical truth may consist of multiple discrete interactions within a single volume, a physical detector has finite spatial and temporal resolution. Consequently, the recorded energy in a hit entry is the sum of all kinetic energy deposited by secondary charged particles that are stopped within that specific detector element. This hierarchical output format enables a clear distinction between the microscopic physical truth and the macroscopic signals that would be recorded by the actual detector hardware, providing the necessary data for subsequent event reconstruction and analysis of shielding efficiency.

5.2.2 GEANT4 - The Machine Behind

GEANT4 is a comprehensive software toolkit for simulating the interaction between particles and matter. It serves as a powerful foundation to model physical processes

and detector configurations with high precision and flexibility. GEANT4 is the successor of GEANT3, which was known as the world-standard for High-Energy Physics (HEP). It is one of the first successful attempts to redesign a new CERN software package for the next generation of HEP experiments. This implementation of an object-oriented environment took place in C++ in 1995. Since it is created from a worldwide collaboration of physicists and software engineers it can expand without impairment of the original purpose. Moreover, the object-oriented approach grants a simplified expansion of the toolkit in a way that the physics implementation is transparent so that new models can easily be added [Allison et al., 2006, Agostinelli et al., 2003, Asai, 2006].
In its core, GEANT4 provides the fundamental properties and skills for modelling experimental setups. This firstly comprises the tracking of particles through matter when doing simulations and the description of detector and model structures. The definition of the participating specific materials as well as the management of events and (simulation) runs is part of the core of GEANT4. In these simulation runs, different physics models are provided which makes it able to access different physical processes. GEANT4 provides comprehensive coverage across a vast energy range, supporting electromagnetic, hadronic, and optical processes for a wide variety of particles, including leptons, photons, and ions. To ensure accuracy, the toolkit allows users to select from various physical models based on theoretical frameworks, experimental datasets, or empirical parametrizations. Its applications are widespread like medical physics, nuclear physics but also particle accelerator design and astrophysics [Allison et al., 2006, Agostinelli et al., 2003].
As a huge difference compared to previous simulation toolkits, GEANT4 does not define the cutoff, which represents the range of secondary particles, through an energy but through a length. This makes more sense physically since the range of a particle is stronlgy dependent on the particle and the material. This does not mean a track is killed at a specific energy, it is traced down to zero kinetic energy. Another feature is the cut-per-region. This allows GEANT4 to regionally specify the production thershold, which is the minimum range a secondary particle must be able to travel in a material to be generated as a discrete track e.g. low thresholds for high-sensivity detectors and high thresholds for low-sensivity detectors. By doing this the running time of a simulation can be reduced significantly without affecting energy deposition accuracy. This feature is not included in MEGAlib for the general purpose which would make native GEANT4 simulations always faster. The GEANT4 toolkit has the option of variance reduction which reduces the statictical uncertainty while saving time [Zoglauer, 2006b, Allison et al., 2006, Agostinelli et al., 2003, Asai, 2006].

5.3 Simulation Setup and Execution

This section describes the main principle behind the simulations as well as the different parameters which are varied to investigate the detector response and the TGF detection probability.

5.3.1 Monte Carlo Simulation Principles

Monte Carlo Simulations (MCSs) are based on iterative stochastic sampling and statistical modeling to derive outcomes and emulate complex systems. It is frequently used in scenarios that are not analytically solvable. Thus, the MCS typically follows a systematic approach. It starts with the modelling and preparation – prior to any actions being made, a deterministic statistical model must be constructed to describe the system. This system is subsequently characterized as a sequence of Probability Density Functions (PDFs), starting with the formulation of a deterministic model that utilizes the most probable values. To find the appropriate distribution, numerical models are employed and calibrated to historical data in a way that reflects the reality to the greatest extent possible. To select the correct parameters, methodologies such as the maximum likelihood estimation are used. By defining the PDFs, risk components which originate from the stochastic nature of the input variables, can be introduced to the model since the PDFs work as a source for the input parameters. The next step is the sampling: random variates are drawn from the distribution so that one set of random variates describes the input parameters for a simulation run. After choosing input parameters they are put into the deterministic model to get a set of output parameters. This whole process is then repeated multiple times to get a sample of output values. The analytic properties of MCSs are based on the fact that independent and identically distributed random numbers can be generated and furthermore transformed to get a sample from a non-uniform distribution. The entirety of the output values is statistically analysed so that typical parameters like mean values, variances or the shape of the PDFs can be derived.

5.3.2 Parameter Variations and Studied Scenarios

To investigate the detectability of TGFs, it is essential to examine various parameters. The first thing we look at is the material to gain insights regarding the effective area, thereby enabling informed conclusions about the optimal detector materials. The effective area quantifies the detector's sensitivity to incoming radiation and is influenced by the chosen material and detector geometry. By systematically varying the materials, we can assess how different materials affect the detector's response to TGFs. The simulations are conducted with a fixed input energy while the zenith angle is systematically varied to get the detectors response for specific angular configurations. This procedure is being repeated for several materials, as well as considering scenarios where the detector is either unshielded or located inside of a surrounding structure, namely the Kugelalm. A single material is selected and utilized consequently throughout the following simulations. The detector which will be placed inside the Kugelalm is made out of NaI which is also a common material for γ-ray detectors so this is the material of choice used for all further simulations.The following stage involves the reverse of the previous approach: maintaining a constant angle while varying the energy to derive a precise energy response function for the detector. Given the asymmetrical nature of the hut in relation to the zenith angle, this analysis is performed across diverse configurations of both θ and ϕ.
Beside of the spectral response of the detector we are also interested in the directional response since the surrounding of the detector is not symmetric. To gain insights about the directional response, isotropic simulations for the range $0° < \theta < 90°$ and $0° < \varphi < 360°$ are performed. By evaluating this scenario, the directional response can be genrated. This procedure is then repeated for several monoenergetic simulations to analyze the energy-dependence of the directional response.

5.4 Simulation Methodology

This section describes the used setup for the simulations as well as the assumptions and simplifications made to perform the simulations. The influence of the surrounding environment and the corresponding detection influence is shown as well.

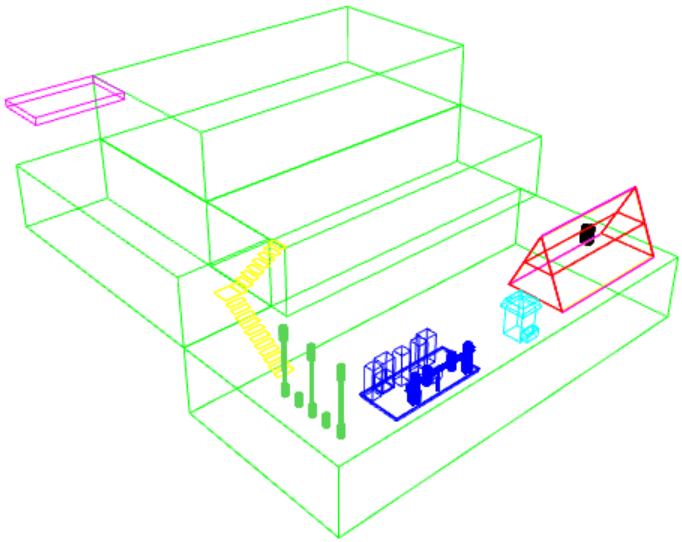

Fig. 5.3: The used Geomega setup. The cylindrical detector is made out of NaI and placed inside the Kugelalm (red): a triangular hut with a roof consisting of wood and aluminum. The big blocks (green) are the different measurement platforms on the UFS, made out of concrete. Other significant objects like the poles (green), the stairs (yellow), the roof (purple) or some detector setups (cyan, blue) are also included since they may be in the field of view of the detector located inside the Kugelalm.

5.4.1 Source and Geometry Models

The used geometry model which rebuilds the UFS environment is shown in Fig. 5.3. It shows the different measurement plateaus (green) which are made out of concrete as well as several features built on there: the stairs (yellow), the roof (purple) when entering the outer part of the UFS and different measurement setups (green, blue, cyan). The most important part is the Kugelalm (red) which is the triangular hut and consists of a wooden and aluminum roof (pink). The detector is placed inside the Kugelalm on a horizontal plank. This setup is used for all further simulations. To build the Geomega model the station and the necessary structures were measured by hand with a measuring tape. While the measurement structures outside are permanently set up, the interior of the Kugelalm is variable. Additionally, the detector will be placed in the upper part of the Kugelalm while the majority of the existing setup is located in the lower part which makes it not necessary to rebuild this in the simulation.

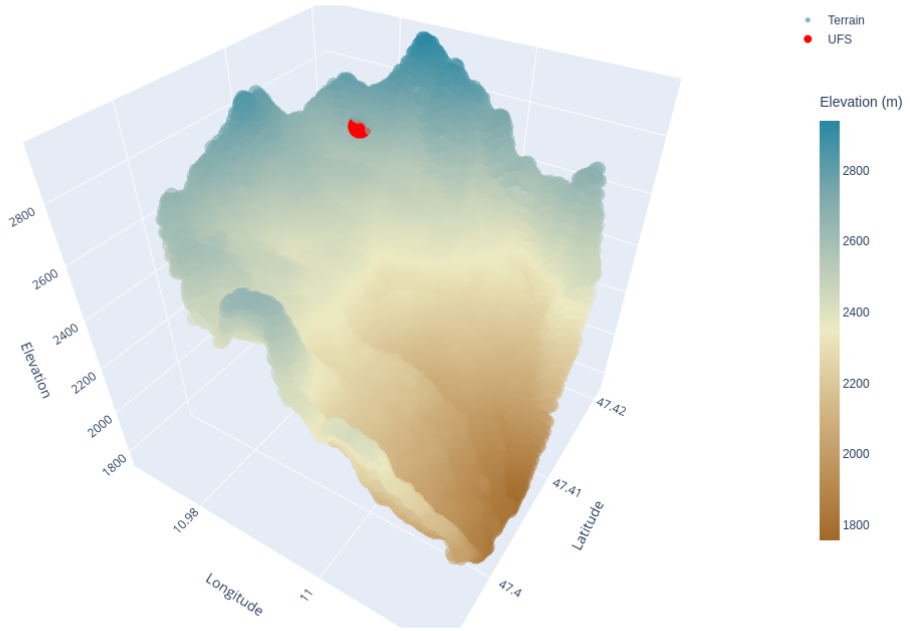

Fig. 5.4: Three-dimensional model of the UFS environment. The station is situated on a steep rock face, with topography defined by elevation data from [UFS Elevation] where the area around the UFF and the surrounding mountains were manually selected. The model uses a resolution of 1 arc-second, corresponding to approximately 30 m.

5.4.2 Influence of Topographic Effects

The complex topography surrounding the UFS significantly influences the detection of TGFs. Given that the UFS is located in the alpine region on a rock face, as depicted in Fig. 5.4, the observation capacity of the measurement instruments placed in this location is constrained. Due to the measurement apparatus not being placed at the summit of the Zugspitze, certain directional views are obstructed by the surrounding mountains. The mountain peaks near the UFS can partially shield the detector from photons arriving at lower elevation angles. To quantify this influence and gain a more comprehensive understanding of the obstructed directions, a horizontal profile can be constructed. Fig. 5.5 illustrates the outline of the mountains from the perspective of an observer positioned at the location of where the detctor is located in the Geomega model. Since some directions are blocked by the mountains, this should be taken into account when doing simulations and measurements.

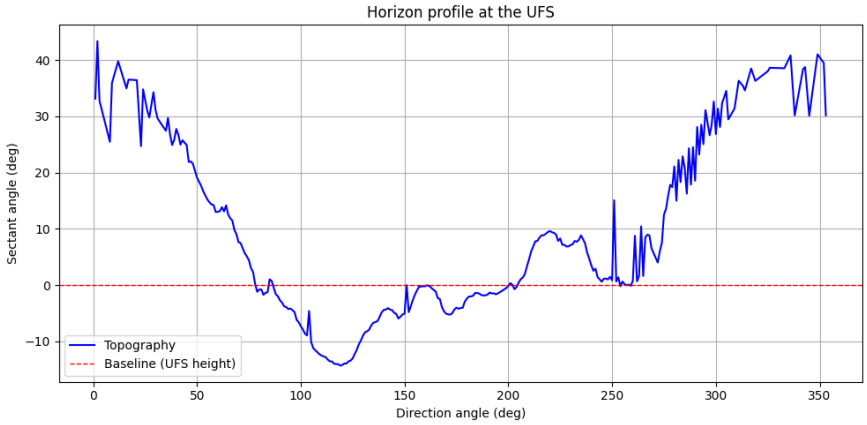

Fig. 5.5: A two dimensional horizon profile of the UFS if an observer is standing where the detector will be placed. The blue line shows the silhouette of the mountains, defining the areas where no signal can be detected. The red dashed line describes the baseline as the position where the detector is placed. This profile was derived from the elevation data in Fig. 5.4 by calculating the maximum elevation angle for each azimuthal direction. A direction angle of 0° corresponds ot the geographic direction north.

5.4.3 Assumptions and Simplifications

First of all, we posited that the TGF source is a point source. Given the uncertainty regarding the precise mechanisms underlying the formation of TGFs and the fact that a source of any shape can be modeled as a collection of point sources, this simplifiaction fits the conditions necessary for doing simulations. The atmospheric model does not incorporate specific elements and densities, instead we employ a transmittance to characterize the photons traversing the atmosphere. This atmospheric component was excluded during simulations involving different materials or angles. This is because the simulation time would increase by several orders of magnitude due to the exponential increase number of scattering processes. Concerning the model utilized for the simulations, it was presumed that the measurement platforms are solid and constructed of pure concrete. The chemical composition of the materials used in the Geomega setup are summarized in Tab. 5.1. Since the concrete platforms are located in front of the mountain as seen from the detector point of view, this direction is blocked for detecting TGF signals. Only the measurement instruments beside of our detector, which might influence the measurement of TGFs due to geometric constraints are included, as illustrated in Fig. 5.3. The effects of snow or rain on the platforms were entirely disregarded since this is not the default weather condition at the Zugspitze. Regarding the impact of natural radioactivity, only the outer 30 cm layer of concrete is considered

Material	Density gcm^{-3}	Composition element	Percentage
Concrete	2.35	H	0.01
		C	0.0001
		O	0.529107
		Na	0.016
		Mg	0.002
		Al	0.033872
		Si	0.337021
		K	0.013
		Ca	0.044
		Fe	0.014
Aluminum	2.7	Al	1
Steel	7.87	Fe	0.712890625
		Cr	0.17578125
		Ni	0.08203125
		Si	0.009765625
		Mn	0.009765625
		C	0.009765625
Wood	0.76	C	0.505
		O	0.43
		H	0.064
		N	0.001

Table 5.1: Chemical composition of the materials used in the Geomega simulation.

to contribute. For material located at greater depths, self-absorption occurs, effectively preventing this radiation from reaching the detector. The natural radiation is presumed to originate from concrete itself since concrete and rock are the typical emittors for natural radioactivity. By assuming the same radioactive decays happening in the concrete and in the mountains it is sufficient to consider the natural radioactivity originating from the concrete close to the detector.

6 Results

This chapter describes the results of the thunderstorm probability as well as the detection probability of TGFs at the UFS. Different detector materials are compared and the detector response is analyzed in detail. In both cases it is compared if the detector is simulated with or without the Kugelalm.

6.1 Thunderstorm Probability

For determining the probability of a measureable thunder occuring with a TGF signal, a lower estimation based on monthly thunderstorm hours is used. This estimation is derived, using the publicly accessible WWLLN data stored on the WWLLN website. This work is using annual files between 2013 and 2024, thus averaging over 11 years.
According to DiGangi et al. [2022], a thunderstorm hour requires the detection of at least two lightning discharges within a 15 km radius of a specific grid point during a one hour window. To implement this, a $0.05^\circ \times 0.05^\circ$ latitude-longitude grid is setup and each cell is evaluated by setting their value to 1 if the necessary conditions are met. Otherwise the value is set to 0.
Since the audibility of thunder varies with different aspects like atmospheric conditions, distance and terrain, the number of thunderstorm hours is distance dependent. In this work, radii of up to 10 km are analyzed and taken into account with the location being the position of the UFS where the detector is located: (lat, lon) = (47.4165, 10.97964). The averaged results of monthly thunderstorm hours for different radii are illustrated in Fig. 6.1. The curves for the different radii are calculated and drawn after each other so for the case $1.5\,\text{km} < r < 3.5\,\text{km}$ the curves have the same shape so they are visible as a single curve. To further analyze the TGF probability, one month is chosen from Fig. 6.1. July has the most averaged thunderstorm hours with 228 thunderstorm hours

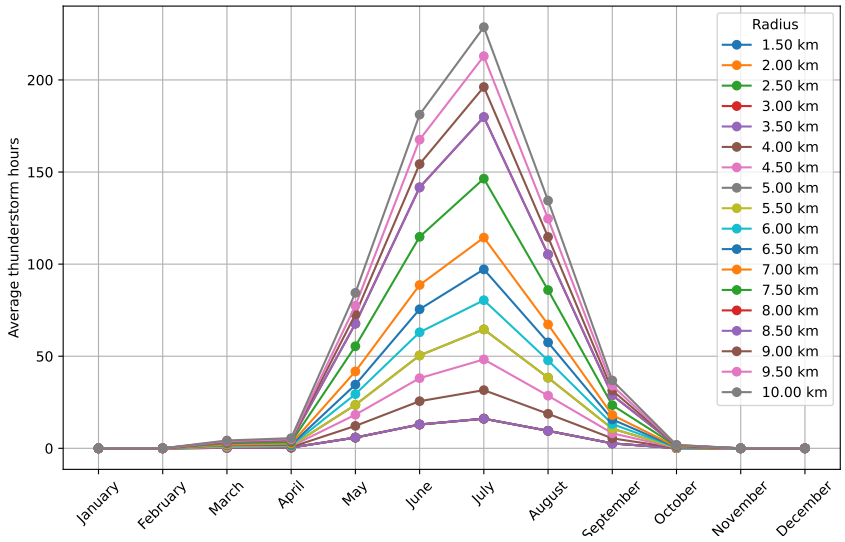

Fig. 6.1: Average thunderstorm hours for different radii average for the years 2013 - 2024. Some radii are described by the same values which results in a curve not being drawn for all radii. This is the case $1.5\,\text{km} < r < 3.5\,\text{km}$, which happen to be described the same curve.

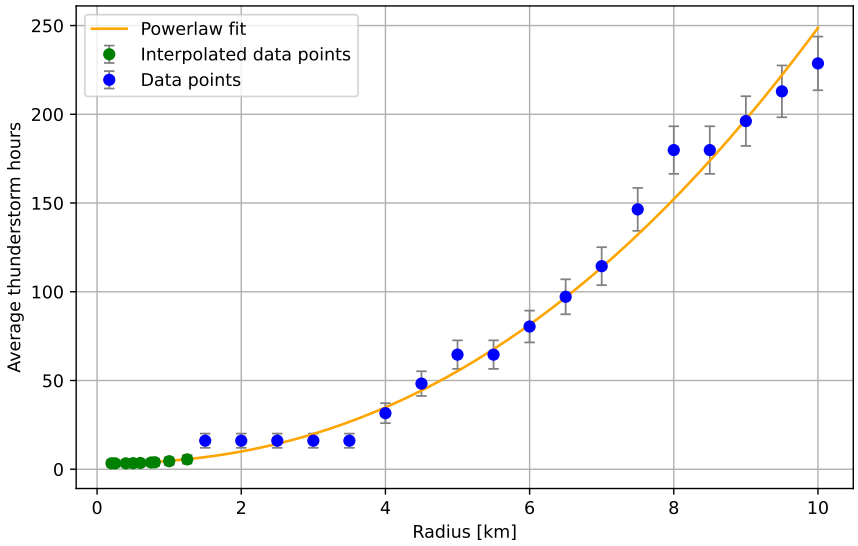

Fig. 6.2: Average thunderstorm hours in July as a function of radial distance. The trend is modeled using a power-law fit applied to a combined dataset. For distances $r < 1.5\,\text{km}$, where empirical data is unavailable, values were extrapolated using a second-degree polynomial to provide a physically consistent transition toward the origin. The original data points are shown alongside the interpolated points used for the final fit.

per month, so the following analyses are done with this month. In Fig. 6.2 the average thunderstorm hours for the different radii in July are visualized.
For radii r<1.5 km, the average thunderstorm hours were extrapolated using a second-degree polynomial to provide continuous estimation in this region of interest. Subsequently, a powerlaw fit was applied to the combined set of interpolated and empirical data points to describe the frequency of thunderstorm hours as a function of distance from the center. The result shows a range of monthly thunderstorm hours between 3 hours for a radius of 500 m and 248 hours for a radius of 10 km. The powerlaw fit has the shape

$$f(r) = 1.413 \cdot r^{2.24} + 3.316 \tag{6.1}$$

6.2 Detection Probability

In addition to the likelihood of a TGF occurring within a measureable distance, it is also crucial to know the probability of detecting a TGF. The transmissivity of this process was calculated utilizing Equation (3.13) with $h_D + d\cos\theta$ being the altitude of the TGF source which was set to 10 km. The calculated transmissivity is subsequently calculated and illustrated for various energies and within the angular range of $0° < \theta < 90°$, which is shown in Fig. 6.3. For small input energies $E_{in} \leq 1$ MeV the transmissivity is significantly lower by 10 orders of magnitude in comparison to energies $E_{in} \geq 5$ MeV. Electrons with lower energy are more susceptible to being absorbed during their traversal through the atmosphere, leading to a reduced probability of their detection. In contrast, for higher energies this effect decreases as high-energy photons have significant kinetic energy after scattering in the atmosphere, thereby substantially increasing their likelihood of reaching the detector. This is further shown by the observation that the transmittance curves are getting closer to each other at higher energies. As shown in Fig. 6.3, the input angle significantly influences photon detection, especially when assuming a constant source height. By incorporating this assumption the photon trajectory through the atmosphere lengthens progressively with increasing θ. For smaller energies such as $E = 100$ keV the transmissivity remains nearly stable for $0° < \theta < 10°$, after which it experiences a rapid decline. For higher energies such as $E = 50000$ keV the transmissivity remains stable for $0° < \theta < 40°$, allowing photons to be detected with equivalent probability over a significantly larger angular range. Consequently, the detection of TGFs is most effective when measuring high-energy photons at

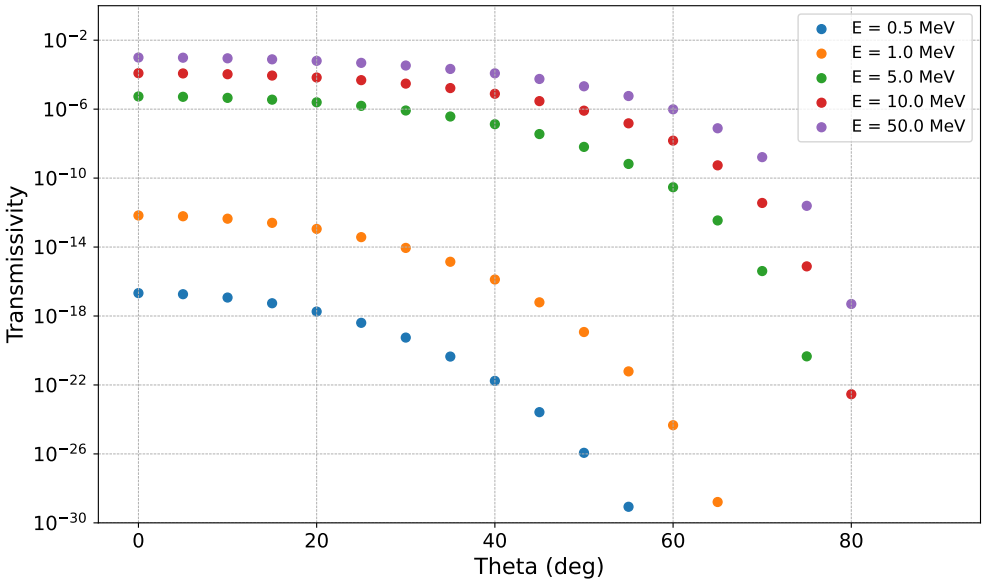

Fig. 6.3: Transmittance for different energies, depending on the photon input angle. The detector altitude is set to 2657 while the source altitude is set to 10 km. For higher energies the angular range for a transmissivity remaining unchanged is much bigger compared to lower energies. The higher the energy the more scatterings, resulting in a longer trajectory from source to detector which is equivalent to a larger angle θ. For lower energies the transmittance is significantly lower.

near-nadir input angles, as this combination minimizes atmospheric attenuation while maximizing the effective detection area.

6.3 Detector Materials and Shapes

To determine the detector efficiency for different materials we performed simulations for input angles θ with an angular range of 0° - 180° in 10° steps. The materials NaI, Ge and $Bi_4Ge_3O_{12}$(BGO) with photons carrying an energy of $E = 1\,MeV$ were analyzed. The azimuthal angle φ was set to 0° resulting in an input direction through the side of the Kuglelalm instead of through the aluminum roof for $\theta = 90°$.
Also, the difference between measurements with and without Kugelalm were analyzed. The main task of this simulation is to determine and visualize differences between different detector materials. Therefore, just the Kugelalm and the detector were used in the simulation's geometrical model. The concrete platforms seen in Fig. 5.3 were left out due to computational restraints because they affect all three materials and would

not get additional information if we are just interested in the effects of the different materials. The simulations were done for a simulation time T = 300 s and a flux F = 1 ph cm^{-2} s^{-1} which converts into an amount of detected particles through

$$N = A \cdot F \cdot T = (\pi r^2 \cdot \cos\theta + 2rh \cdot \sin\theta) \cdot F \cdot T \tag{6.2}$$

where r is the detector radius, θ is the zenith input angle, F is the photon flux and T is the simulation time. For computational reasons the detector in the simulations is increased by a factor of $r_{new} = 8 \times r_{old}$ and $h_{new} = 8 \times h_{old}$ resulting in an effective area of $A_{eff,\,new} = 512 \times A_{eff,\,old}$. A scaling factor of 512 is a rather lower estimate. Since the increase in size combines the enlargement of the geometric cross-section and the microphysical interactions, the effective area is probably incresed even more. The increased colume improves the inclusion of secondary particles and Compton-scattered photons which would escape otherwise when using a smaller detector. These effects are compensated by dividing the effective area in all further formulas by an efficiency factor that is at least 512. Because the detector is of cylindrical shape with a radius r= 28 cm and a height h = 80 cm, the amount of detected photons changes depending on the input angle which is seen in Tab. 6.1. Since the detector dimensions are fixed, the ratio of detector radius r and detector height h is kept constant. The resulting effective areas for the different input angles are shown in Fig. 6.4.

The intial observation pertains to the higher effective area for the scenarios where the detector is not placed inside of the Kugelalm. The affected area is assessed through the equation

$$A_{\text{eff}} = A_{\text{start}} \times \frac{N_{\text{photo}}}{N} \tag{6.3}$$

where A_{start} represents the starting area determined by the system, N_{photo} is the number of photons which are detected for energies within ± 10% of the photopeak and N is the total number of detected events. When the detector is placed inside the house, the effective area is reduced due to the shielding effect of the structure. Low-energy photons become absorbed within the building materials and fail to reach the detector. Other particles undergo scattering – while some may still reach the detector at a deflected angle and lower energy, many are redirected away from the detector's active volume entirely. A symmetry around $\theta = 90°$ is visible because the detector is of cylindrical shape and is not shielded.

When we position the detector inside the Kugelalm several distinct effects become observable. The presence of the wooden and aluminum shielding layer results in the scattering of a greater number of photons. More photons are scattered away from the

Input angle [deg]	Number of detected photons ($\times 10^8$)
0	2.36
10	2.07
20	1.74
30	1.62
40	1.58
50	1.58
60	1.62
70	1.74
80	2.07
90	2.36
100	2.07
110	1.74
120	1.62
130	1.58
140	1.58
150	1.62
160	1.74
170	2.07
180	2.36

Table 6.1: The number of detected photons for every input angle θ for a photon input energy of $E_{\text{in}} = 1\,\text{MeV}$.

detector than towards it or get absorbed, which consequently leads to a reduction in the number of photons detected. Furthermore, the symmetry around $\theta = 90°$ is no longer present as the Kugelalm lacks symmetry with respect to the detector along the z-axis. For angles $\theta > 90°$ the effective are is increased relative to $\theta < 90°$. The reason for that is the reduced thickness of the Kugelalm given that the roof comprises both a wooden and an aluminum layer whereas the sides consist solely of a wooden layer. In the applied scenario for $\theta = 0°$ the photons are simulated for zenith direction while for $\theta = 90°$ the photon direction is perpendicular to the lateral wooden wall.
The detector has been positioned in the middle of the Kugelalm resulting in the condition that for $0° < \theta < 70°$ the photons must pass through aluminum and wood. Conversely, for $70° < \theta < 90°$ the photons encounter the wooden lateral wall of the Kugelalm at an almost perpendicular angle. The absence of the necessity to traverse aluminum allows for a greater number of photons to reach the detector, thereby explaining the abrupt increase observed at $\theta = 80°, 90°$.
In the comparative analysis of various materials, it becomes evident that BGO exhibits the largest effective area, serving as the benchmark for detection efficiency. As established in Section 3.2, the interaction cross-section is strongly correlated with the atomic

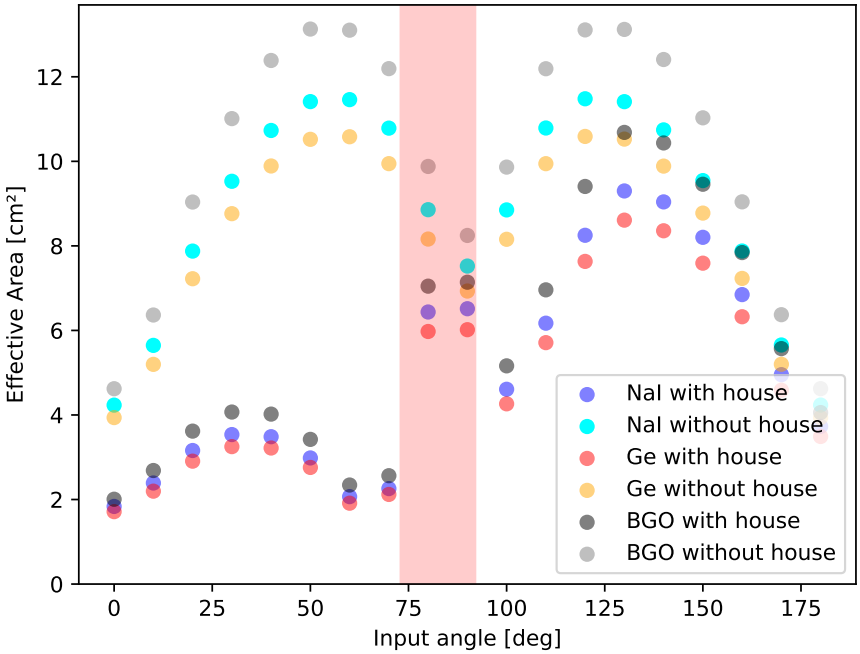

Fig. 6.4: Effective area in cm^2 for different detector materials (BGO, NaI and Ge) for a detector placed both inside and outside the *Kugelalm*. The photon input energy is $E = 1\,\mathrm{MeV}$ and we shoot them in vertically from above from zenith angle $\theta = 0°$ that the photon direction is aligned with the positive z-axis. The input angle is increased in 10° steps to $\theta = 180°$ and the simulations are performed for the case that the detector is placed inside or outside the Kugelalm. The red shaped range shows the angular range in which the photons traverse just the lateral wooden wall.

number Z. Due to its high Z and density, BGO provides the highest stopping power, resulting in the largest effective area and detection efficiency. Despite BGO's efficiency, other materials are evaluated against it. As compared by Milbrath et al. [2008], it was demonstrate that NaI offers a light yield, which describes the efficiency to transform ionizing radiation into visible light, more than four times higher compared to BGO. Furthermore, NaI crystals are more commercially accessible and cost-effective to produce in large volumes. Also, they are easier to grow with high purity. Consequently, while BGO remains the standard for maximum photon capture, NaI was selected for the subsequent simulations in this work. This choice allows to prioritize practical feasibility without significantly compromising the required sensitivity. Wada et al. [2019b] also used NaI detectors in their TGF measurements, which allows us to compare the simulation results with actual measured values.

6.4 Detector Response

To gain insights about the detector response, monochromatic simulations ranging from 100 keV to 10 MeV are performed. The resulting plots for the detector's absorbed energy spectra are shown in Fig. 6.5. Starting with 100 keV, a clear photopeak is visible for both scenarios. Also, for the case of no house the Compton edge at ≈ 75 keV is visible. If the NaI detector is placed inside the Kugelalm the photopeak is significantly smaller and the Compton edge is not visible. For input angles $\varphi = -90°$ and $\theta = 25°$ there are slight signs of a peak at 70 keV. When the input angle θ changes from zenith to $\theta = 25°$ there are more detected photons if the NaI detector is not placed inside the Kugelalm. The reason for that is the increased effective area as already seen in Fig. 6.4.
By increasing the photon input energy to $E_{\text{in}} = 1000$ keV the resulting spectra show a lot more effects. Since the input energy is higher and the scattering effects appear more often there are more lower energetic photons reaching the detector. If the house is not included in the simulation, a dip in the spectra in the range of 200 – 700 keV is visible. For the zenith angle simulation this dip is deeper compared to the other case. The origin of this dip is Compton scattering since this process dominates in this energy range. For the zenith direction the effective area is lower compared to the other direction and a lower effective area results in less scatters. For the case of placing the NaI detector inside the Kugelalm the photons need to traverse more material so the probability of multiple scatterings is much higher.
For even higher input energies of 10000 keV the *gamma*-ray spectrum drastically changes. The ratio of counts with house compared to counts without house strongly increases compared to the lower energy scenarios as seen in Fig. 6.6. The Compton dominated energy range is visible at 700 – 7000 keV where for the scenario of the detector placed witout the house a dip emerged. As seen in Fig. 3.9 for this energy range Compton scattering is still the dominant process while for higher energies pair production dominates. A new feature emerging for high input energies is a peak at $E_{\text{in}} = 511$ keV. This peak originates from pair production and the corresponding electron positron annihilation when the input energy of photons surpaces the threshold of $E_{\text{in}} = 1.022$ MeV.
As illustrated in Fig. 6.6, detection efficiency is highly dependent on the energy of the incident photons since more photons are detected for increasing energy. For photons with energies around a few hundred keV, more counts were observed when the detector is placed without the Kugelalm. For higher photon energies $\geq$1 MeV, the amount of detected counts increases when placing the detector inside the Kugelalm. The total counts for both cases are shown in Fig. 6.7. The progression of the datapoints is largely

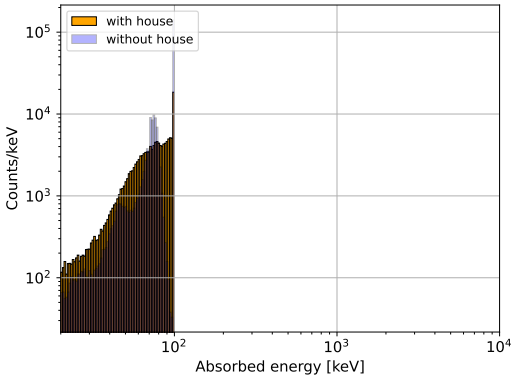

(a) $E_{\text{in}} = 100$ keV, $\varphi = 0°$, $\theta = 0°$

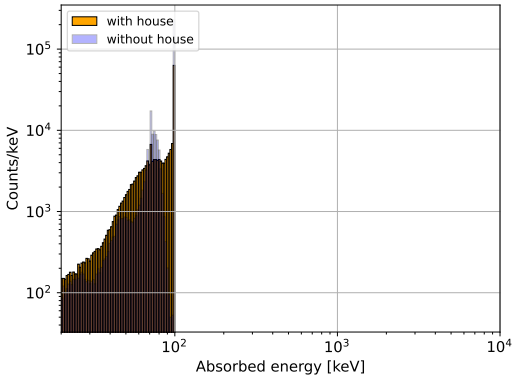

(b) $E_{\text{in}} = 100$ keV, $\varphi =$ -90°, $\theta = 25°$

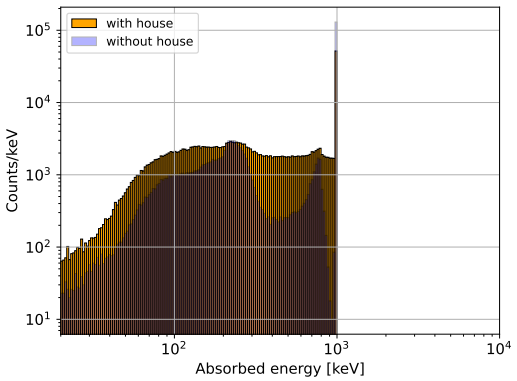

(c) $E_{\text{in}} = 1000$ keV, $\varphi = 0°$, $\theta = 0°$

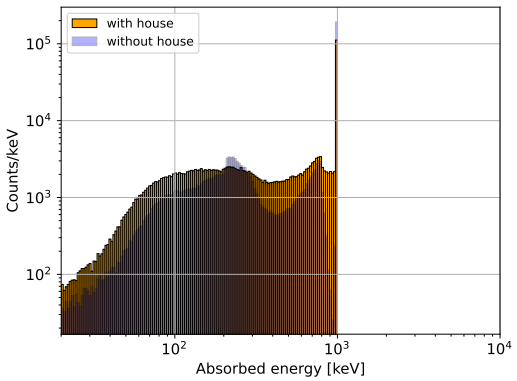

(d) $E_{\text{in}} = 1000$ keV, $\varphi =$ -90°, $\theta = 25°$

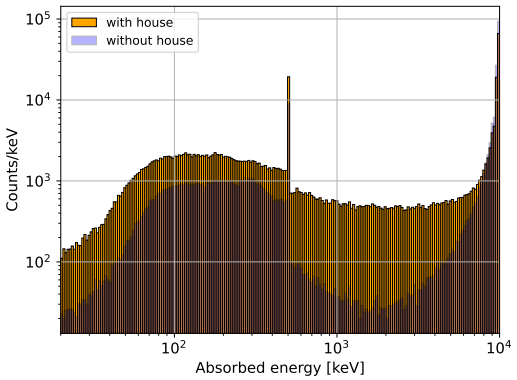

(e) $E_{\text{in}} = 10000$ keV, $\varphi = 0°$, $\theta = 0°$

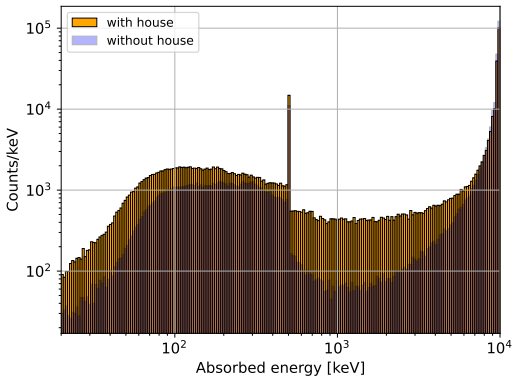

(f) $E_{\text{in}} = 10000$ keV, $\varphi =$ -90°, $\theta = 25°$

Fig. 6.5: Absorbed energy spectra of different (φ, θ) combinations and monochromatic input energies. $1.18{\times}10^9$ starting photons are simulated.

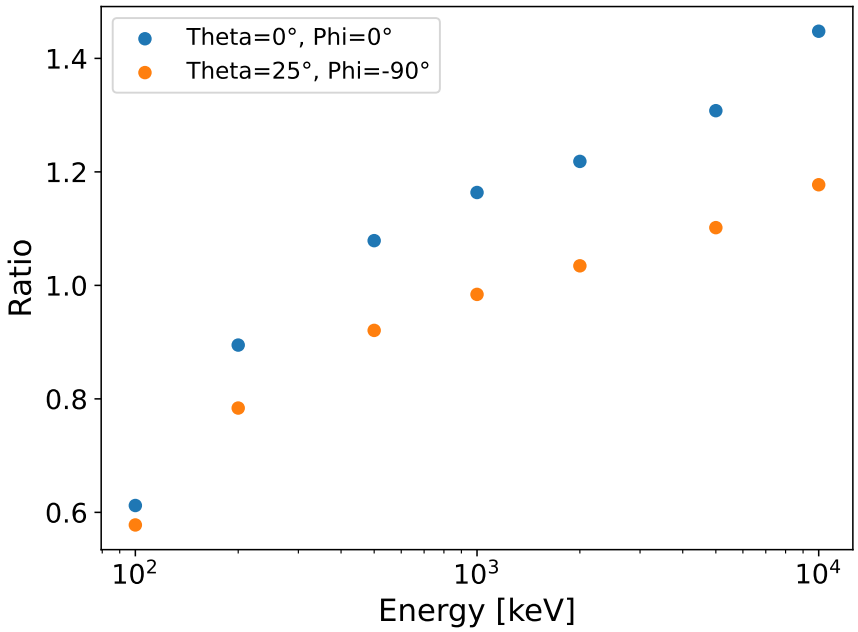

Fig. 6.6: Ratio of counts when the detector is placed inside the Kugelalm over counts if the detector would be placed without the Kugelalm. The angle configurations are the zenith input scenario ($\theta = 0°, \varphi = 0°$) and the case where the input angle is orthogonal to the Kugelalm wall ($\theta = 25°, \varphi = -90°$).

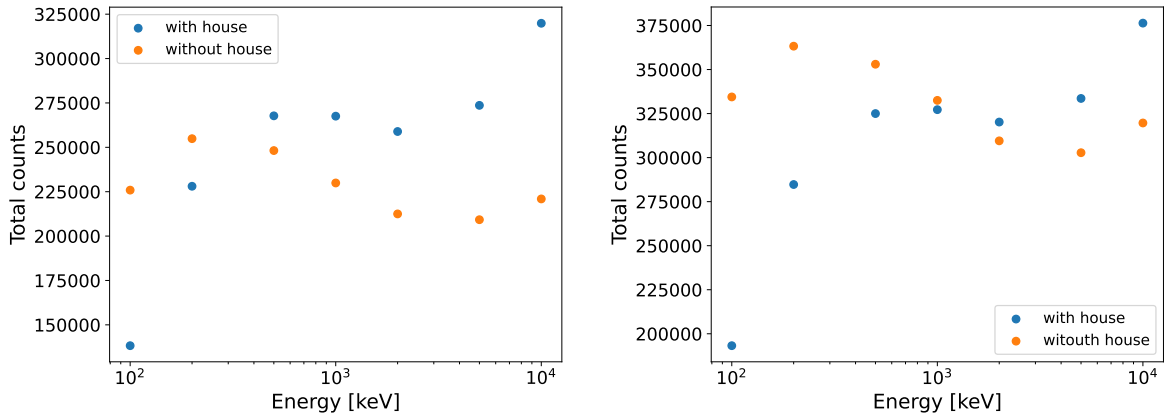

(a) **(b)**

Fig. 6.7: Total counts for the two cases when (a) the input direction is $\theta = \varphi = 0°$ and (b) when the input direction changes to φ = -90°, θ = 25°. In (b) the azimuthal angle φ describes the direction where the photons travel through the aluminum roof so φ = -90° is orthogonal to the Kugelalm roof.

similar for both cases. In the low-energy regime, the observed increase in total counts is driven by the dominance of the photoelectric effect, which ensures the complete absorption of incident photons within the detector volume. Within this range, the mass attenuation coefficient is significantly higher compared to intermediate energies, leading to a high intrinsic detection efficiency. As the incident energy increases towards 1 MeV, the probability of photoelectric interaction decreases. In this intermediate energy range, Compton scattering becomes the primary interaction mechanism. Since Compton scattering involves only partial energy deposition, there is a higher probability that photons scatter out of the detector volume without being fully registered, which explains the observed decline in total counts. At even higher energies (> 1.022 MeV), pair production emerges as an additional interaction process. The increase in the pair production cross-section at very high energies of up to 10 MeV leads to the subsequent rise in total counts observed in the 'without house' data.

Processes such as pair production and subsequent Bremsstrahlung create a multiplication effect, where a single primary high-energy photon generates a cascade of secondary photons. These secondary particles are registered by the detector, resulting in the observed peak in total counts at the highest energy.

For the following simulations the Kugelalm is included since the number of total counts is significantly higher for higher input photon energies. Knowing the detectability difference of the detector placed inside the Kugelalm or not and the spectral response is one important thing, knowing the directional response is of similar importance. Depending on the input direction there might be a significant difference in the amount of detected photons. To analyze this, we performed isotropic monoenergetic simulations. The resulting plots which also include effects from the surrounding environment are shown in Fig. 6.8. For incident energies of $E_{\text{in}} = 100$ keV, the silhouette of the Kugelalm is clearly visible as a triangular structure in the resulting plot. This pattern, appearing at $\varphi = \pm\ 30°$ and $\varphi = 160°$, corresponds to azimuthal directions where the structural material thickness is at its maximum. Consequently, the increased path length leads to higher photon absorption and a localized reduction in the count rate, effectively mapping the building's geometry onto the detection profile. Also, for some angle combinations there are no measured counts at all. The UFS is located at the mountainside as seen in Fig. 5.4 and therefore some input directions like between $\varphi = 180°$ and $\varphi = 15°$, as well as between $\varphi = -120°$ and $\varphi = -150°$ are blocked by the mountains.

For higher energies like $E_{\text{in}} = 10000$ keV the input direction does not matter as much as for lower input energies which can be seen in a way that the pixels in the Fig. 6.8 have similar intensity, no matter fomr which direction they originate. In this case the

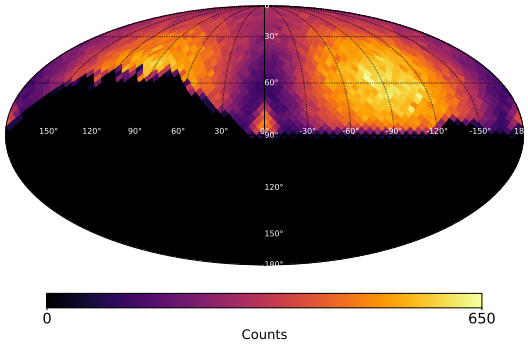

(a) Measured counts per pixel from isotropic simulation for $E_{\text{in}} = 0.1$ MeV

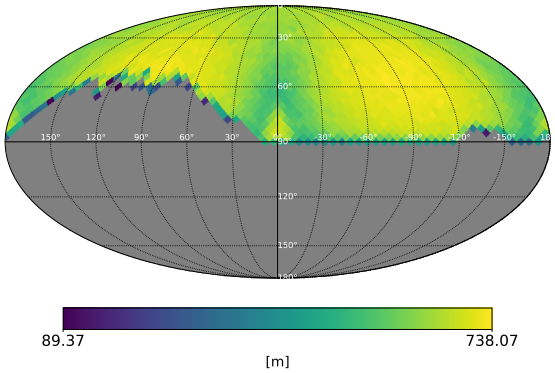

(b) Calculated maximum distance for $E_{\text{in}} = 0.1$ MeV

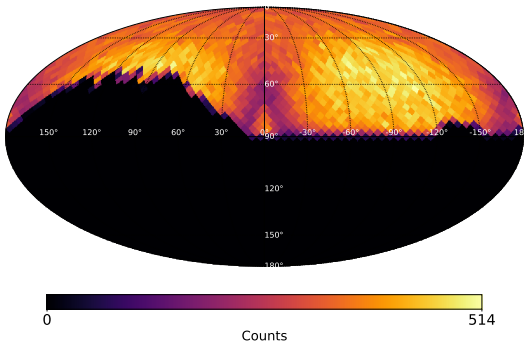

(c) Measured counts per pixel from isotropic simulation for $E_{\text{in}} = 1$ MeV

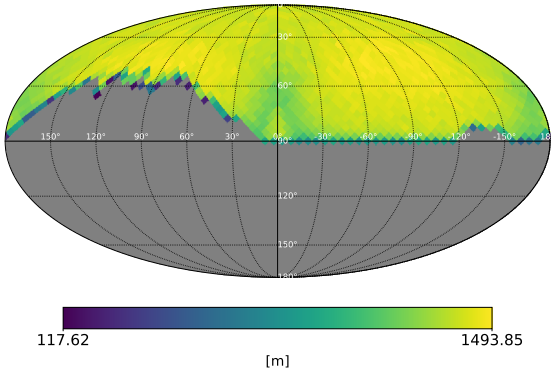

(d) Calculated maximum distance for $E_{\text{in}} = 1$ MeV

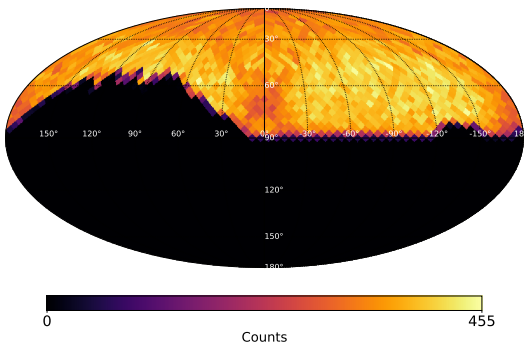

(e) Measured counts per pixel from isotropic simulation for $E_{\text{in}} = 10$ MeV

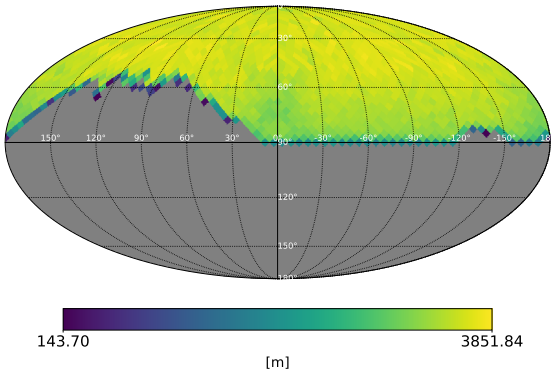

(f) Calculated maximum distance for $E_{\text{in}} = 10$ MeV

Fig. 6.8: Isotropic simulations for different monochromatic input energies. The counts per pixel were simulated (left) and with eq. (6.4) the maximum distance between source and detector was calculated (right).

amount of maximum counts is decreasing for higher energies. The simulation trigger criterion was set to 512000 events so what changes is not the amount of detected events but the distribution of the pixels of these.
A similar behaviour can be seen for the maximum distance in which a TGF source could be placed to measure a defined amount of photons per TGF. This distance is calculated with eq. (3.13) through

$$\Phi_{\text{measured}} = \Phi_{\text{source}} \cdot T_{\text{res}} \tag{6.4}$$

$$\frac{N_{\text{min}}}{\frac{A_{\text{start}}}{\eta}\frac{N_{\text{cpp}}}{N_{\text{e}}} \cdot t} = \frac{L}{4\pi d^2}\frac{N_{\text{cpp}}}{N_{\text{e}}} \exp\left[-\frac{1}{\cos\theta} H \rho_0 \mu(E) \exp\left(-\frac{h_{\text{D}}}{H}\right)\left(1 - \exp\left(-\frac{d\cos\theta}{H}\right)\right)\right] \tag{6.5}$$

and solved for d. Since this equation is not analytically solvable, a numeric approach is chosen. By trying to minimize the function f(d) = $\Phi_{\text{source}} \cdot T_{\text{res}} - \Phi_{\text{measured}}$ the algorithm finds exact solutions for d.
The left side of Equation (6.4) describes the measured flux while the right side is the source flux multiplied with the resulting transmission probability which results from $T_{\text{res}} = T_{\text{atm}} \cdot T_{\text{geo}}$. The fixed input parameters are the number of simulated events N_{e}, the minimum amount of detected photons N_{min}, the starting effective area of the detector A_{start}, the duration of the TGF t, the altitude of the detector h_{D}, the scale height H, the density of air ρ_0, the energy-dependent mass attenuation coefficient $\mu(E)$, the luminosity of the TGF source L and the efficiency factor η which is set to 512. The variable parameters are the maximum distance d, the simulated counts per pixels N_{cpp} and the input angle θ.
N_{min} is the key parameter since it gives conclusions about our signal. In this work we set N_{min} to 60 photons per TGF to have comparisons to other works such as Chaffin et al. [2024]. For RHESSI measurements at least 17 detected photons are required to identify a TGF signal [Smith et al., 2010]. Fermi GBM uses a minimum number of 20 photons per TGF for measurements with the BGO detectors. Both RHESSI and Fermi GBM have a lower N_{min} but since they are both space-based detectors, we choose our threshold to be higher to account for the higher background noise. With 60 counts the Signal-to-Noise Ratio (SNR) becomes

$$SNR = \frac{N_{\text{min}}}{\sqrt{N_{\text{min}} + N_{\text{background}}}} = 7.68 \tag{6.6}$$

with a background contribution of 1 photon by natural radioactivity.
The distance plots in Fig. 6.8 (b), (d), (f) give a good estimation on how the maximum

Energy interval [keV]	Contribution [%]
100 – 500	34.94846
500 – 1000	15.05154
1000 – 5000	34.94846
5000 – 10000	15.05154

Table 6.2: Procentual contribution to the overall flux for the different chosen energy intervals.

measureable distance evolves with increasing energy. Since a TGF is described by a powerlaw instead of a monoenergtic emission, the procedure to get the maximum distance in which a TGF with a reaslistic spectrum can be detected, needs to be adjusted. A necessary part of this calculation is the energy-dependent effective area. Due to computational reasons it is not possible to use the effetive area for every energy between 100 keV and 10 MeV, which is why an estimation is used. The isotropic simulations are done for specific energies for which the effective area is then determined. In this case, the energies 0.1 MeV, 0.5 MeV, 1 MeV, 5 MeV and 10 MeV are chosen. With these energies, the following intervals are defined: (0.1 MeV, 0.5 MeV), (0.5 MeV, 1 MeV), (1 MeV, 5 MeV), and (5 MeV, 10 MeV). Since the energy spectrum of the TGF is assumed to follow a powerlaw spectrum it is substantial to know how much every intervals contributes to the overall flux. To determine this, the following equation needs to be solved for K:

$$\int_{E_{\min}}^{E_{\max}} dE \frac{dN}{dE} = \mathrm{L} \tag{6.7}$$

$$\int_{E_{\min}}^{E_{\max}} dE K \left(\frac{E}{E_{\mathrm{piv}}}\right)^{-1} = L \tag{6.8}$$

For the given energy range $(E_{\min}, E_{\max}) = (100\,\mathrm{keV},\ 10000\,\mathrm{keV})$ and different fluxes $(L_{\min}, L_{\mathrm{mean}}, L_{\max}) = (10^{18}, 10^{19}, 10^{20})\,\mathrm{ph\,s^{-1}}$, the different K values are calculated to $(K_{\min}, K_{\mathrm{mean}}, K_{\max}) = (2.17147{\times}10^{15}, 2.17147{\times}10^{16}, 2.17147{\times}10^{17})\,\mathrm{ph\,keV^{-1}\,s^{-1}}$. Knowing K, the partial flux contribution of every energy interval can be determined. The resulting contribution is shown in table Tab. 6.2. With the procentual contributions the equation to solve for d to get the maximum distance can be set up. To get d it is important to apply the calculated weightening factor for every energy interval contribution. By doing this, the amount of photons emitted in the specific energy intervals is taken into account, respective of how many photons they emitted compared to the

source flux. The final equation which needs to be solved has the form

$$N_{\mathrm{min}} = \sum_{i=1}^{4} p_i \left(\frac{L}{4\pi^2} \cdot \exp\left(C \left(1 - \exp\left(\frac{d \cos\theta}{H} \right) \right) \right) \frac{N_{\mathrm{cpp}}}{N_{\mathrm{sky}}} A_{\mathrm{eff,i}}\, t \right) \tag{6.9}$$

where C is a factor of the form $-\frac{1}{\cos\theta} H \rho_0 \mu(E_i) \exp\left(-\frac{h_{\mathrm{D}}}{H}\right)$. For each of the intervals a reference value is chosen whereby our choice is the left boundary of each interval because by doing doing this we don't need to interpolate between the values. $\mu(E_i)$ is the corresponding mass attenuation coefficient for the chosen energy, p_i is the contribution factor of the corresponding interval and $A_{\mathrm{eff,i}} = \frac{A_{start}}{\eta} \frac{N_{\mathrm{cpp}}}{N_{\mathrm{sky}}}$ is the energy-dependent effective area calculated for the chosen reference energies. This equation needs to be solved for d, analogous to the monochromatic case. The resulting maximum distance plots for the different fluxes ($L_{\mathrm{min}}, L_{\mathrm{mean}}, L_{\mathrm{max}}$) to detect 60 photons during a 1 ms TGF duration are shown in Fig. 6.9.

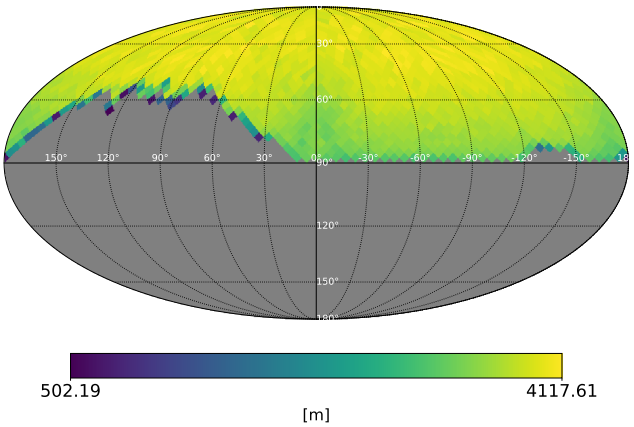

(a)

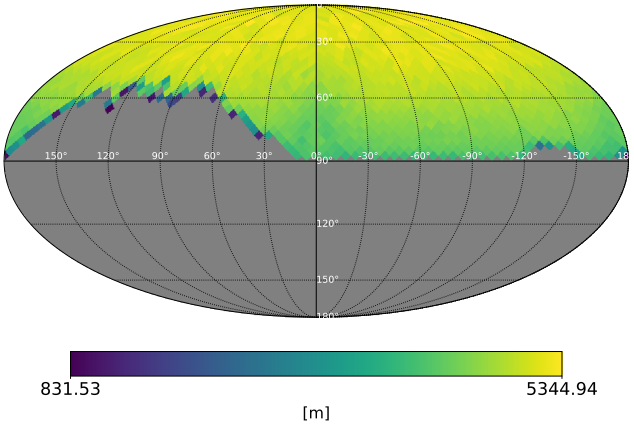

(b)

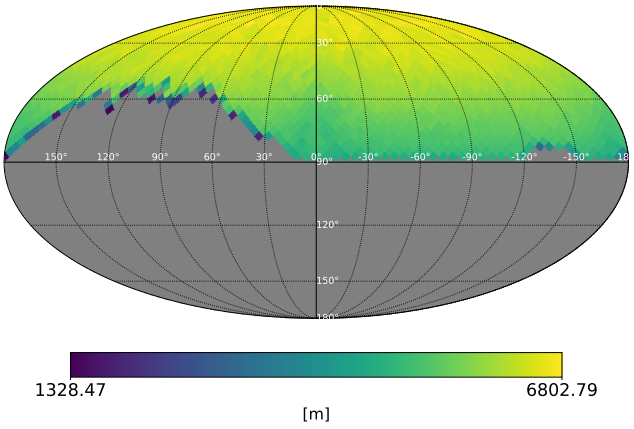

(c)

Fig. 6.9: The maximum distance for a TGF emitting a powerlaw spectrum. The plots show the maximum distance for several assumed source luminosities of (a) $L_{\mathrm{min}} = 10^{18}\,\mathrm{ph\,s^{-1}}$, (b) $L_{\mathrm{min}} = 10^{19}\,\mathrm{ph\,s^{-1}}$, and (c) $L_{\mathrm{min}} = 10^{20}\,\mathrm{ph\,s^{-1}}$ and assume a minimum of $N_{\mathrm{min}} = 60$ photons to be detected during a TGF with a duration of t=1 ms

7 Fermi GBM TGF analysis

The assumption for the previous simulations so far was either a source of monochromatic energy, a constant direction or isotropic simulations. These scenarios were used to gain insights about the detector behaviour and the Kugelalm response function but this simplification does not describe what happens in a thundercloud. To come closer to the realistic scenario we therefore want to figure out a realistic source behavior to simulate. To do so, we start with assuming that upward going and with satellites measured TGFs emit the same signal downwards. There are datasets for Fermi GBM found at [Fermi GBM] which we used to analyse this.
The Fermi GBM is a scientific instrument onboard the Fermi Gamma-ray Space Telescope. It is an international collaboration between the National Aeronautics and Space Administration (NASA) and the Max-Planck Institute for Extraterrestrial Phyiscs (MPE) and was launched on June 11, 2008 [Meegan et al., 2009]. The GBM is designed to monitor the entire unocculted sky and detect photons in the energy range of 8 keV up to 40 MeV. For measurements, two types of scintillators are utilized: It consists of 12 NaI detectors which are sensitive to low energies from 8 keV to 1 MeV and oriented at different angles to determine the direction of arrival of signals. 2 mounted BGO detectors cover the high-energy range from 200 keV to 40 MeV Thompson and Wilson-Hodge [2022]. As soon as the on-board software detects a statistically significant increase in count rates in two or more NaI detectors, the instrument triggers.
The GBM provides several types of data: Time-Tagged Events (TTEs) which provide the highest presicion with 2μs time resolution and CSPEC/CTIME which are binned data types and used for energy analysis [Meegan et al., 2009]. Between July 2008 and July 2016, the first Fermi-GBM TGF Catalog was created, including 4135 measured TGFs. Since the GBM itself can localize bursts to within several degrees, VLF radioassociation from external networks like WWLLN are often used to pinpoint TGF locations. Therefore, the dataset size usable for this work reduces to 1544 TGFs [Fermi GBM]. Fermi is operating in a low-Earth orbit at an altitude of approximately 565 km and an inclination of 25.6 – 26.5 degrees [Roberts et al., 2018]. To make conclusions

about measured TGFs it is necessary to know the location of Fermi at the time of the TGF to determine the location where Fermi 'sees' the TGF signal. To perform this analysis the WWLLN association table from [Fermi GBM] is chosen. For spectral analysis, the TGFs surpassing 110 observed counts are chosen since the SNR is >10 for these events, ensuring a clear differentiation from the background. The SNR is calculated through Equation (6.6). For the temporal analysis, TGFs with a duration >1 ms were chosen. The reason for that is to ensure enough counts per bin even after dividing it into intervals. For shorter TGFs the number of counts per bin decreases, making the analysis more difficult due to the background contribution.

7.1 Spectral analysis

The spectal analysis of TGFs using the 3ML framework follows a multi-step procedure. The initial stage involves loading the TTE as well as the CSPEC and the response files.

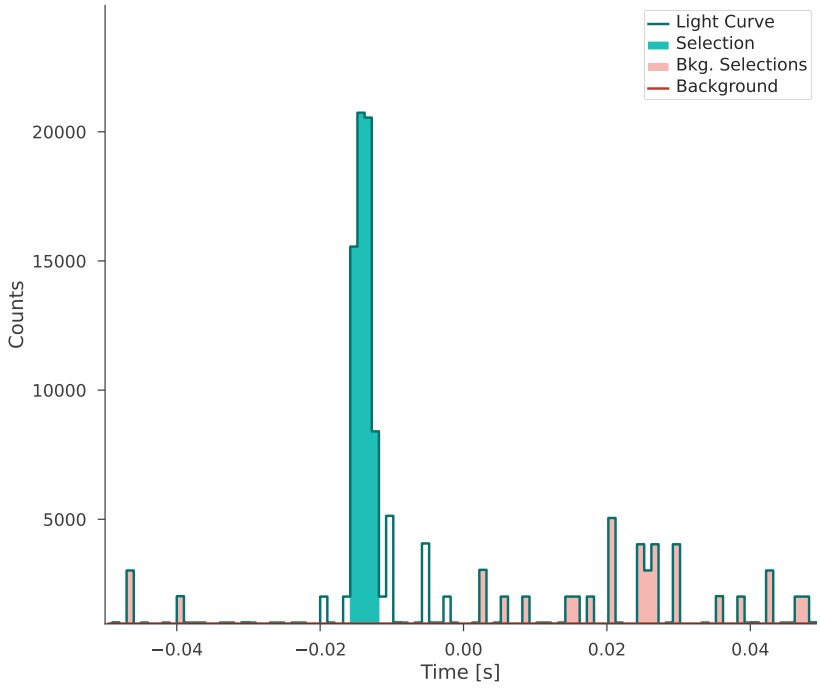

Fig. 7.1: Temporal evolution and interval selection for TGF090813215 from the Fermi catalog, measured by a NaI detector. The histogram displays the counts over time, with the main TGF signal highlighted in green. Shaded pink regions indicate the background selection intervals. An energy range of 10 keV to 40 MeV is used. The intense peak between -0.02 s and -0.01 s corresponds to the millisecond-scale flash analyzed in the time-resolved spectral evolution

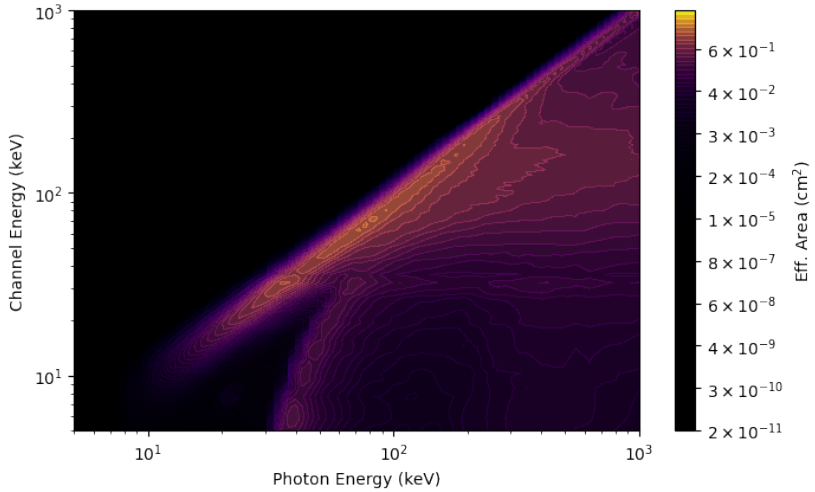

Fig. 7.2: Detector response matrix of Fermi GBM. The diagonal edge which contains the majority of the effective area is the photopeak. A lot of off-diagonal elements are contained because this plot was made for a very large source angle. Taken from [Fermi GBM DRM].

The TTE files are used for individual photon detection with time stamps, the CSPEC files provide the binned spectra over time and the response files describe the detector response. With these files the lightcurve is generated to identify the source and background intervals. For this study we utilized data from 3 specific detectors, two NaI and one BGO, that were oriented towards Earth at the time of the trigger. The source and background intervals of the signals measured by these detectors were manually defined by inspecting the lightcurves of these detectors, as illustrated in Fig. 7.1.
Once the intervals are defined, 3ML generates 'SpectrumLike' objects. These objects summarize the observed counts in the source interval as well as the estimated background and the intrumental repsonse matrix. The interaction between the incident flux and the detector is modeled by the convolution of the theoretical spectral model f(E), with the Detector Response Matrix (DRM) R. For the Fermi GBM, these matrices are well-defined and provided as standard calibration products. A DRM of Fermi is visualized in Fig. 7.2. They are precalculated using extensive GEANT4 simulations of the spacecraft and instrument geometry to account for the effective area, energy dispersion, and angular sensitivity of each detector. This relationship is expressed as:

$$d(E_\mathrm{i}) = \underbrace{\Delta T}_{[\Delta T]=s} \int_{E_\mathrm{i1}}^{E_\mathrm{i2}} \underbrace{dE_\mathrm{i}}_{[E_\mathrm{i}]=keV} \underbrace{R(E_\mathrm{i}, E_\mathrm{f})}_{[R]=cm^2} \cdot \underbrace{f(E_\mathrm{f})}_{[f]=\frac{\mathrm{ph}}{\mathrm{keV\,s\,cm^2}}} \tag{7.1}$$

where the response function $R(E_\mathrm{i}, E_\mathrm{f})$ maps the true photon energy E_f to the instrumentally recorded energy E_i. Unlike a photon spectrum the data is shown in 'detector space', namely counts vs. energy bins. This is essential because an instrument does not measure the physical photon flux directly but instead the incoming photons undergo a series of physical interactions within the detector crystal, as the ones seen in Fig. 3.8.
For the analysis of the measured spectra, several spectral models were compared, including a powerlaw, a cutoff powerlaw, and a Band function [Yassine et al., 2020]. The actual analysis was performed using Bayesian analysis with the EMCEE sampler. The EMCEE software package is an ensemble Markov Chain Monte Carlo (MCMC) sampler which was used for fitting the model [Foreman-Mackey et al., 2019]. This approach ensures a dense sampling of the high-likelihood regions, allowing for precise quantification of parameter uncertainties. Our analysis indicates that a simple power law is sufficient to describe the data since more complex models led to siginificantly larger parameter uncertainties without a corresponding improvement in the fit quality. The TGFs can be described through

$$F(E) = K \cdot \left(\frac{E}{E_\mathrm{piv}} \right)^{\lambda} \tag{7.2}$$

where K is the normalization factor and λ describes the spectral index. After converging on the median posterior parameters, the resulting model was compared to the raw data, which is shown in Fig. 7.3. The visualization in the given plot represents the final stage of the spectral fitting process. The cross-markers represent the observed counts and the resulting predicted count rates are represented as a histogram to reflect the discretization of the data into energy bins, allowing for a direct statistical comparison with the instrumentally recorded counts.
The lower panel in Fig. 7.3 displays the residuals, which quantify the deviation between the data and the model in units of standard deviation. The fact that the residuals for all three detectors fluctuate randomly around the zero-line and remain largely within the $\pm 1.5\sigma$ range confirms that the power-law model, after accounting for the complex detector respone, provides a physically and statistically consistent description of the TGF spectrum over the entire energy range from 10 keV to 10 MeV. This modeling approach, demonstrated above for a single event, serves as the methodological basis for our analysis. When applying the standardized spectral fitting procedure to every TGF in our sample, we can move from characterization of individual events to a comprehensive statistical description of a TGF population.
By utilizing the full dataset with the previously mentioned selection criteria, we performed a systematic analysis of 70 individual TGFs to determine the distribution of their spectral parameters. The resulting distribution for the spectral index and the

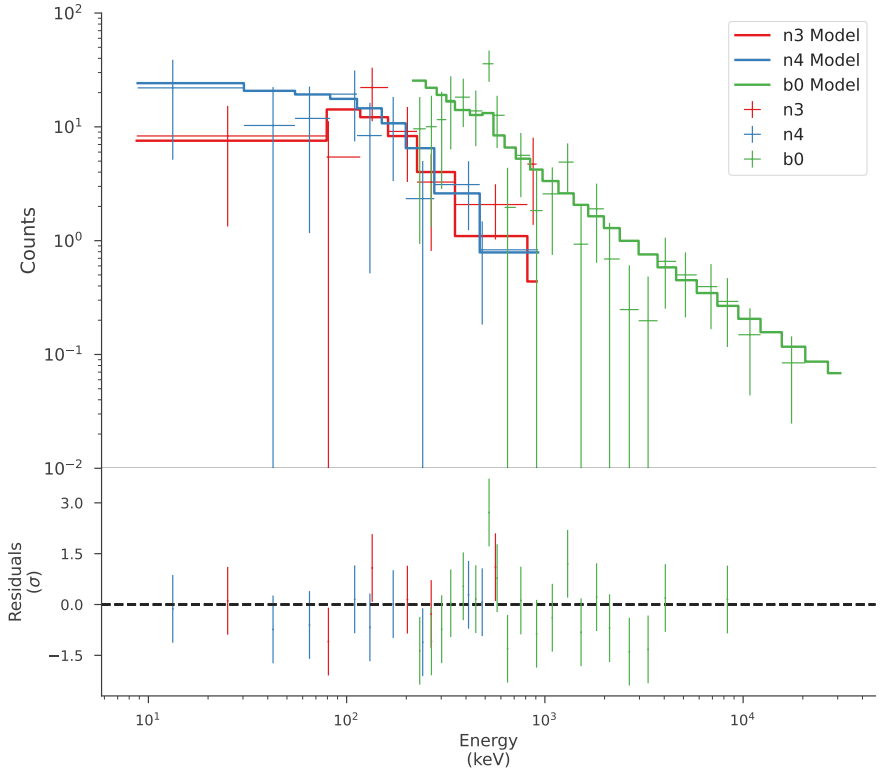

Fig. 7.3: Spectral fit of TGF090813215 from the Fermi GBM catalog using 3ML analysis. The upper panel displays the count spectra for used detctors (crosses) alongside their respective power-law model fits (solid lines). The energy range spans from 10 keV to 40 MeV. The lower panel shows the residuals in units of standard deviation, indicating a good agreement between the data and the input powerlaw.

hardness ratio are presented in Fig. 7.4. The statistical analysis calculates an average spectral index of -1.075±0.023 and an average K of $127 \pm 32\,\mathrm{keV}^{-1}\,\mathrm{s}^{-1}\,\mathrm{cm}^{-2}$. The index distribution is roughly unimodal and symmetric with 73% of the values being concentrated between -1.2 and -0.8. Using the determined parameters for each TGF, we calculated the hardness ratios for every TGF to characterize the spectral energy distribution. The hardness ratio is defined as

$$HR = \frac{\int_{E_2}^{E_3} dE\, F(E)}{\int_{E_0}^{E_1} dE\, F(E)} \tag{7.3}$$

where F(E) represents the power-law model with a pivot energy of $E_{\mathrm{piv}} = 100\,\mathrm{keV}$. The boundaries of the soft band are assumed as $(E_0, E_1) = (100\ \mathrm{keV}, 300\ \mathrm{keV})$ and the boundaries of the hard band as $(E_2, E_3) = (300\ \mathrm{keV}, 10000\ \mathrm{keV})$ since these boundaries are commonly used. The hardness ratio values are broadly distributed between 0.8 and 6.3. To further analyze the connections between parameters the hardness ratio

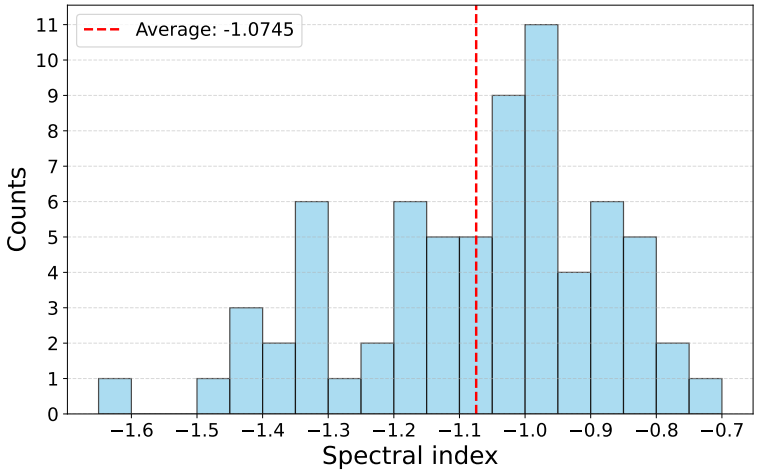

(a) Distribution of the powerlaw index values. Each histogram bin shows the number of TGFs with a spectral index in the respective range.

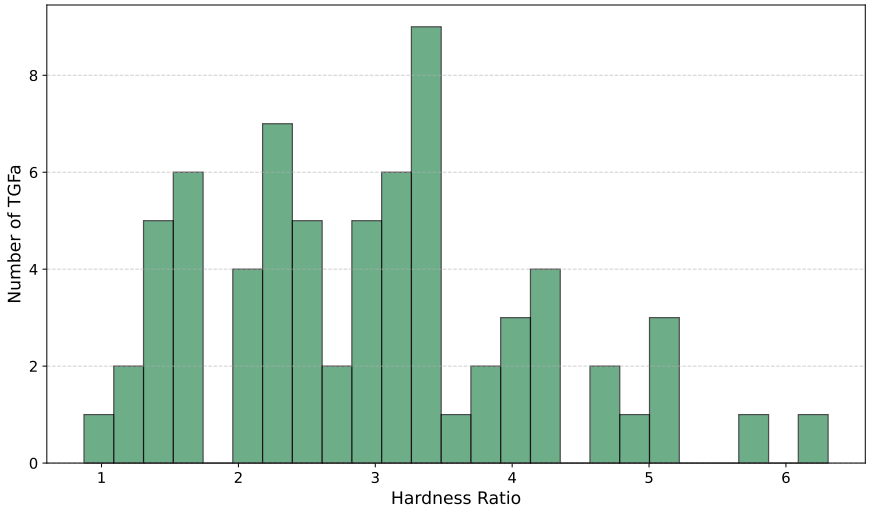

(b) Distribution of the hardness ratio. Each histogram bin shows the number of TGFs with a hardness ratio in the respective range.

Fig. 7.4: The statistical parameter distributions for the power law index (a) and the hardness ratios (b) after analyzing and averaging over 70 TGFs from the Fermi catalog. The dashed red lines show the average values of the used dataset.

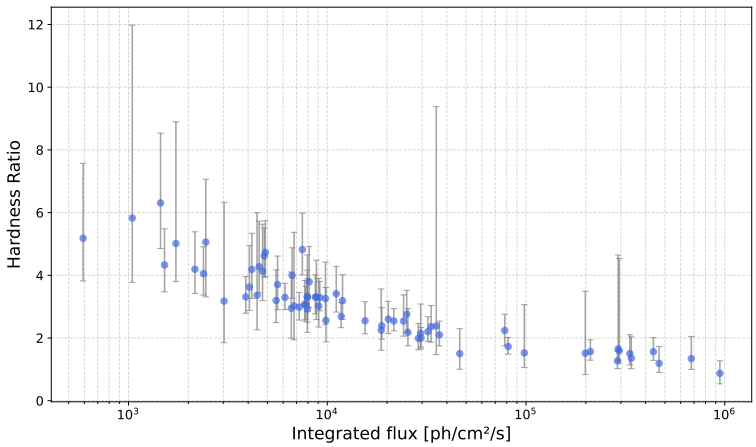

(a)

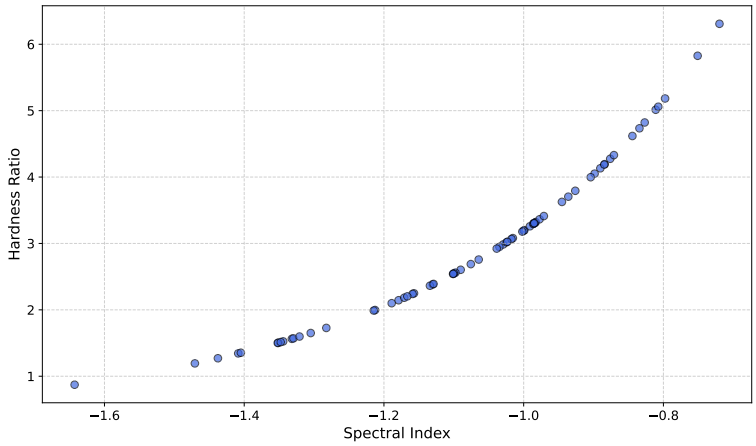

(b)

Fig. 7.5: (a) Hardness ratio plotted over the integrated flux from 10 keV – 10 MeV and (b) hardness ratio plotted over the spectral index. When higher-energy photons are emitted, the spectral index is higher but the flux of these photons is lower compared to lower-energetic photons.

is plotted over the integrated flux from 10 keV – 10 MeV and over the spectral index. This is illustrated in Fig. 7.5.

Analysis of the spectral characteristica shows a strong dependence between hardness ratio and integrated flux or spectral index. Comparing the hardness ratio at different fluxes, it shows bigger uncertainties for fluxes at around $10^3\,\mathrm{ph\,cm^{-2}\,s^{-1}}$ compared to higher fluxes. The reason for this is the lower photon statistics since less photons are emitted. The hardness ratio is the highest for fluxes in this range with a maximum value of 6.3. For increasing flux the spectrum starts to soften which is shown through a stabilized hardness ratio at around 1. For higher fluxes in the range of $10^5 - 10^6\,\mathrm{ph\,cm^{-2}\,s^{-1}}$ the uncertainties strongly decrease since more photons are part of the statistics which increases the accuracy. This shows that for a hard spectrum rather fewer high-energy

photons are emitted. For a softening of the spectrum, more photons are emitted by the TGF.
Beside of the integrated flux, the spectral index shows a non-linear correlation with the hardness ratio. For a spectral index of around -1.64 which corresponds to a hardness ratio < 1 an increase is visible, resulting in a hardness ratio of 6.3 for a spectral index of about -0.72. Since the data points are oriented along a well-defined curve, the mathiematical correlation between the hardness ratio and the spectral index is shown.
To validate our findings, we calculated the total luminosity using the derived parameters. We assume that the signal measured by Fermi GBM is not just emitted upwards but also downwards, which can then be detected at ground-based stations. To calculate the luminosity, we assume a source distance of $d = 15\,\mathrm{km}$ since thunderclouds appear at an altitude between 15 km and 21 km:

$$L = 4\pi\, d^2 \int_{E_{\min}}^{E_{\max}} dE E\, K \left(\frac{E}{E_{\mathrm{piv}}}\right)^{\lambda} \tag{7.4}$$

The resulting luminosity of $2.304 \times 10^{18}\,\mathrm{phs}^{-1}$ is within the same order of magnitude as the theoretical assumption of $10^{19}\,\mathrm{phs}^{-1}$ which is a common approximation in literature. Although our determined value is slightly lower than the initial assumption, it confirms that our parameter estimates are physically plausible within the context of TGF energetic models.
When a TGF happens, an estimated amount of $10^{19}\,\mathrm{ph\,s}^{-1}$ are emitted. Given a duration of 1 ms, this results in a total number of 10^{16} photons originating from one TGF. The upward moving component of the TGF, which was previously measured by satellite-based measurements like Fermi-GBM, encounters increasingly thinner atmospheric layers and can be detected with minimal attenuation. The downward-directed component needs to traverse the more dense atmospheric layers near the Earth's surface which is why the attenuation of this signal plays a crucial role. This attenuation is energy-dependent, which makes it a big challenge to detect since the air acts as an absorber for low-energy photons. While the transmissivity between 0 keV up to a few 100 keV is basically zero as seen in Fig. 3.11, it increases progressively for energies in the MeV energy range. This transmissivity changes not only with the distance but also with the input angle of the TGF photons. Consequently, only a fraction of the flux can be measured at the Kugelalm. When the photons traversed the atmosphere the last thing which needs to be taken into account is the local detector environment and the detector response. Since the detector is shielded this has a big effect on the detection efficiency, which is determined by the effective area of the detector. By integrating the

filtered flux, the statitical expectation is drastically reduced, depending on the distance of the TGF source. To gain better understandings of the spectra which are measureable for different distances, simulations with a powerlaw emitted by the TGF source were performed.

Due to computational reasons, a simulation with a flux of $10^5\,\mathrm{ph\,cm^{-2}\,s^{-1}}$ was performed with a duration of 1 ms and a powerlaw with the spectral index given above λ = -1.07444019 between 100 keV – 10 MeV. With this input flux the luminosity of the source can be calculated with

$$L_{\mathrm{sim}} = 4\pi \cdot d^2 \cdot F \tag{7.5}$$

where d describes the distance between the source and the detector. The flux for different distances are summarized in Tab. 7.1. By dividing through the bin width, the resulting spectrum shows the counts per keV and per second of a photon to be detected in this energy range. Another important thing to mention is the scaling factor. Since the flux of simulated photons changes with distance we need to calculate a different scaling factor for each distance to scale the simulated scenario up. The reason why we need to scale it up is that we want to get the source luminosity of $10^{19}\,\mathrm{ph\,s^{-1}}$. This procedure leaves out the atmospheric transmission probability, so we need to take this into account to receive the final measureable spectrum of the count rate. The scaling factor was calculated using $L = \alpha \cdot L_{\mathrm{sim}}$ where α is the scaling factor and L is the assumed source luminosity. To calculate the number of photons per $\mathrm{cm^{-2}}$ the number of simulated particles L_{sim} then needs to be divided through the starting area, which is determined by the system to $A_{\mathrm{start}} = 1.9635 \cdot 10^7\,\mathrm{cm^{-2}}$. The resulting numbers for the scaling factor, the number of detectable photons and the photons per $\mathrm{cm^{-2}}$ emitted are summarized in Tab. 7.1. Since transmission probability is energy-dependent, we need to calculate the transmission probability for each energy bin. Having a zenith input

Distance [m]	$L_{\mathrm{simulated}}$ [$\mathrm{ph\,s^{-1}}$]	Scaling factor	Number of photons	Photons $\mathrm{cm^{-2}}$
500	3.1816×10^{15}	3.1831×10^{3}	3.93×10^{7}	1.6×10^{8}
1000	1.2566×10^{16}	7.9580×10^{2}	2.46×10^{6}	6.4×10^{8}
2000	5.0265×10^{16}	1.9895×10^{2}	7.99×10^{4}	2.6×10^{9}
5000	3.1416×10^{17}	3.1831×10^{1}	1.74×10^{2}	1.6×10^{10}
10000	1.2566×10^{18}	7.9580	6.21×10^{-1}	6.4×10^{10}

Table 7.1: Scaling factor, flux of simulated particles in $\mathrm{ph\,s^{-1}}$, the number of detected photons and the emitted photons per $\mathrm{cm^{-2}}$ for different distances. These parameters need to be included to scale the simulated scenario to the scenario of an assumed flux of $10^{19}\mathrm{ph\,s^{-1}}$.

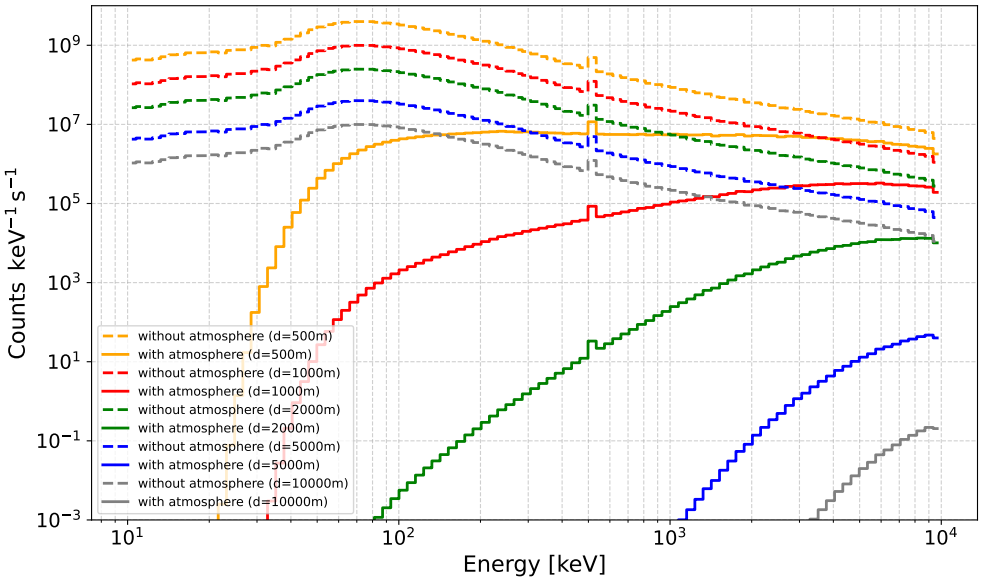

Fig. 7.6: Simulated powerlaw spectra for several distances. The spectra are calculated for including the atmospheric attenuation and leaving it out. The increase in distance is reflected in the spectrum: for distances around 500 m low-energy photons are detected while for distances around 5 km the low-energy photons get absorbed.

direction, Equation (6.4) takes the form

$$T_{\text{atm}}(E, d) = \exp\left(-\mu(E) \cdot 7.617276 \cdot 10^2 \left(1 - \exp\left(-1.176471 \cdot 10^{-4} \cdot d\right)\right)\right) \tag{7.6}$$

By multiplying every energy bin with the corresponding transmissivity the attenuation effects of atmosphere and detector environment are taken into account. The resulting spectra for different distances between detector and TGF source and with or without absorbing atmosphere are visualized in Fig. 7.6. In the scenarios excluding the atmosphere, the counts decrease consistently at higher input energies. This behavior shows the underlying power-law distribution of the source spectrum, resulting in fewer high-energy photons being emitted. A detection peak is observed in the energy range between 70 and 80 keV. Since a part of the high-energy photons undergoes scattering and loses energy, the peak of the detected energy distribution remains below 100 keV. The spectral shape remains identical across all distances when the atmosphere is not considered. A vertical shift of the curves occurs for the different distances. This shift is due to the different scaling factors applied for each distance, corresponding to the geometric attenuation of intensity. A prominent feature in these cases is the peak at the 511 keV line.

When atmospheric transmissivity is taken into account, the spectra show a steeper in-

crease, particularly at shorter distances. At the shortest distance between the detector and the TGF source for $d = 500\,\text{m}$, detections begin at approximately 20 keV and increase sharply until roughly 70 keV. From that energy on, the rate remains relatively stable but shows a slight downward trend toward higher energies. With increasing distance, the slope of the initial rise decreases, while the threshold energy at which photons are detected shifts to higher values. As the thickness of the atmospheric layers increases with distance, low-energy photons are absorbed before reaching the detector, which explains the shift in the detection threshold. Up to a distance of 2000 m, the 511 keV line remains recognizable as a dominant peak. For distances in the range of 500 – 1000 m the detectec counts are at the order of magnitude $10^6 - 10^7$. At even greater distances of up to 5 – 10 km, barely more than 200 photons are detected with a number of detectable photons of 0.6 for a distance of 10 km. The photons measured at these energy ranges primarily possess energies of several MeV, while photons with energies below 1 MeV are entirely absorbed by the atmosphere.

7.2 Temporal analysis

Besides the spectral analysis we also performed a temporal analysis of the given TGFs. To do so, the decisive criterion was not just the detected counts anymore, we also needed to take into account the duration of the TGFs. Since the minimum time resolution limited by the data is 1 ms we selected the TGFs with a duration > 1ms.
To investigate the spectral evolution of TGFs over time, a robust method for splitting the lightcurve into statistically significant intervals is required. For this procedure the detector with the brightest lightcurve or the best signal serves as a basis for determining the intervals. These time intervals defined by the reference detector are then mapped to all other active detectors. This ensures that the spectral data from all detectors corresponds to the exact same physical state of the TGF. With this, 3ML generates a new set of plugins for each time bin. Each bin plugin then contains the count data and the appropriate instrument for that specific moment – from each active detector. The notebook then performs the fitting: First, a spectral model is identified. The algorithm then loads the synchronised data from all detectors and runs a fit to adapt the model to the data. The resulting parameters are then stored and visualized [Burst analysis].
This procedure allows for an independent Bayesian spectral fit for each time slice, meaning that the abovementioned Bayesian analysis with the EMCEE sampler is performed

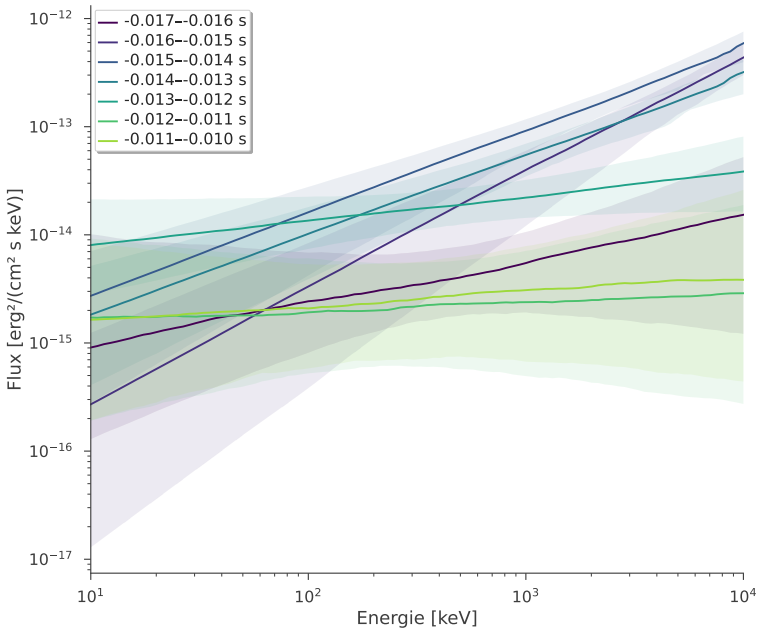

Fig. 7.7: Time-resolved energy flux distribution ($E^2F(E)$ representation) for TGF090813215 taken from the Fermi catalog. The positive slope in this representation indicates a hard spectral index, confirming that the power output is dominated by high-energy emission in the MeV range. The flux is well-constrained during the peak signal (-0.016 s to -0.013 s), while the larger uncertainty bands in the pre- and post-peak intervals reflect the decrease in the signal-to-noise ratio.

for each time bin plugin. This enables us to track the evolution of the flux and accordingly the evolution of the powerlaw parameters throughout the duration of one event. By utilizing this adaptive segmentation we can move beyond time-integrated properties and resolve whether the TGF exhibits spectral hardening or softening during its millisecond-scale lifetime. The resulting time evolution for a single TGF is shown in Fig. 7.7. The time-resolved energy flux distribution is presented here in the $E^2\,F(E)$ representation to illustrate the spectral evolution of the TGF across consecutive temporal intervals. While a standard photon spectrum F(E) emphasizes the total number of photons, the $E^2\,F(E)$ visualization shifts the focus to the power distribution. This approach identifies the specific energy range where the bulk of the power is emitted, offering a more direct view of the event's energetics. Consequently, this representation allows for a clearer analysis of the physical processes driving the TGF and how the dominant energy output shifts over time. The different parameters for each time interval are visualized in Tab. 7.2.

The observed positive slopes of the flux functions on the log-log scale corresponds to a rather hard power law spectrum. In this representation, an increasing line indicates

Interval [s]	K [$\mathrm{keV^{-1}\,cm^{-2}\,s^{-1}}$]	λ	Flux [$\times 10^2\,\mathrm{ph\,cm^{-2}\,s^{-1}}$]	HR
-0.017 – -0.016	0.08117	-0.648	1.064	3.49
-0.016 – -0.015	0.003359	-0.128	0.2131	21.34
-0.015 – -0.014	0.04908	-0.327	1.602	10.627
-0.014 – -0.013	0.09164	-0.457	2.009	6.783
-0.013 – -0.012	12.19	-1.088	7.727	0.761
-0.012 – -0.011	0.08214	-0.935	6.166	1.291
-0.011 – -0.010	0.497	-0.901	3.923	1.452

Table 7.2: Properties of the time-intervals from TGF090813215. The flux was integrated between 10 keV and 10 MeV. The hardness ratio was calculated using Equation (7.3).

that the energy flux is dominated by high-energy photons in the MeV range, which is a primary characteristics of Bremsstrahlung emission from relativistic electron avalanches as described previously. A clear distinction is visible between the intervals containing the TGF signal and the surrounding background. The signal intervals ranging from -0.016 s to -0.013 s exhibit a high, well-constrained flux progression. In contrast, intervals preceding and following the flash like -0.011 s to -0.010 s show a significantly lower flux progression and large errors. The flux for the interval between -0.013 s and -0.012 s already shows a decreasing trend, which is also visible in the lightcurve plot Fig. 7.1 where the counts for this interval are significantly lower compared to the preceding peak intervals. Tab. 7.2 shows a lower integrated flux for the time intervals -0.016 – -0.014 s, showing that the flux consists predominantely of high-energy photons.
The increased uncertainties in the time intervals which do not contribute to the TGF signal are a direct result of a lower signal-to-noise ratio. In these regions, the model is constrained by background fluctuations rather than a dominant source signal. The non-signal intervals are plotted to show the decay of the TGF signal. The plot enables the tracking of subtle spectral changes throughout the duration of the event. Variations in the slope and amplitude between individual time slices suggest a dynamic acceleration process. A noticeable flattening of the slope toward the end of the burst indicates spectral softening, a common feature in high-energy transients that reflects the decaying energy of the particle accelerator. Finally, the fact that the energy flux at energies above 1 MeV is substantially higher than in the 100 keV range for the TGF signal intervals provides a visual validation of the previously calculated hardness ratio. The hardness ratio increases to 21.38 with the beginning of the source interval, reaching 6.783 towards the end of the source interval. Subsequently, it remains in the range of 1.2 – 1.5. This confirms that the emission during the TGF is significantly biased toward high-energy photons, as expected from theoretical models.

8 Natural Radioactivity

To assess the contribution of natural background radiation to the experimental setup shown in Fig. 5.3, the decay chains of ^{238}U, ^{235}U, ^{232}Th and the isotope ^{40}K were simulated. The emission was modeled from the outer 30 cm layer of the concrete platforms, assuming all daughter isotopes in the respective chains are present. The source volume was limited to the outer 30 cm of the concrete, as photons originating from deeper layers are effectively absorbed by the material before reaching the detector. A simulation time of 1 ms was utilized for each run, making it comparable to the measured TGF signal which was assumed to have a length of 1 ms.
The resulting spectra of the isotopes ^{238}U, ^{235}U, ^{232}Th and ^{40}K are presented in Fig. 8.1. For the case of not taking into account the atmospheric transmissivity the natural radioactivity background can be neglected since the signal is four orders of magnitude weaker. The situation changes for the realistic measureable TGF spectrum which includes atmospheric transmissivity. It strongly depends on the distance between TGF source and detector. For shorter distances in the range of a few hundred meters, the TGF signal is significantly higher than the background noise. By further increasing the distance to 1 – 2 km the natural radioactivity becomes more important and can no longer be negelcted. The reason for this is the increased threshold energy of the detector after atmospheric interaction. Since the natural radioactivity originates from concrete which is in immediate vicinity to the detector, the background radiation is not affected by atmospheric transmission. Consequently, while the TGF signal is weakened by the distance, the background remains the same. This results in an increased importance of the natural background since the TGF signal has fewer counts. For even higher distances of about 5 km the natural radioactivity is the source of detected energies in the range of up to 1 MeV.

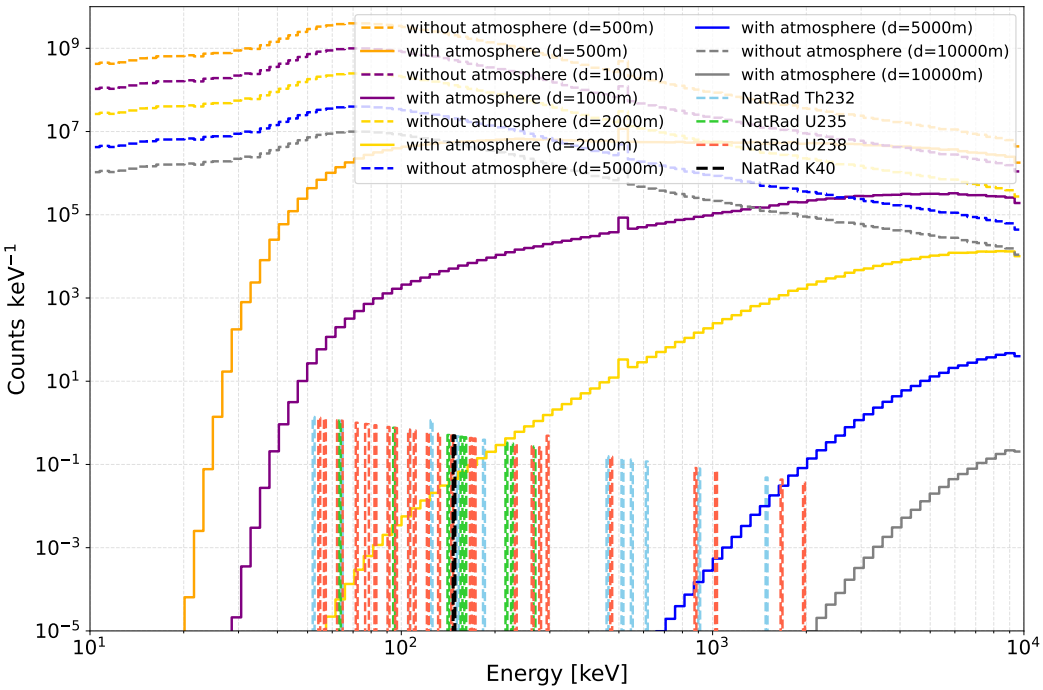

Fig. 8.1: Simulated spectra for powerlaw simulations with and without taking account the atmospheric transmissivity. The simulated γ-ray lines are included. the powerlaw simulations as well as the background simulations were performed for a suration of 1 ms.

9 Discussion

This study evaluated the detectability of TGFs at the UFS by performing various simulations and calculating key detection parameters. For existing measurements, a TGF luminosity of $10^{19}\,\mathrm{ph\,s^{-1}}$ and a duration of 1 ms are widely accepted assumptions. For comparison, Chaffin et al. [2024] assumes a range from 10^{16} to over $10^{18}\,\mathrm{ph\,s^{-1}}$, while Ursi [2021] utilizes $10^{18}\,\mathrm{ph\,s^{-1}}$. The duration estimated and measured by Wada et al. [2019b] is 1 ms, which is in excellent agreement with the values used in this work. To account for a broader range of scenarios, the maximum distance at which a TGF remains detectable was calculated for different luminosities. In this work the maximum distance is evaluated for a minimum number of 60 photons to arrive at the detector. This threshold for the minimum number of detectable photons is consistent with the methodology chosen by Ursi [2021]. While Ursi [2021] also performed GEANT4 simulations, they utilized a power law with a high-energy cutoff at 6.6 MeV, whereas this work used a standard power law. Their analysis utilized an effective area of $10\,\mathrm{cm^{-2}}$, which compares well to the maximum effective area of approximately $13\,\mathrm{cm^{-2}}$ determined in our case.The maximum detection distances calculated in this work were (4117, 5344, 6802) m for luminosities of $(10^{18}, 10^{19}, 10^{20})\mathrm{ph\,s^{-1}}$, respectively. These values are slightly higher than the TGF altitude of 2500 ± 500 m determined by Wada et al. [2019b]. It should be noted that Wada et al. [2019b] conducted their measurements at sea level and were thus not limited by mountainous terrain like in our case. Similar results were achieved by Ursi [2021], who calculated a maximum vertical distance of approximately 4 km and a horizontal distance of about 10 km under similar initial conditions. The spatial characterization of TGFs could be further enhanced by implementing a stereo observation network, a method which was successfully employed by Wada et al. [2019b]. By utilizing a dataset of TGFs measured with Fermi GBM we calculated the number of photons detected for TGFs originating at several distances. For distances in the range of 500 – 1000 m there are $10^6 - 10^7$ detected photons. While the number is quite large for lower distances it decreases to 174 photons at 5 km distance and 0.621 photons for a distance of 10 km. This leads to a distance in which 60 photons can be measured in

the range of 5500 – 6500 m. This is in good consistency with the range determined by Ursi [2021] as well as the range of maximum distances calculated from the simulations performed in this work.

For measurements of TGFs, Wada et al. [2019b] utilized networks of detectors spaced 1 – 5 km apart. This multi-detector approach allows for the simultaneous capture of γ-ray signals at different position. This enables a precise location of the TGF position and the analysis of the TGF source geometry as well as the correlation with lightning leader propagation. Since the UFS is located in a mountainous region it is difficult to develop a detector approach. It could be possible to mount detectors on nearby summits close to the UFS which would increase the measurement precision and detection area. Beside of the combination of several detectors, Hongbo et al. [2019a] used a different approach. By combining high-sensitivity magnetic sensors with γ-ray detectors this combination provides a possibility to validate TGF events. By utilizing multi-station magnetic recordings, Hongbo et al. [2019a] were able to correlate lightning waveforms directly with the impulsive γ-ray emission.

In their work, Ursi [2021] estimated a number of $10^4 - 10^7$ photons to be measured for horizontal distances below 1 km and vertical distances below 4.5 km. After comparing with the numbers calculated in this thesis, these estimates are highly reasonable when compared to our simulated values, which yielded $10^4 - 10^7$ photons for distances up to 2 km. Regarding energy spectra, this work assumed energies ranging from 100 keV to 10 MeV. This is in good agreement with Chaffin et al. [2024], who measured TGFs in the 100 keV to 9 MeV range. However, Wada et al. [2019b] noted that TGF energies typically cluster around 10 MeV but can extend up to 20 MeV. As our current simulations are capped at 10 MeV, expanding the energy range in future analyses could be beneficial, particularly since low-energy partitions are often nonexistent at higher altitudes.

The simulated flux in this study was calculated to be between $1.6 \times 10^8 - 6.4 \times 10^{10}\,\mathrm{ph\,cm^{-2}}$ for varying distances between 500 m – 10 km. Experimentally, Wada et al. [2019b] determined an on-ground fluence of $4 \times 10^5\,\mathrm{ph\,cm^{-2}}$ at the TGF center and $7.3 \times 10^3\,\mathrm{ph\,cm^{-2}}$ at a 1 km offset. They concluded that their detectors were saturated and estimated the actual flux to be 4 to 5 orders of magnitude higher. This corrected estimate coincides well with our simulated flux for the chosen distances. Finally, based on the calculated maximum distances, we estimated the frequency of measurable events. Given the propagation of these distances, we expect between around 63 monthly thunderstorm hours for a luminosity of $10^{19}\,\mathrm{ph\,s^{-1}}$, totaling in 756 hours per year. Ursi [2021] calculated bwetween 60 and 730 expected flashes which shows the comparability of our study. Assuming a TGF-to-flash ratio of $10^{-3} - 10^{-2}$ similar to Ursi [2021], we

can expect up to 8 measurable TGFs per year at the UFS.
Despite the consistency of our results with existing literature, this work faces several limitations. The energy spectrum in our simulations was capped at 10 MeV. Since downward TGFs can exhibit energies up to 20 MeV or higher as mentioned by Wada et al. [2019b], the simulation might underestimate the flux at larger distances due to the lower attenuation of high-energy photons. Also, this study assumes a simplified beam geometry. As explained in Ursi [2021], the beam geometry and the halfangle can vary which has strong influence on the detectability. In reality, these variations in the beam opening angle and source orientation could lead to significant fluctuations in the number of arriving photons. Another limitation is the detector itself. As described by Wada et al. [2019b], saturation may happen at such events. While our flux estimates for close-range events are high these instrumental limitations could constrain the measurable data quality of very bright, nearby flashes. What could also be improved is the single-detector setup. Relying on a single measurement setup without coinciding radio-frequency observations as done by Hongbo et al. [2019a] or Wada et al. [2019b] makes it challenging doing precise localisation meausrements.

10 Summary

This thesis investigates the detection potential and physical charcteristics of TGFs from a ground-based perspective. TGFs are intense sub-millisecond bursts of high-energy radiation produced within thunderstorms. While these phenomena are primarily studied via satellite observation, this research focuses on their detectability provided by the research station UFS, located at an altitude of 2650 meters at the Zugspitze mountainside. By utilizing this high-altitude ground-based station, the study aims to mitigate the effects of atmospheric attenuation that typically prevents the observation of these events at lower elevations. Other effects, appearing in the mountainside like topographical limitations and natural radioactivity background are also included and analysed.
The theoretical foundation of this work describes the mechanisms of particle acceleration in the atmosphere, specifically focusing on the RREA model and the RFM. These processes explain how strong electric fields within thunderclouds can accelerate the seed electrons necessary for the creation of TGFs to relativistic speeds, leading to the emission of high-energy bremsstrahlung. This work analyses the spectral properties of these TGFs, noting that while TGFs exhibit hard energy spectra reaching several tens of MeV at their source, these spectra are significantly modified by Compton scattering as the photons propagate through the atmosphere.
A central component of this research involves detailed computational modeling using the GEANT4 based MEGAlib framework. The simulations and models accurately replicate the complex topography of the Zugspitze mountain range and the structural environment of the Kugelalm measurement hut, where the detector is located. By implementing Monte Carlo simulations, the study evaluates the performance of common detector materials such as NaI scintillators. It was found that out of the three materials NaI, Ge and BGO the BGO scintillator performs the best. With a maximum effective area of 15cm^2 the BGO detector has the highest effective area for an input angle of approximately $\theta = 60°$. This finding is consistent with the performed isotropic analysis. For several monochromatic sources of $\text{E} = (0.1,\ 1,\ 10)\,\text{MeV}$ the expected count distribution was calculated in which the most counts were detected for $\varphi = 90°$ and

$\theta = 60°$. These plots also show several features of the detector environment. While for energies E = 0.1 MeV the data points reflect the triangular shape of the Kugelalm, this effect fades away for increasing energies. A constant feature throughout all simulations is the angle configuration (φ, θ) which is blocked by the mountains.
This work evaluates the detector response for several monochromatic sources. For lower energies in the range of 0.1 – 1 MeV the photopeak and the Compton continuum are clearly visible. By further increase of the photon energy a significant peak at 511 keV occurs, originatin from pair production. Since the detector is located in the Kugelalm, the corresponding shielding effect by the Kugelalm roof is also visible. by comparing the two scenarios there are more low-energy counts when the detector is located inside the Kugelalm. Since the roof functions as a scatterer, more photons experience energetic and directional change and get detected after scattering. The corresponding total counts ratio for counts with and without including the Kugelalm steadily increases. While for photons energies of E = 0.1 MeV this ratio is approximately 0.6, it rises to 1.4 for photon energies of E = 10 MeV, making it more advantageous to place the detector inside the Kugelalm for high input energies. This enhancement at higher energies happens due to secondary scattering withing the structure. The detected spectrum is dependent on the input direction, which is shown. By comparing $(\varphi, \theta) = (0°, 0°)$ with a slightly tilted θ angle of $(\varphi, \theta) = (25°, -90°)$ it was shown that the Kugelalm geometry has an effect on the detection of TGFs. For the zenith direction the ratio of counts with vs without the Kugelalm was 1.2 for energies of E = 10 MeV instead of 1.4 for zenith direction. Beside of the shielding effect of the Kugelalm, the atmospheric transmission probability was calculated. This probability is strongly dependent on energy and input angle of the incoming photons. For a source altitude of 10 km when the detector is located on an altitude of 2657 m, the atmospheric transmission probability varies between 14 orders of magnitude. For photon energies E = 0.5 MeV the probability is on the order of 10^{-17} since a lot of the low-energy photons get absorbed. The probability further decreases for higher zenith angles due to the thicker atmospheric layer. High-energetic photons with E = 50 MeV have a probaility of 10^{-3} to reach the detector.
Using this transmissivity the maximum distance in which a TGF can be measured was calculated. The minimum number of photons to be detected for this claculation was chosen to be 60 which results in a SNR of 7.68 and is in good agreement with the literature and similar simulation setups. For monochromatic energies (0.1, 1, 10) MeV this distance was calculated to be (738, 1493, 3851) m. To gain a more reaslistic estimation the maximum distance for a powerlaw spectrum with spectral index -1 emitted by the TGF was calculated. The monochromatic simulations give a good estimation of the expected dimensions but does not describe a realistic TGF emission. To calculate this,

several luminosities of $(10^{18}, 10^{19}, 10^{20})\,\mathrm{ph\,s^{-1}}$ which cocincide with literature assumptions, were used. With this the maximum distance for a powerlaw is calculated to be (4117, 5344, 6802) m, respectively.
To make conclusions about the TGF detectability, the occurrence of TGFs was analyzed. To do so, a lower estimation was made by utilizing a monthly thunderstorm hours dataset. This dataset was averaged over 11 years. July has the most averaged thunderstorm hours with 228 so this month was chosen for further analysis. The monthly thunderstorm hours were then plotted over the radius so that a powerlaw fit can be performed. With the given maximum distance this results in a number of 432 – 1283 yearly thunderstorm hours with an average of 756 yearly thunderstorm hours for a source luminosity of $10^{19}\,\mathrm{ph\,s^{-1}}$.
To validate our finidings, TGFs measured with Fermi GBM were utlilized. We used a total of 70 TGFs, limited to >110 counts for spectral analysis and a duration of >1 ms for temporal analysis. For the spectral analysis, the 3ML framework and Bayesian analysis was applied to the TGF data. With this procedure the average spectral index could be determined to λ = -1.07444019 for energies between 100 keV and 10 MeV while the averaged normalization constant is $127 \pm 32\,\mathrm{keV^{-1}\,s^{-1}\,cm^{-2}}$. Knowing the averaged values the integrated fluxes as well as the hardness ratios were calculated. By visualizing the hardness ratio with the integrated flux and the index it was shown that the higher the spectral index the lower the hardness ratio. For high hardness ratio the integrated flux is lower, showing that the number of high-energy photons (with energies between 300 keV and 10 MeV) emitted is smaller compared to low-energy photons (with energies between 100 – 300 keV). For increasing flux the spectrum softens by emitting more low-energy photons. To validate the averaged powerlaw parameters, the resulting luminosity was determined. For a source in 15 km distance a luminosity of $2.304\times10^{18}\,\mathrm{ph\,s^{-1}}$ was calculated, being in agreement with the initial assumption of $10^{19}\,\mathrm{ph\,s^{-1}}$.
The powerlaw spectra for different source – detector distances were calculated for comparison with the calculated values. To do so, an initial luminosity is assumed and used to calculate the normalization factor K. By defining several intervals (100 – 500) keV, (500 – 1000) keV, (1000 – 5000) keV, (5000 – 10000) keV the partition of each interval to the overall flux was determined to use this as a weighting factor. By weighting the different intervals it was taken into account that some energy range might emit more photons than others. The resulting spectra were then visualized for the case of inluding the attenuation of the atmosphere and without this attenuation. For distances in the range of 500 – 1000 m the number of detected photons is in the range of $10^6 - 10^7$ with a threshold detection energy of 20 – 80 keV. For higher distances this threshold is

increasing since more photons get absorbed or scattered due to the thicker atmosphere. A distance of 5 km shows around 174 detectable photons with no significant detections below energies of 1 Mev. The number of photons detected at different source distances lets us approximate a distance at which 60 photons can be mesaured. This distance is evaluated to be in the range of 5500 – 6500 m which is in good comparison with the calculated maximum distance of 5344 m for a luminosity of $10^{19}\,\mathrm{ph\,s^{-1}}$.
The performed temporal analysis clearly shows the hard spectra of a TGF by evaluating the hardness ratio and spectral index for the whole TGF duration. When the signal starts, a hardness ratio of 21 is calculated which decreases to a stable hardness ratio of 1 at the end of the TGF signal. For a higher hardness ratio the spectral index decreases, indicating a hard spectrum. The spectral index increases to around -1 towards the end of the TGF signal.
The natural background was taken into account since the detector setup is surrounded by concrete which works as an emitter for natural radioactivity. The decays for the isotopes ^{238}U, ^{235}U, ^{232}Th, and ^{40}K were simulated for the given setup. Depending on the distance of the TGF source the natural background can be neglected. While for lower distances around 500 m the natural radioactivity is surpassed by the actual signal, for higher distances it plays a more significant role. Due to the attenuation of low-energy photons for increasing distance the natural rdioactivity can be detected at lower energies and needs to be taken into account.
This work successfully determines the distance for which a minimum number of photons emitted by a TGF can be detected. These results are compared and validated with other works, including a validation of TGF properties such as the hardness of the spectrum. The calculated values were specifically compared with existing TGFs measured by Fermi GBM by assuming that the upward part is also emitted downward. This comparison shows good consistency in the detectable distance for TGFs at the UFS. The measurement site was successfully implemented, accounting for features such as the shielding by the Kugelalm or the mountains for specific directions. The role of natural radioactivity present at the measurement site was also analyzed. Regarding the dataset, the averaged parameters were determined utilizing 70 TGFs. By using a larger dataset or including variations of several power-law indices, one might find different averaged spectral indices or see how the spectrum changes more broadly. Due to computational reasons, the energy limit in this work was set to 10 MeV. It is suggested that there is a high-energy component for TGFs by other works, which was not analyzed. Including higher-energy photons might change the detected spectrum and result in different parameters. While several detector materials were compared to see which performed best for specific configurations, the study did not include how detectability changes

with various detector shapes or internal detector properties like saturation or pileup. By varying the shape or including specific property effects, one might find the optimal configuration for detecting TGF photons. This work also focuses on single TGF pulses. Since it is reported that a TGF might contain multiple pulses, this could also be further analyzed. This could also have additional effects on the detector like the summation of several signals, which was not included in this work. No analysis of real lightning data was done which would get more insights in the probability of thunder happening at the UFS measurement site. To get a better estimation this could be analyzed.

11 Outlook

Building on this thesis, the most significant step for future work is the implementation of real-time measurements at the UFS. A spare BGO detector which is similar to those mounted on the Fermi satellite will be built specifically for these kind of measurements. The installation of this detector and corresponding detection of real-time data might take place in late 2026. This setup will then provide an opportunity to measure and record real-time TGF events close to Earths surface in this region. Similar measurements have already been done in Japan or Italy so this would be a possibility to compare measured TGFs under different conditions. These measurements can be used to analyze the simulations performed and developed in this work. By comparing simulated results with the actual measurement data, the simulation setup can be improved and validated. Future work should also focus on expanding the simulated energy range beyond 10 MeV. Since it was already suggested that there is a higher-energy component in TGFs, it is crucial to analyze these higher-energy parts. The analysis should include directional and spectral response of such signals to gain deeper understanding of the TGF production mechanisms. By evaluating the high-energy component of TGFs, the simulations and models used in this work can be improved. Also, TGFs measured with satelited-based instruments should be analzed in greater detail. The analysis of more TGF datasets will improve the statistics of the parameter distributions while making the model more precise. To specify the results, more instrumental factors can be taken into account. Utilizing the real BGO detector will allow for a more detailed analysis of how environmental factors like seasonal snow or rain affect the signal. Analyzing real-time measurements over a long period of time will show the seasonal effects and can give insights in when TGF measurement occur most frequently.
To further enhance the detection and localization of TGFs, the installation of a detetor network or the installation of different detectors can be a topic of future work. The installation of different kinds of detectors allows the measurement of several TGF features. Not just the TGF signal but also radio signatures coinciding with TGFs and lightning discharges could be measured. This would be a possibility to expand the range

of parameters connected to TGFs. Starting with one BGO detector and real-time data, several detectors will increase the measurement of correlated features, such as radio frequency signals originating from the same discharge.
Future work should continue to compare TGFs measured by satellite-based instruments with ground-based data. This comparison will provide insights into the spectral properties and possible differences in the propagation direction of TGFs. Especially the use of a BGO detector similar to the ones mounted on Fermi will provide important measurements as soon as it is ready to be started. Since the detectors are technically similar, the measured signal does not need to be adjusted for differing detector effects. It can be directly compared to the Fermi signal, and therefore possible differences between ground-based and space-based observations can be detected more easily. The use of this detector will allow good comparison between the different data. It can help to determine how the global atmosphere modifies the TGF signal as it is measured by a similar detetor at the UFS and possibly at Fermi.

Bibliography

Vladislav Mazur. *Principles of Lightning Physics*. 2053-2563. IOP Publishing, 2016. ISBN 978-0-7503-1152-6. doi: 10.1088/978-0-7503-1152-6. URL https://dx.doi.org/10.1088/978-0-7503-1152-6.

Manoj Paras and Rani Pooja. Terrestrial gamma-ray flashes and other high energy atmospheric phenomena: An overview. *Disaster Advances*, 14:107–125, 04 2021.

Joseph R. Dwyer and Martin A. Uman. The physics of lightning. *Physics Reports*, 534(4):147–241, 2014. ISSN 0370-1573. doi: https://doi.org/10.1016/j.physrep.2013.09.004. URL https://www.sciencedirect.com/science/article/pii/S037015731300375X. The Physics of Lightning.

C. Köhn, M. Heumesser, O. Chanrion, K. Nishikawa, V. Reglero, and T. Neubert. The emission of terrestrial gamma ray flashes from encountering streamer coronae associated to the breakdown of lightning leaders. *Geophysical Research Letters*, 47(20):e2020GL089749, 2020. doi: https://doi.org/10.1029/2020GL089749. URL https://agupubs.onlinelibrary.wiley.com/doi/abs/10.1029/2020GL089749. e2020GL089749 10.1029/2020GL089749.

Joseph Dwyer, David Smith, and Steven Cummer. High-energy atmospheric physics: Terrestrial gamma-ray flashes and related phenomena. *Space Science Reviews*, 173, 11 2012. doi: 10.1007/s11214-012-9894-0.

Martino Marisaldi, Fabio Fuschino, Claudio Labanti, Marco Tavani, Andrea Argan, Ettore Del Monte, Francesco Longo, Guido Barbiellini, Andrea Giuliani, Alessio Trois, Andrea Bulgarelli, Fulvio Gianotti, and Massimo Trifoglio. Terrestrial gamma-ray flashes. *Nuclear Instruments and Methods in Physics Research Section A: Accelerators, Spectrometers, Detectors and Associated Equipment*, 720:83–87, 2013.

ISSN 0168-9002. doi: https://doi.org/10.1016/j.nima.2012.12.029. URL https://www.sciencedirect.com/science/article/pii/S0168900212015628. Selected papers from the 2nd International Conference Frontiers in Diagnostic Technologies (ICFDT2).

Yuuki Wada, Takeshi Morimoto, Ting Wu, Daohong Wang, Hiroshi Kikuchi, Yoshitaka Nakamura, Eiichi Yoshikawa, Tomoo Ushio, and Harufumi Tsuchiya. Downward terrestrial gamma-ray flash associated with collision of lightning leaders. *Science Advances*, 11(21):eads6906, 2025. doi: 10.1126/sciadv.ads6906. URL https://www.science.org/doi/abs/10.1126/sciadv.ads6906.

Zhang Hongbo, Lu Gaopeng, Lyu Fanchao, Li Xiao, Qie Xiushu, and Liu Ruiting. Measurements and analysis of terrestrial gamma-ray flashes (tgfs) within china. In *2019 11th Asia-Pacific International Conference on Lightning (APL)*, pages 1–4, 2019a. doi: 10.1109/APL.2019.8816055.

Britannica, Aug 2025. URL https://www.britannica.com/science/thunderstorm. Accessed: 2025-09-04.

Skybrary. Lifecycle of the thunderstorm, 2025. URL https://skybrary.aero/articles/lifecycle-thunderstorm. Accessed: 2025-07-14.

Horace R. Byers and Roscoe R. Braham. Thunderstorm structure and circulation. *Journal of Atmospheric Sciences*, 5(3):71 – 86, 1948. doi: 10.1175/1520-0469(1948)005<0071:TSAC>2.0.CO;2. URL https://journals.ametsoc.org/view/journals/atsc/5/3/1520-0469_1948_005_0071_tsac_2_0_co_2.xml.

V. V. Surkov and M. Hayakawa. Underlying mechanisms of transient luminous events: a review. *Annales Geophysicae*, 30(8):1185–1212, 2012a. doi: 10.5194/angeo-30-1185-2012. URL https://angeo.copernicus.org/articles/30/1185/2012/.

Danyal Petersen, Matthew Bailey, William H. Beasley, and John Hallett. A brief review of the problem of lightning initiation and a hypothesis of initial lightning leader formation. *Journal of Geophysical Research (Atmospheres)*, 113(D17):D17205, September 2008. doi: 10.1029/2007JD009036.

V. V. Surkov and M. Hayakawa. Underlying mechanisms of transient luminous events: a review. *Annales Geophysicae*, 30(8):1185–1212, 2012b. doi: 10.5194/angeo-30-1185-2012. URL `https://angeo.copernicus.org/articles/30/1185/2012/`.

Carolynne Montijn and Ute Ebert. Diffusion correction to the raether–meek criterion for the avalanche-to-streamer transition. *Journal of Physics D: Applied Physics*, 39: 2979, 06 2006. doi: 10.1088/0022-3727/39/14/017.

Samir Bedoui. *Overvoltages Evaluation in Transformation Substations under Lightning effect*. PhD thesis, Larbi Ben M'Hidi University, Oum El Bouaghi, 07 2019.

Seho Kim, Taehyung Nam, and Dongwon Jung. Experimental validation of an onboard transient luminous events observation system for visioncube via ground simulation environment. *Aerospace*, 5:100, 09 2018. doi: 10.3390/aerospace5040100.

Carolyn Kierans, Tadayuki Takahashi, and Gottfried Kanbach. Compton telescopes for gamma-ray astrophysics. In C. Bambi, S. Katsanevas, and N. Omodei, editors, *Handbook of X-ray and Gamma-ray Astrophysics*. Springer, 2022. URL `https://arxiv.org/abs/2208.07819`. arXiv:2208.07819.

PJ Karpius and TD Reilly. Gamma-ray interactions with matter. In *Nondestructive Assay of Nuclear Materials for Safeguards and Security*, pages 27–41. Springer, 2024.

Ali Farzanehpoor Alwars and Faezeh Rahmani. A feasibility study of gamma ray source finder development for multiple sources scenario based on a monte carlo simulation. *Scientific Reports*, 11:6121, 03 2021. doi: 10.1038/s41598-021-85706-4.

William R Leo. *Techniques for nuclear and particle physics experiments: a how-to approach*. Springer Science & Business Media, 1994.

Malcolm S. Longair. *High Energy Astrophysics - Third Edition*. Cambridge University Press, 2014. ISBN 9780521756181.

Syed Naeem Ahmed. 2 - interaction of radiation with matter. In Syed Naeem Ahmed, editor, *Physics and Engineering of Radiation Detection (Second Edition)*, pages 65–

155. Elsevier, second edition edition, 2015. ISBN 978-0-12-801363-2. doi: https://doi.org/10.1016/B978-0-12-801363-2.00002-4. URL https://www.sciencedirect.com/science/article/pii/B9780128013632000024.

G Nelson and Doug Reilly. Gamma-ray interactions with matter. *Passive nondestructive analysis of nuclear materials*, 2:27–42, 1991.

R Thalman, K Zarzana, Tolbert M A, and Volkamer R. Rayleigh scattering cross-section measurements of nitrogen, argon, oxygen and air. *Journal of Quantitative Spectroscopy & Radiative Transfer*, 147:171–177, 2014.

Mass attenuation coefficient. Mass attenuation coefficient determination for our atmosphere, 2025. URL https://physics.nist.gov/PhysRefData/Xcom/html/xcom1.html. Accessed: 2025-03-13.

Rasha Abbasi, John Belz, Ryan Le Von, Dan Rodeheffer, Paul Krehbiel, Jackson Remington, and William Rison. Ground-based observations of terrestrial gamma ray flashes associated with downward-directed lightning leaders. *EPJ Web Conf.*, 197: 03002, 2019. doi: 10.1051/epjconf/201919703002. URL https://doi.org/10.1051/epjconf/201919703002.

K.P. Lieb. Lebensdauermessungen in 14n, 15n und 22ne. *Nuclear Physics*, 85(2):461–475, 1966. ISSN 0029-5582. doi: https://doi.org/10.1016/0029-5582(66)90636-5. URL https://www.sciencedirect.com/science/article/pii/0029558266906365.

Yuuki Wada, Teruaki Enoto, Yoshitaka Nakamura, Yoshihiro Furuta, Takayuki Yuasa, Kazuhiro Nakazawa, Takeshi Morimoto, Mitsuteru Sato, Takahiro Matsumoto, Daisuke Yonetoku, Tatsuya Sawano, Hideo Sakai, Masashi Kamogawa, Tomoo Ushio, Kazuo Makishima, and Harufumi Tsuchiya. Gamma-ray glow preceding downward terrestrial gamma-ray flash. *Communications Physics*, 2(1):67, December 2019a. doi: 10.1038/s42005-019-0168-y.

Teruaki Enoto, Yuuki Wada, Yoshihiro Furuta, Kazuhiro Nakazawa, Takayuki Yuasa, Kazufumi Okuda, Kazuo Makishima, Mitsuteru Sato, Yousuke Sato, Toshio Nakano, Daigo Umemoto, and Harufumi Tsuchiya. Photonuclear reactions triggered by light-

ning discharge. *Nature*, 551:481–484, 2017. URL https://api.semanticscholar.org/CorpusID:4388159.

Zhang Hongbo, Lu Gaopeng, Lyu Fanchao, Li Xiao, Qie Xiushu, and Liu Ruiting. Measurements and analysis of terrestrial gamma-ray flashes (tgfs) within china. In *2019 11th Asia-Pacific International Conference on Lightning (APL)*, pages 1–4, 2019b. doi: 10.1109/APL.2019.8816055.

Y. Wada, T. Enoto, K. Nakazawa, Y. Furuta, T. Yuasa, Y. Nakamura, T. Morimoto, T. Matsumoto, K. Makishima, and H. Tsuchiya. Downward terrestrial gamma-ray flash observed in a winter thunderstorm. *Phys. Rev. Lett.*, 123:061103, Aug 2019b. doi: 10.1103/PhysRevLett.123.061103. URL https://link.aps.org/doi/10.1103/PhysRevLett.123.061103.

G. J. Fishman, P. N. Bhat, R. Mallozzi, J. M. Horack, T. Koshut, C. Kouveliotou, G. N. Pendleton, C. A. Meegan, R. B. Wilson, W. S. Paciesas, S. J. Goodman, and H. J. Christian. Discovery of intense gamma-ray flashes of atmospheric origin. *Science*, 264(5163):1313–1316, 1994. doi: 10.1126/science.264.5163.1313. URL https://www.science.org/doi/abs/10.1126/science.264.5163.1313.

J. R. Dwyer, H. K. Rassoul, M. Al-Dayeh, L. Caraway, A. Chrest, B. Wright, E. Kozak, J. Jerauld, M. A. Uman, V. A. Rakov, D. M. Jordan, and K. J. Rambo. X-ray bursts associated with leader steps in cloud-to-ground lightning. *Geophysical Research Letters*, 32(1):2004GL021782, January 2005. ISSN 0094-8276, 1944-8007. doi: 10.1029/2004GL021782. URL https://agupubs.onlinelibrary.wiley.com/doi/10.1029/2004GL021782.

C. A. Skeie, N. Østgaard, A. Mezentsev, I. Bjørge-Engeland, M. Marisaldi, N. Lehtinen, V. Reglero, and T. Neubert. The temporal relationship between terrestrial gamma-ray flashes and associated optical pulses from lightning. *Journal of Geophysical Research: Atmospheres*, 127(17):e2022JD037128, 2022. doi: https://doi.org/10.1029/2022JD037128. URL https://agupubs.onlinelibrary.wiley.com/doi/abs/10.1029/2022JD037128. e2022JD037128 2022JD037128.

Ningyu Liu and Joseph R. Dwyer. Modeling terrestrial gamma ray flashes produced

by relativistic feedback discharges. *Journal of Geophysical Research (Space Physics)*, 118(5):2359–2376, May 2013. doi: 10.1002/jgra.50232.

Joseph R. Dwyer, Ningyu Liu, J. Eric Grove, Hamid Rassoul, and David M. Smith. Characterizing the source properties of terrestrial gamma ray flashes. *Journal of Geophysical Research: Space Physics*, 122(8):8915–8932, 2017. doi: https://doi.org/10.1002/2017JA024141. URL `https://agupubs.onlinelibrary.wiley.com/doi/abs/10.1002/2017JA024141`.

Fanchao Lyu, Steven Cummer, and Lindsay McTague. Insights into high peak current in-cloud lightning events during thunderstorms. *Geophysical Research Letters*, 42: 1–8, 08 2015. doi: 10.1002/2015GL065047.

Nikolai Ostgaard, Thomas Gjesteland, Johan Stadsnes, Paul Connell, and Brant Carlson. Production altitude and time delays of the terrestrial gamma flashes: Revisiting the burst and transient source experiment spectra. *Journal of Geophysical Research*, 113:2307, 02 2008. doi: 10.1029/2007JA012618.

A. Lindanger, C. A. Skeie, M. Marisaldi, I. Bjørge-Engeland, N. Østgaard, A. Mezentsev, D. Sarria, N. Lehtinen, V. Reglero, O. Chanrion, and T. Neubert. Production of terrestrial gamma-ray flashes during the early stages of lightning flashes. *Journal of Geophysical Research: Atmospheres*, 127(8):e2021JD036305, 2022. doi: https://doi.org/10.1029/2021JD036305. URL `https://agupubs.onlinelibrary.wiley.com/doi/abs/10.1029/2021JD036305`. e2021JD036305 2021JD036305.

Elizabeth Gibney. Mystery gamma rays could help solve age-old lightning puzzle, Feb 2021. URL `https://www.nature.com/articles/d41586-021-00395-3`. Accessed: 2025-09-04.

A. V. Gurevich, G. M. Milikh, and R. Roussel-Dupre. Runaway electron mechanism of air breakdown and preconditioning during a thunderstorm. *Physics Letters A*, 165 (5-6):463–468, June 1992. doi: 10.1016/0375-9601(92)90348-P.

J. R. Dwyer. A fundamental limit on electric fields in air. *Geophysical Research Letters*, 30(20):2055, October 2003. doi: 10.1029/2003GL017781.

J. R. Dwyer. Source mechanisms of terrestrial gamma-ray flashes. *Journal of Geophysical Research (Atmospheres)*, 113(D10):D10103, May 2008. doi: 10.1029/2007JD009248.

Alexander Broberg Skeltved, Nikolai Østgaard, Brant Carlson, Thomas Gjesteland, and Sebastien Celestin. Modeling the relativistic runaway electron avalanche and the feedback mechanism with geant4. *Journal of Geophysical Research: Space Physics*, 119(11):9174–9191, November 2014. ISSN 2169-9402. doi: 10.1002/2014ja020504. URL `http://dx.doi.org/10.1002/2014JA020504`.

C. T. R. Wilson. The acceleration of β-particles in strong electric fields such as those of thunderclouds. *Mathematical Proceedings of the Cambridge Philosophical Society*, 22(4):534–538, 1925. doi: 10.1017/S0305004100003236.

Nicole A. Kelley, David M. Smith, Joseph R. Dwyer, Michael Splitt, Steven Lazarus, Forest Martinez-McKinney, Bryna Hazelton, Brian Grefenstette, Alexander Lowell, and Hamid K. Rassoul. Relativistic electron avalanches as a thunderstorm discharge competing with lightning. *Nature Communications*, 6:7845, August 2015. doi: 10.1038/ncomms8845.

Andrew B. Collier, Thomas Gjesteland, and Nikolai ØStgaard. Assessing the power law distribution of tgfs. *Journal of Geophysical Research (Space Physics)*, 116(A10):A10320, October 2011. doi: 10.1029/2011JA016612.

Jeffrey M. Chaffin, David M. Smith, Jeff Lapierre, Steve Cummer, John Ortberg, Antonio Sunjerga, Amirhossein Mostajabi, Marcos Rubinstein, and Farhad Rachidi. Mountaintop gamma ray observations of three terrestrial gamma-ray flashes at the säntis tower, switzerland with coincident radio waveforms. *Journal of Geophysical Research (Atmospheres)*, 129(2):e2023JD039761, January 2024. doi: 10.1029/2023JD039761.

J. R. Dwyer and D. M. Smith. A comparison between monte carlo simulations of runaway breakdown and terrestrial gamma-ray flash observations. *Geophysical Research Letters*, 32(22):L22804, November 2005. doi: 10.1029/2005GL023848.

T. Gjesteland, N. Østgaard, A. B. Collier, B. E. Carlson, M. B. Cohen, and N. G.

Lehtinen. Confining the angular distribution of terrestrial gamma ray flash emission. *Journal of Geophysical Research: Space Physics*, 116(A11), 2011. doi: https://doi.org/10.1029/2011JA016716. URL `https://agupubs.onlinelibrary.wiley.com/doi/abs/10.1029/2011JA016716`.

B. E. Carlson, T. Gjesteland, and N. Østgaard. Connecting the terrestrial gamma-ray flash source strength and observed fluence distributions. *Journal of Geophysical Research (Space Physics)*, 117(A1):A01314, January 2012. doi: 10.1029/2011JA017122.

Alessandro Ursi. A study of tgf detectability at 2165 m altitude: Simulations for the mountain-based gamma-flash program. In *AGU Fall Meeting Abstracts*, volume 2021 of *AGU Fall Meeting Abstracts*, pages AE15A–1883, December 2021.

M. Marisaldi, M. Galli, C. Labanti, N. Østgaard, D. Sarria, S. A. Cummer, F. Lyu, A. Lindanger, R. Campana, A. Ursi, M. Tavani, F. Fuschino, A. Argan, A. Trois, C. Pittori, and F. Verrecchia. On the high-energy spectral component and fine time structure of terrestrial gamma ray flashes. *Journal of Geophysical Research: Atmospheres*, 124(14):7484–7497, July 2019. ISSN 2169-8996. doi: 10.1029/2019jd030554. URL `http://dx.doi.org/10.1029/2019JD030554`.

S. Foley, G. Fitzpatrick, M. S. Briggs, V. Connaughton, D. Tierney, S. McBreen, J. R. Dwyer, V. L. Chaplin, P. N. Bhat, D. Byrne, E. Cramer, G. J. Fishman, S. Xiong, J. Greiner, R. M. Kippen, C. A. Meegan, W. S. Paciesas, R. D. Preece, A. von Kienlin, and C. Wilson-Hodge. Pulse properties of terrestrial gamma-ray flashes detected by the fermi gamma-ray burst monitor. *Journal of Geophysical Research: Space Physics*, 119(7):5931–5942, 2014. doi: https://doi.org/10.1002/2014JA019805. URL `https://agupubs.onlinelibrary.wiley.com/doi/abs/10.1002/2014JA019805`.

Gamma-ray spectra. Gamma-ray energies of radioactive isotopes, 2026. URL `https://www.nndc.bnl.gov/nudat3/?utm_source=chatgpt.com`. Accessed: 2025-11-26.

Davide Romano, Giuseppe Sabatino, Marcella Di Bella, Francesco Italiano, Maria Teresa Caccamo, Alessandro Tripodo, and Salvatore magazù. Natural radioactivity and radiological hazard for humans: A simple introduction for newbies and students. new perspectives and innovative teaching methods. *Atti della Accademia Peloritana dei Pericolanti*, 99, 08 2021. doi: 10.1478/AAPP.99S1A39.

K. Kovler, H. Friedmann, B. Michalik, W. Schroeyers, A. Tsapalov, S. Antropov, T. Bituh, and D. Nicolaides. 3 - basic aspects of natural radioactivity. In Wouter Schroeyers, editor, *Naturally Occurring Radioactive Materials in Construction*, pages 13–36. Woodhead Publishing, 2017. ISBN 978-0-08-102009-8. doi: https://doi.org/10.1016/B978-0-08-102009-8.00003-7. URL `https://www.sciencedirect.com/science/article/pii/B9780081020098000037`.

A.R. Bell. Cosmic ray acceleration. *Astroparticle Physics*, 43:56–70, 2013. ISSN 0927-6505. doi: https://doi.org/10.1016/j.astropartphys.2012.05.022. URL `https://www.sciencedirect.com/science/article/pii/S0927650512001272`. Seeing the High-Energy Universe with the Cherenkov Telescope Array - The Science Explored with the CTA.

K. O'Brien, W. Friedberg, Herbert H. Sauer, and D.F. Smart. Atmospheric cosmic rays and solar energetic particles at aircraft altitudes. *Environment International*, 22:9–44, 1996. ISSN 0160-4120. doi: https://doi.org/10.1016/S0160-4120(96)00086-4. URL `https://www.sciencedirect.com/science/article/pii/S0160412096000864`. The Natural Radiation Environment VI.

Jozef Masarik. Chapter 1 origin and distribution of radionuclides in the continental environment. In Klaus Froehlich, editor, *Environmental Radionuclides: Tracers and Timers of Terrestrial Processes*, volume 16 of *Radioactivity in the Environment*, pages 1–25. Elsevier, 2009. doi: https://doi.org/10.1016/S1569-4860(09)01601-5. URL `https://www.sciencedirect.com/science/article/pii/S1569486009016015`.

Shaowen Hu. Solar particle events and radiation exposure in space. *The Health Risks of Extraterrestrial Environments (THREE)*, 03 2017.

Don Porcelli and Mark Baskaran. Handbook of environmental isotope geochemistry. 05 2020.

G. Fiorentini, Marcello Lissia, and Fabio Mantovani. Geo-neutrinos and earth's interior. *Phys. Rep.*, 453, 08 2007. doi: 10.1016/j.physrep.2007.09.001.

Umweltforschungsstation Schneefernerhaus. Forschung – umweltforschungsstation

schneefernerhaus, 2025. URL https://schneefernerhaus.de/forschung/. Accessed: 2025-06-30.

Nilgün Demir and Zehra Nur Kuluöztürk. Determination of energy resolution for a nai(tl) detector modeled with fluka code. *Nuclear Engineering and Technology*, 53(11):3759–3763, 2021. ISSN 1738-5733. doi: https://doi.org/10.1016/j.net.2021.05.017. URL https://www.sciencedirect.com/science/article/pii/S1738573321002680.

Andreas Zoglauer. An introduction to megalib the medium-energy gamma-ray astronomy library, 2006a. https://megalibtoolkit.com/documents/MEGAlib_TheOverview.pdf.

Andreas Zoglauer. Megalib - the medium-energy gamma-ray astronomy library, 2006b. https://megalibtoolkit.com/overview.html.

Andreas Zoglauer, Georg Weidenspointner, Michelle Galloway, Steven E. Boggs, and Cornelia B. Wunderer. Cosima — the cosmic simulator of megalib. In *2009 IEEE Nuclear Science Symposium Conference Record (NSS/MIC)*, pages 2053–2059, 2009. doi: 10.1109/NSSMIC.2009.5402128.

J. Allison, K. Amako, J. Apostolakis, H. Araujo, P. Arce Dubois, M. Asai, G. Barrand, R. Capra, S. Chauvie, R. Chytracek, G.A.P. Cirrone, G. Cooperman, G. Cosmo, G. Cuttone, G.G. Daquino, M. Donszelmann, M. Dressel, G. Folger, F. Foppiano, J. Generowicz, V. Grichine, S. Guatelli, P. Gumplinger, A. Heikkinen, I. Hrivnacova, A. Howard, S. Incerti, V. Ivanchenko, T. Johnson, F. Jones, T. Koi, R. Kokoulin, M. Kossov, H. Kurashige, V. Lara, S. Larsson, F. Lei, O. Link, F. Longo, M. Maire, A. Mantero, B. Mascialino, I. McLaren, P. Mendez Lorenzo, K. Minamimoto, K. Murakami, P. Nieminen, L. Pandola, S. Parlati, L. Peralta, J. Perl, A. Pfeiffer, M.G. Pia, A. Ribon, P. Rodrigues, G. Russo, S. Sadilov, G. Santin, T. Sasaki, D. Smith, N. Starkov, S. Tanaka, E. Tcherniaev, B. Tome, A. Trindade, P. Truscott, L. Urban, M. Verderi, A. Walkden, J.P. Wellisch, D.C. Williams, D. Wright, and H. Yoshida. Geant4 developments and applications. *IEEE Transactions on Nuclear Science*, 53 (1):270–278, 2006. doi: 10.1109/TNS.2006.869826.

S. Agostinelli, J. Allison, K. Amako, J. Apostolakis, H. Araujo, P. Arce, M. Asai,

D. Axen, S. Banerjee, G. Barrand, F. Behner, L. Bellagamba, J. Boudreau, L. Broglia, A. Brunengo, H. Burkhardt, S. Chauvie, J. Chuma, R. Chytracek, G. Cooperman, G. Cosmo, P. Degtyarenko, A. Dell'Acqua, G. Depaola, D. Dietrich, R. Enami, A. Feliciello, C. Ferguson, H. Fesefeldt, G. Folger, F. Foppiano, A. Forti, S. Garelli, S. Giani, R. Giannitrapani, D. Gibin, J.J. Gómez Cadenas, I. González, G. Gracia Abril, G. Greeniaus, W. Greiner, V. Grichine, A. Grossheim, S. Guatelli, P. Gumplinger, R. Hamatsu, K. Hashimoto, H. Hasui, A. Heikkinen, A. Howard, V. Ivanchenko, A. Johnson, F.W. Jones, J. Kallenbach, N. Kanaya, M. Kawabata, Y. Kawabata, M. Kawaguti, S. Kelner, P. Kent, A. Kimura, T. Kodama, R. Kokoulin, M. Kossov, H. Kurashige, E. Lamanna, T. Lampén, V. Lara, V. Lefebure, F. Lei, M. Liendl, W. Lockman, F. Longo, S. Magni, M. Maire, E. Medernach, K. Minamimoto, P. Mora de Freitas, Y. Morita, K. Murakami, M. Nagamatu, R. Nartallo, P. Nieminen, T. Nishimura, K. Ohtsubo, M. Okamura, S. O'Neale, Y. Oohata, K. Paech, J. Perl, A. Pfeiffer, M.G. Pia, F. Ranjard, A. Rybin, S. Sadilov, E. Di Salvo, G. Santin, T. Sasaki, N. Savvas, Y. Sawada, S. Scherer, S. Sei, V. Sirotenko, D. Smith, N. Starkov, H. Stoecker, J. Sulkimo, M. Takahata, S. Tanaka, E. Tcherniaev, E. Safai Tehrani, M. Tropeano, P. Truscott, H. Uno, L. Urban, P. Urban, M. Verderi, A. Walkden, W. Wander, H. Weber, J.P. Wellisch, T. Wenaus, D.C. Williams, D. Wright, T. Yamada, H. Yoshida, and D. Zschiesche. Geant4—a simulation toolkit. *Nuclear Instruments and Methods in Physics Research Section A: Accelerators, Spectrometers, Detectors and Associated Equipment*, 506(3):250–303, 2003. ISSN 0168-9002. doi: https://doi.org/10.1016/S0168-9002(03)01368-8. URL `https://www.sciencedirect.com/science/article/pii/S0168900203013688`.

Makoto Asai. Introduction to geant4, 2006. `https://cds.cern.ch/record/491492/files/p107.pdf`.

UFS Elevation. Ufs elevation dataset, 2025. URL `https://earthexplorer.usgs.gov/`. Accessed: 2025-03-27.

WWLLN. Wwlln global lightning climatological datasets and animations, 2025. URL `https://wwlln.net/climate/`. Accessed: 2025-12-02.

Elizabeth A. DiGangi, Michael Stock, and Jeff Lapierre. Thunder hours: How old methods offer new insights into thunderstorm climatology. *Bulletin of the American Meteorological Society*, 103(2):E548 – E569, 2022. doi: 10.1175/BAMS-D-20-0198.1.

Brian D. Milbrath, Anthony J. Peurrung, Mary Bliss, William J. Weber, and WA (United States) Pacific Northwest National Lab., Richland. Radiation detector materials: An overview. *Journal of Materials Research*, 23(10):p. 2561–2581, Okt 2008. ISSN 0884-2914. doi: 10.1557/JMR.2008.0319.

D. M. Smith, B. J. Hazelton, B. W. Grefenstette, J. R. Dwyer, R. H. Holzworth, and E. H. Lay. Terrestrial gamma ray flashes correlated to storm phase and tropopause height. *Journal of Geophysical Research (Space Physics)*, 115(20):A00E49, August 2010. doi: 10.1029/2009JA014853.

Fermi GBM. Fermi gbm datasets, 2025. URL `https://fermi.gsfc.nasa.gov/ssc/data/access/gbm/tgf/`. Accessed: 2026-01-15.

Charles Meegan, Giselher Lichti, P. N. Bhat, Elisabetta Bissaldi, Michael S. Briggs, Valerie Connaughton, Roland Diehl, Gerald Fishman, Jochen Greiner, Andrew S. Hoover, Alexander J. van der Horst, Andreas von Kienlin, R. Marc Kippen, Chryssa Kouveliotou, Sheila McBreen, W. S. Paciesas, Robert Preece, Helmut Steinle, Mark S. Wallace, Robert B. Wilson, and Colleen Wilson-Hodge. The fermigamma-ray burst monitor. *The Astrophysical Journal*, 702(1):791–804, August 2009. ISSN 1538-4357. doi: 10.1088/0004-637x/702/1/791. URL `http://dx.doi.org/10.1088/0004-637X/702/1/791`.

David J. Thompson and Colleen A. Wilson-Hodge. *Fermi Gamma-Ray Space Telescope*, page 1–31. Springer Nature Singapore, November 2022. ISBN 9789811645440. doi: 10.1007/978-981-16-4544-0_58-1. URL `http://dx.doi.org/10.1007/978-981-16-4544-0_58-1`.

O. J. Roberts, G. Fitzpatrick, M. Stanbro, S. McBreen, M. S. Briggs, R. H. Holzworth, J. E. Grove, A. Chekhtman, E. S. Cramer, and B. G. Mailyan. The first fermi-gbm terrestrial gamma ray flash catalog. *Journal of Geophysical Research: Space Physics*, 123(5):4381–4401, 2018. doi: https://doi.org/10.1029/2017JA024837. URL `https://agupubs.onlinelibrary.wiley.com/doi/abs/10.1029/2017JA024837`.

Fermi GBM DRM. Detector response matrix of fermi gbm, 2026. URL `https://fermi.gsfc.nasa.gov/ssc/data/analysis/gbm/gbm_data_tools/gdt-docs/notebooks/Responses.html`. Accessed: 2026-02-11.

M. Yassine, F. Piron, F. Daigne, R. Mochkovitch, F. Longo, N. Omodei, and G. Vianello. A new fitting function for grb mev spectra based on the internal shock synchrotron model. *Astronomy & Astrophysics*, 640:A91, August 2020. ISSN 1432-0746. doi: 10.1051/0004-6361/201937057. URL http://dx.doi.org/10.1051/0004-6361/201937057.

Daniel Foreman-Mackey, Will Farr, Manodeep Sinha, Anne Archibald, David Hogg, Jeremy Sanders, Joe Zuntz, Peter Williams, Andrew Nelson, Miguel de Val-Borro, Tobias Erhardt, Ilya Pashchenko, and Oriol Pla. emcee v3: A python ensemble sampling toolkit for affine-invariant mcmc. *Journal of Open Source Software*, 4(43): 1864, November 2019. ISSN 2475-9066. doi: 10.21105/joss.01864. URL http://dx.doi.org/10.21105/joss.01864.

Burst analysis. Analyzing bursts with 3ml, 2025. URL https://threeml.readthedocs.io/en/stable/notebooks/grb080916C.html. Accessed: 2025-07-28.

Eigenständigkeitserklärung

Hiermit erkläre ich an Eides statt, dass ich die Masterarbeit

"Modeling the Response to Terrestrial Gamma-Ray Flashes at the Zugspitze Research Station"

selbstständig angefertigt und keine anderen als die von mir angegebenen Quellen und Hilfsmittel benutzt habe.
Ich erkläre außerdem, dass diese Arbeit weder in gleicher oder anderer Form bereits in einem anderen Prüfungsverfahren vorgelegen hat.
Ich habe früher außer den mit dem Zulassungsgesuch urkundlich vorgelegten Graden keine weiteren akademischen Grade erworben oder zu erwerben versucht.

Würzburg, den 13/02/2026

Patrik Ehrmann